FUNDAMENTALS OF MOLECULAR COMMUNICATION OVER MICROFLUIDIC CHANNELS

A Dissertation
Presented to
The Academic Faculty

by

Ahmet Ozan Bicen

In Partial Fulfillment
of the Requirements for the Degree
Doctor of Philosophy in the
School of Electrical and Computer Engineering

Georgia Institute of Technology
May 2016

FUNDAMENTALS OF MOLECULAR COMMUNICATION OVER MICROFLUIDIC CHANNELS

Approved by:

Professor Ian F. Akyildiz, Advisor
School of Electrical and Computer Engineering
Georgia Institute of Technology

Professor Mary Ann Weitnaeuer
School of Electrical and Computer Engineering
Georgia Institute of Technology

Professor Geoffrey Y. Li
School of Electrical and Computer Engineering
Georgia Institute of Technology

Professor Raghupathy Sivakumar
School of Electrical and Computer Engineering
Georgia Institute of Technology

Associate Professor Craig R. Forest
School of Mechanical Engineering
Georgia Institute of Technology

Date Approved: 15 March 2016

Anneme ve Babama,

Ayşe ve Halil Biçen

ACKNOWLEDGEMENTS

I have been honored to have had the opportunity to work with Prof. Ian F. Akyildiz during my Ph.D. study. He has shared his immense knowledge and experience without any reserve. He has been an enthusiastic advisor with a genuine concern for my well-being. I would like to also express my deepest gratitude to Prof. Ian F. Akyildiz for his encouragement and valuable support towards the successful completion of this thesis.

I thank Prof. Geoffrey Y. Li, Prof. Mary Ann Weitnauer, Prof. Raghupathy Sivakumar, and Prof. Craig R. Forest for serving on my dissertation committee.

This thesis would not have been possible had my M.Sc. advisor Prof. Ozgur B. Akan not recommended me to Prof. Akyildiz for a Ph.D. student position four years ago, which led me to attend Georgia Tech as a graduate student. I would like to take this chance to thank Prof. Ozgur B. Akan.

I thank all former and current members of the Broadband and Wireless Networking Laboratory for sharing this learning environment and experience. Without their help, my stay here would not have been such pleasant and comfortable. I am especially thankful to Bige D. Unluturk, Chong Han, Abdallah Al-Shehri, Ahyoung Lee, Youssef Chahibi, Shih-Chun Lin, and Janne Lehtomaki for their friendship and support. A special thank goes to Massimiliano Pierobon, Josep M. Jornet, and Ravikumar Balakrishnan for their mentorship during my first year of Ph.D. study. Josep M. Jornet has been the first person to look for, whenever I needed an advice on almost anything. I enjoyed a large number of discussions with them, sometimes on research, sometimes on personal issues, which enriched me in many ways. I am deeply indebted to them for their critical help in a number of issues related to my stay in Atlanta.

I also want to extend my thanks to all my friends who made the past four years very enjoyable. I would like to express my deepest gratitude to Cem Caliskan, Can Temel, Rafael Castillo, John Krier, Cantay Caliskan, Ozgur Ergul, Burak Kocuk, and Can Onur.

Last but not least, I would like to thank my family. I would like to thank my parents for their constant support and encouragement during my stay in Atlanta. I would like to thank my brothers for spending hours to entertain and encourage me during difficult times. Half the world away, my parents have been my biggest strength. During all these years far from home, they have still managed to convey their love and affection. My achievements so far have been just a testament to their sacrifices, determination and dedication.

TABLE OF CONTENTS

LIST OF TABLES

LIST OF FIGURES

SUMMARY

The interconnection of molecular machines with different functionalities to form molecular communication systems can increase the number of design possibilities and overcome the limited reliability of the individual molecular machines. Artificial information exchange using molecular signals would also expand the capabilities of single engineered cell populations by providing them a way to cooperate across heterogeneous cell populations for the applications of synthetic biology and lab-on-a-chip systems. The realization of molecular communication systems necessitates analysis and design of the communication channel, where the information carrying molecular signal is transported from the transmitter to the receiver.

In this thesis, significant progress towards the use of microfluidic channels to interconnect molecular transmitter and receiver pairs is presented. System-theoretic analysis of the microfluidic channels are performed, and a finite-impulse response filter is designed using microfluidic channels. The spectral density of the propagation noise is studied and the additive white Gaussian noise channel model is developed. Memory due to inter-diffusion of the transmitted molecular signals is also modeled. Furthermore, the interference modeling is performed for multiple transmitters and its impact on the communication capacity is shown. Finally, the efficient sampling of the signal transduction by engineered bacterial receivers connected to a microfluidic channel is investigated for the detection of the pulse-amplitude modulated molecular signals. This work lays the foundation for molecular communication over microfluidic channels that will enable interconnection of engineered molecular machines.

CHAPTER I

INTRODUCTION

Molecular communication (MC) is one of the fundamental approaches towards enabling biocompatible communication systems. It can provide advantages for biochemical signal sensing including higher accuracy, high-throughput analysis, compactness, point-of-care diagnostics, and extraction of localized features at nano-scale in biological environments and lab-on-a-chip systems. In the literature, there exist different molecular communication options [5, 6, 37]. For example, the use of different types of molecules is suggested for information encoding. Intercellular Ca^{2+} waves are suggested as an alternative mechanism for molecular signal propagation. The diffusion-based signal propagation has been a focus of interest for MC research so far, in which molecules are transported solely by diffusion through the fluidic medium [7]. The concentration of molecules are used as information carrying signal for molecular communication. The concentration signal is transmitted, i.e., released, into the fluidic channel and is propagated, i.e., transported, to the receiver. According to the received concentration signal, the receiver performs the desired chemical reaction, such as synthesis of molecules.

Molecular communication is not just a miniaturization of the classical communication systems. On the contrary, it requires the development of innovative solutions and the revision of the well-established concepts in the communication theory. Specifically, to elicit highly sophisticated behavior of engineered cells, a physical platform is needed to host molecular transmitter and receiver.

The objective of this thesis has been to establish the foundations of molecular communication over microfluidic channels. A micro channel with fluid flow (microfluidic channel) can serve as a communication channel that connects patches of molecular transmitter and receiver, such as engineered cells. Molecular communication can also expand the capabilities of engineered cell populations by providing them a way to cooperate and coordinate

tasks across heterogeneous cells. For example, the interconnection of engineered cells with different functionalities to form artificial cell-to-cell molecular communication systems can increase the number of design possibilities and overcome the limited precision of individual engineered cells for the applications of synthetic biology and lab-on-a-chip systems including adaptive control of photosynthesis in biofuel cells and diagnosis of cancer by the network of chemist cells on a chip.

1.1 Microfluidic Molecular Communication System

Spectacular evolution of the microfluidic chip technologies has enabled miniaturization, parallelization, automation, and integration of chemical assays for detection, separation, reaction, and sample manipulation operations. Microfluidic platforms for chemical analysis systems have been planned to enable rapid and cost-efficient processing of the application-specific distinct molecules with low reagent consumption [28, 40, 52, 53, 54]. These advances in the microfluidic chip technologies and their salient features for entirely molecular sensing and computation have further entailed the networking of distinct microfluidic systems, i.e., *lab on a chip* [25, 55, 56]. For this purpose, the emerging field of molecular communication, in which the molecular concentration signals are modulated to carry information, stands as a promising solution to enable information transfer among distinct chemical systems [5, 6]. Consequently, molecular communication networks on chip may emerge as the convergence of the large-scale integration of microfluidic systems and molecular communication over microfluidic channels with the objective of *high throughput*, *multi-step* on chip chemical automation in a microfluidic platform.

A molecular communication architecture on a microfluidic chip is illustrated in Fig. 1. In this architecture, the transmitter and the receiver chambers, where the transmitter and the receiver nodes can be hosted, respectively, are connected over a microfluidic channel with fluid flow. In response to a specific stimulus, e.g., external molecular input, the transmitter node releases a concentration of molecules, i.e., transmits the information carrying molecular signal, which propagates through the transmitter chamber, the microfluidic channel, and the receiver chamber via diffusion, convection, and diffusion again, respectively, until reaching

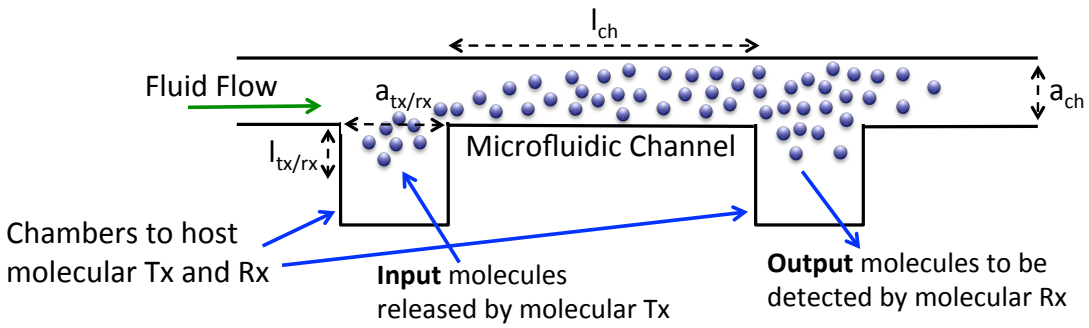

Figure 1: The conceptual illustration of the microfluidic channel with transmitter and receiver channels. l_{ch} is the microfluidic channel distance between the transmitter and the receiver, a_{ch} is the height of the microfluidic channel, $l_{\text{tx/rx}}$ is the distance from the molecular transmitter to the microfluidic channel (the distance from the microfluidic channel to the molecular receiver), and $a_{\text{tx/rx}}$ is the chamber width.

to the receiver node. To realize potential gains and design efficient yet practical molecular communication systems, the understanding of the mass transport mechanisms behind the molecular signal propagation from the transmitter to the receiver is imperative.

1.2 Bacteria-based Molecular Receivers

Molecular communication can facilitate the automation of biochemical assays that would otherwise require the intervention of an external human operator. For example, the distinct patches of chambers can be connected through microfluidic channels to develop bacteria-based chemical analysis systems [27, 57]. Bacteria are extremely capable of detecting biomolecules [58, 59, 60, 61, 62, 63, 64]. Furthermore, bacteria can be genetically engineered to function as a biological molecular oscillator, so that, they can be utilized as the transmitter and the receiver nodes for MC in a microfluidic platform [9, 27, 71, 73]. Therefore, bacteria-based molecular nanonetworks can be utilized in microfluidic platforms to enable integrated assay operations in multiple steps via on-chip information transfer. Using bacteria as the *chemist* inside microfluidic platform, MC between bacteria populations can combine multi-stage reactions on a single microfluidic chip.

The envisioned applications of molecular communication have originated research on

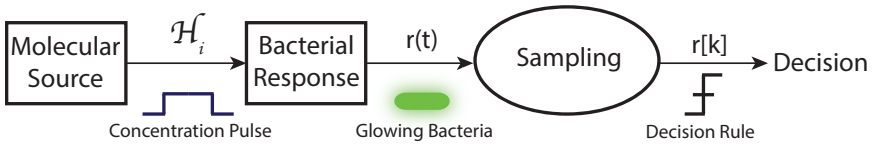

Figure 2: The block diagram representation of the bacteria-based molecular receiver system.

the utilization of the available signaling mechanisms in the cells for information transmission. Molecular communication is ubiquitous in biological systems including populations of microorganisms and organs [6, 9]. For example, bacteria form biofilms and exchange signals to initiate gene expression based on the population density, i.e., quorum sensing. Molecular signals are also present in multicellular organisms, e.g., hormones and neurotransmitters are used to regulate physiological activities. Genetic engineering of cells, specifically bacteria, has been prompted to develop molecular oscillators and transceivers for the information transmission using molecular signals [27, 69, 70, 71]. The study of bacteria and its response to the external environment is critical for understanding cellular response due to the relative ease of engineering and testing, which already gained a wide attention in the literature for sensing and monitoring [60, 62, 64, 72, 73].

The block diagram for the considered bacteria-based molecular receivers is given in Fig. 2. Molecular source releases PAM molecular signals with level $\mathcal{H}_i$. The bacteria transduce the molecular signal to green fluorescent protein (GFP), recorded illumination of which denoted as received signal $r(t)$. The continuous-time received signal $r(t)$ is sampled and the discrete-time $r[k]$ is obtained. Finally, thresholding is applied based on the predefined decision rules. Accordingly, the input molecular signal $\mathcal{H}_i$ is decided.

1.3 Research Objectives

In this thesis, we specifically investigate the communication performance of microfluidic channels to connect molecular transmitter and receiver pairs as well as engineered bacteria populations as a molecular receiver. A considerable portion of this thesis addresses the distortion and noise effects that microfluidic channels cause on the transmitted molecular concentration signal. The developed models of attenuation and noise are used to evaluate

the performance (information rates) of molecular communication over microfluidic channels. In addition, the signal transduction of bacteria is investigated for efficient sampling and detection of molecular signals with biological receivers.

The following four areas are investigated under this research and each of them is described in the following subsections:

1. System-Theoretic Microfluidic Channel Modeling and FIR Filter Design
2. End-to-End Propagation Noise and Memory Analysis for Microfluidic Channels
3. Interference Modeling and Capacity Analysis for Microfluidic Multiple Access Channel
4. Detection of PAM Molecular Signals with Bacterial Receivers on a Microfluidic Channel

1.3.1 System-Theoretic Microfluidic Channel Modeling and FIR Filter Design

Flow-induced Molecular Communication (FMC), where molecular transport is performed via flow, is utilized in microfluidic channels to enhance diffusion-based molecular communication. The incorporation of the microfluidic channel and the transport of molecules by flow, i.e., convection, require a rigorous analysis to develop an end-to-end concentration propagation model and a design for microfluidic channels. Therefore, we perform a system-theoretic analysis of molecular transport first. The system-theoretic model incorporates the solution of flow velocity in microfluidic channels and yields an end-to-end transfer function for concentration propagation based on building blocks of microfluidic channels. Then, the design of microfluidic channels is performed based on the least-squares Finite Impulse Response (FIR) filtering to achieve the desired end-to-end transfer function in FMC. According to the desired pass and stop bands, the required length and aspect-ratio parameters of the microfluidic channels are obtained for FIR filtering. The transfer functions for FMC is elaborated via numerical results. Furthermore, two example designs of microfluidic channels are presented for least-squares FIR band-pass and band-stop filtering in FMC.

1.3.2 End-to-End Propagation Noise and Memory Analysis for Microfluidic Channels

Molecular Communication (MC) between a transmitter and a receiver placed in the chambers attached to a microfluidic channel is investigated. A linear end-to-end channel model is developed capturing the effects of the diffusion and the junction transition at the chambers as well as the microfluidic channel shapes and the fluid flow. The spectral density of the propagation noise is studied and the flat frequency bands are identified for the chambers and the microfluidic channel. This suggests that in certain microfluidic design choices, the spectral density of noise may end up naturally being flat. Motivated by this result, the Additive White Gaussian Noise (AWGN) model is developed based on the chamber, the microfluidic channel, and the fluid flow parameters for the end-to-end propagation noise. Furthermore, the molecular memory is modeled due to inter-diffusion among transmitted molecular signals. The effect of the molecular memory on the end-to-end propagation noise is also analyzed. To substantiate our analytical results, the ranges of physical parameters that yield linear end-to-end MC channel are investigated. These results show validity of the AWGN model for MC over microfluidic channels, and characterize the impact of the microfluidic channel and chamber geometry on the propagation noise and memory.

1.3.3 Interference Modeling and Capacity Analysis for Microfluidic Multiple Access Channel

The impact of the interference on the Molecular Communication (MC) between a transmitter and receiver pair which are connected through a microfluidic channel containing fluid flow is investigated. The interference modeling and the capacity analysis is performed based on the microfluidic channel geometry, the flow velocity, and the distance. During the analysis, time-scale of biological oscillators is specifically targeted, which is in the range of several minutes to a few hours. The Signal-to-Interference and Noise Ratio (SINR) is shown to be constant with respect to the location of the interfering transmitter. The capacity of the MC link between the designated transmitter and the corresponding receiver is shown to be upper bounded by 1 bit/per channel use when exposed to a single interfering transmitter. For the multiple, i.e., N, transmitters, the decay of pairwise MC capacity is also studied as

a factor of N. Finally, placement of the two transmitter and receiver pairs on the opposite sides of the microfluidic channel is studied. Three different microfluidic interference channel configurations, i.e., both-sided interference (microfluidic X channel), one-sided interference (microfluidic Z channel), and interference-free, are proposed based on the distance of the receiver from the interfering transmitter, microfluidic channel cross-section, and the fluid flow velocity.

1.3.4 Detection of PAM Molecular Signals with Bacterial Receivers on a Microfluidic Channel

The sampling of the bacterial signal transduction is investigated for molecular communication (MC). It is assumed that the finite-duration amplitude modulated, i.e., pulse-amplitude modulated (PAM), concentration of a certain type of molecule is used for information transmission. The bacterial signaling pathway is modified to transduce the input molecules to the output signal, i.e., produce green fluorescent protein (GFP). The bacterial signal transduction is composed of a set of biochemical reactions which impose randomness on the response. Therefore, the input-output relation, the timing issues, and the noise effects for the bacteria response are characterized based on both analytical and experimental observations. Sampling schemes for the raw bacteria response are proposed based on the total response duration, the peak value, the ramp-up slope, and the ramp-down slope. Each sampling scheme is shown to be providing a one-to-one and monotonic function of the input. The sampling based on the ramp-up slope is shown to be statistically favorable for the detection of PAM molecular signals. Accordingly, the time interval selection and non-coherent sampling are studied for the efficient calculation of the ramp-up slope from the raw bacteria response. This work provides a basis for the sampling of the raw bacteria response and enables accurate detection of PAM molecular signals via bacterial response for MC and sensing applications.

1.4 Organization of the Thesis

The remainder of this thesis is organized as follows. In Section 2, system-theoretic analysis of the microfluidic channels are performed, and a finite-impulse response filter is designed

using microfluidic channels. In Section 3, noise and memory models are developed for the molecular communication between a transmitter and a receiver placed in the chambers attached to a microfluidic channel. In Section 4, we perform interference modeling and capacity analysis for multiple transmitters connected to a microfluidic channel. In Section 5, the efficient sampling of the signal transduction by the bacterial receivers placed in the chambers attached to a microfluidic channel is investigated. Finally, the Section 6 summarizes the research results and suggests a number of problems for future investigation.

CHAPTER II

SYSTEM-THEORETIC MICROFLUIDIC CHANNEL MODELING AND FIR FILTER DESIGN

In this chapter, a system-theoretic analysis of molecular transport is presented. Additionally, the design of microfluidic channels is performed based on the least-squares Finite Impulse Response (FIR) filtering to achieve the desired end-to-end transfer function. This work was first presented in [1]. In Section 2.2, the characteristics of fluid flow in microfluidic channels and the lumped parameter model is introduced. The analysis of molecular transport in microfluidic channels via flow is presented in Section 2.3. Building blocks of microfluidic channels are analyzed for concentration propagation and end-to-end concentration propagation model is presented in Section 2.4 for each building block, as well as for the overall end-to-end model. In Section 2.5, the design of microfluidic channels for finite impulse filtering via least-squares is presented. Numerical results are presented in Section 2.6.

2.1 Motivation

Microfluidic channels and flow can jointly provide control over propagation of molecules from transmitter to the receiver in MC. Here, we focus on the communication between transmitter and receiver placed in a microfluidic channel in which the fluid flows which constitutes a new MC paradigm, i.e., the Flow-induced Molecular Communications (FMC).

In FMC, the fluid flowing through a microfluidic channel serves as a communication channel and connects patches of molecular transmitter and receiver, such as bacterial habitat [9]. A basic MC scheme over microfludic channel is presented in Fig. 3 where the convection provides transport of released molecules by the transmitter to the receiver over a microfluidic channel. Overall, FMC brings significant advantages over traditional MC, including utilization of flow for enhancing molecular transport and guiding concentration

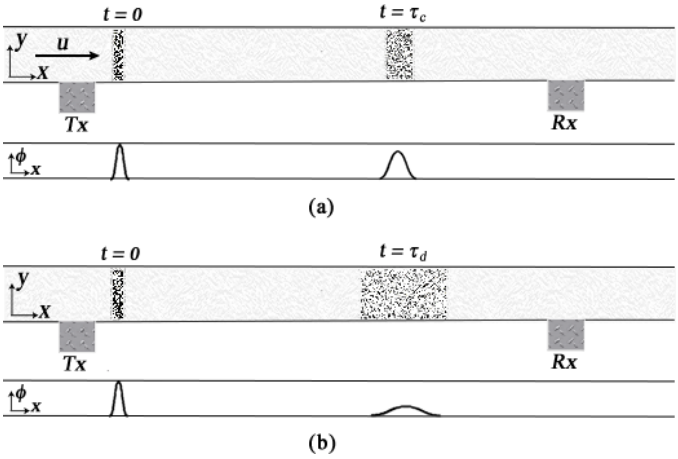

Figure 3: Propagation of the concentration signal from the transmitter (Tx) to the receiver (Rx) patch through the microfluidic channel based on the convection (a) and the diffusion (b). At an arbitrary position, the propagation time of convection based transport with flow velocity u is much less than diffusion based transport, i.e., $\tau_d \gg \tau_c$, which alleviates dispersion of molecules in (a) compared to (b).

propagation via the microfluidic channel. FMC can be used to provide nano communications for a very wide range of emerging applications, specifically in nanomedicine, medical microbiology, and immediate point-of-care testing of samples for biochemical toxins and dangerous pathogens. However, the realization of these envisioned applications depends on an accurate analysis and efficient design of microfluidic channels for FMC.

For the realization of FMC, it is imperative to develop new and efficient communication techniques. The challenges and requirements to be addressed for the analysis and design of microfluidic channels for FMC can be summarized as follows:

- *Modeling the Molecular Transport via Flow inside Microfluidic Channels*: The concentration propagation inside the microfluidic channels must be investigated from the FMC perspective. The solution of the flow rate inside the microfluidic channels must be determined, and the microfluidic channel configurations must be studied to understand the propagation of transmitted molecules.

- *Enhancing the Concentration Propagation via Microfluidic Channel Design*: The shape of microfluidic channels must be optimized to alleviate the dispersion and the

delay between the transmitter and the receiver. The microfluidic channel parameters, i.e., length and cross-section, must be adjusted to enhance the FMC via filtering spectrum of the concentration signal.

All these challenges coupled with the physical limitations of microfluidic channels, immediate diagnosis and treatment requirements for mission critical clinical applications call for a thorough analysis and efficient design of FMC to realize nano communications in biocompatible environments. So far, to the best of our knowledge, there is no prior work on analytical modeling of concentration propagation and design of microfluidic channels from the FMC point of view.

While a channel model solely based on diffusion is proposed in [7], the analysis of noise sources and the communication capacity in diffusion-based concentration propagation have been the main approaches for molecular communication research [10], [11], [12], [13], [37]. Recently, modeling and simulation of concentration propagation in microfluidic channels have been a field of interest [29], [33], [30], [31], [32], [34], [36]. While these studies on microfluidics have been adequate for the analysis of separation, dispersion, and the generation of concentration profiles via microfluidic devices, they do not focus on the communication perspective, which requires the propagation characteristics of the FMC channel to be revealed based on the transmitted concentration signal and the channel parameters. Furthermore, the microfluidics has been considered for networking of lab-on-a-chip systems [14], where possible different configurations of microfluidic technologies are surveyed for droplet-based nano communication. Overall, the incorporation of convection and the inherited features from microfluidics require a new analysis for an accurate and efficient development of communication techniques and design of microfluidic channels.

In this chapter, first, system-theoretic analysis of the FMC is performed which provides a framework to determine the end-to-end concentration propagation in microfluidic channels based on flow velocity and channel configurations, i.e., straight, turning, and interconnections. Then, the least-squares design of microfluidic channels is presented in which physical parameters of microfluidic channels, i.e., interconnection, cross-section and length, are optimized to obtain desired transfer function at the receiver via Finite Impulse Response (FIR)

filtering. To the best of our knowledge, this is the first work on the FMC focusing on the analysis and design of microfluidic channels for end-to-end concentration propagation and finite impulse filtering, respectively. The distinctive features of our work are as follows:

1. **A Flow Model in Microfluidic Channels:** A contemporary overview of fluid flow inside microfluidic channels is presented, and a general technique for deriving flow rate in microfluidic channels is developed. This technique is used to determine the flow rate inside a specific channel for a given microfluidic channel topology.

2. **An End-to-end Concentration Propagation Model:** The molecular transport models are developed by incorporating convection to reveal the attenuation, delay, and the transfer function for the basic microfluidic channel and the interconnection configurations. Using systems theory, the end-to-end concentration propagation model is presented for FMC.

3. **Design of Microfluidic Channels for FIR Filtering:** To enhance the end-to-end FMC, an FIR filtering structure is developed based on the microfluidic channels. For a desired frequency response, the FIR filter coefficients are optimized via least-squares method. The obtained filter coefficients are mapped to transfer function of individual microfluidic channels to determine the length and aspect-ratio.

2.2 Fluid Flow Model

To understand and work with the microfluidic channels, the hydrodynamic behavior of fluids in microchannels must be first understood. Here, we provide a comprehensive look at the physical phenomena of the fluid flow inside microfluidic channels and how it makes the utilization of convection for FMC possible.

The Navier-Stokes equation relating the velocity field $\mathbf{u}$ of the fluid flow to pressure p under the constant density ρ, constant viscosity μ, and conservation of mass ($\nabla \cdot \mathbf{u} = 0$) assumptions is as

$$\rho\left(\frac{\partial \mathbf{u}}{\partial t} + (\mathbf{u}\cdot\nabla)\mathbf{u}\right) = -\nabla p + \mu\nabla^2\mathbf{u} + \mathbf{F} \tag{1}$$

where $\mathbf{F}$ represents the body forces. We assume there is no electrical field acting on the

fluid, and the gravitational body force diminishes due to the hydrostatic pressure gradient [15]. The density ρ of a liquid is in the order of $\approx 10^3 \text{kg/m}^3$ which is comparable to a solid's density for many practical purposes [15]. Therefore, the fluid flows, such as water and aqueous solutions, are well approximated as incompressible, i.e., constant density ρ, in microfluidic channels [16].

To guide design of microfluidic channels for FMC, Navier-Stokes equation is solved analytically in the particular cases. Specifically, the simplification of the Navier-Stokes equation is performed under unidirectional flow through an infinite channel assumption, where the fluid velocity field and the velocity field gradient are orthogonal, i.e., $(\mathbf{u}\cdot\nabla)\mathbf{u} = 0$. Fluid flow is said to be laminar under this condition, and the total flow is formed by the addition of contribution from each lamina. In the following subsections, the fluid flow characteristics and the solution steps of the fluid flow rate for given microfluidic channels are presented.

2.2.1 Characteristics of Flow in Microfluidic Channels

The Reynolds number (Re), which gives the relative importance of inertial and viscous forces, is used to characterize laminar flow in microfluidic channels and is defined as [15]

$$\text{Re} \triangleq \frac{\rho u D_\text{H}}{\mu} \approx \frac{\text{intertial forces}}{\text{viscous forces}} \tag{2}$$

where μ is the viscosity, D_H is the hydraulic diameter of the channel, and u is the characteristic area-averaged velocity depending on the volumetric flow rate Q of the fluid and cross-section area A of the channel. D_H is given by

$$D_\text{H} = \frac{4A}{\chi} \tag{3}$$

where χ is the perimeter of the channel. In a circular cross-section channel with radius r, $D_\text{H} = 2r$ and $u = Q/(\pi r^2)$. For a square channel with the width w, $D_\text{H} = w$ and $u = Q/w^2$. For a rectangular channel with width much greater than height, i.e., $w \gg h$, $D_\text{H} = 2w$ and $u = Q/(wh)$.

In the laminar flow case, i.e., at small Reynolds numbers ($\text{Re} < 2300$) for the smooth channels, the viscous forces are large enough to overcome the inertial forces and to keep the

fluid in line and prevent random rapid fluctuations of the fluid [17]. The fluid flows in microchannels are almost always at low Reynolds number, i.e., $\mathrm{Re} < 1$, due to small hydraulic diameters D_{H} and relatively slow volumetric flow rates Q. Furthermore, in microfluidic channels the inertial effects such as gravity, and turbulence are negligible [18, 19, 20]. The laminar flow and the absence of turbulence are essential to minimize unsteady-state flows at turning channels and connection nodes in microfluidic channels [21]. Moreover, when the distance l from the inlet of a channel with radius r satisfies the condition $l/r \gg \mathrm{Re}$, the laminar flow can be taken as fully-developed, and analysis of infinite channels can be used to analyze flows in finite length channels [16, 15].

2.2.2 Poiseuille Flow

Poiseuille flow is the solution of steady laminar flow in microfluidic channels [16, 15]. Flow in microfluidic channels is defined by perturbation or superposition of Poiseuille flow. In a Poiseuille flow, the flow is driven by pressure, i.e., pressure difference causes the flow, unidirectional, i.e., through only single direction and orthogonal to other axes, and taken to be in steady-state, i.e., there is no acceleration of the fluid [15].

The channel is taken to be parallel to x axis, and its cross-section is invariant. Using the steady flow ($\partial\mathbf{u}/\partial t = 0$), unidirectional velocity field ($u_y = u_z = 0$), fully developed laminar flow ($\partial u_x/\partial x = 0$), and smooth channel $(\mathbf{u} \cdot \nabla)\mathbf{u} = 0$ assumptions, Navier-Stokes equation (1) is simplified as

$$\partial_x p(x) = \mu(\partial_y^2 + \partial_z^2)u_x(y, z) \tag{4}$$

where $u_x(y, z)$ is the only non-zero component of fluid velocity field which is independent of position in x direction and changes based on position in y, and z directions. Furthermore, since velocity field in y, and z directions are zero, the pressure drops in y and z directions are 0. Therefore, due to the constant pressure gradient in the x direction in (4), the pressure difference Δp between the two ends of the microfluidic channel is a linear function of x as

$$p(x) = p(x_0) - \frac{\Delta p}{l}(x - x_0) \tag{5}$$

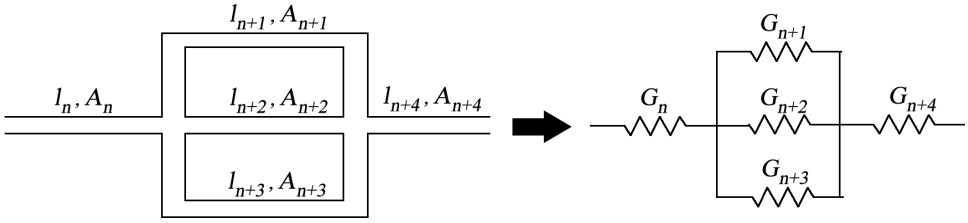

Figure 4: Hydraulic conductance model.

where Δp is equal to $p(l) - p(x_0)$. Replacing (5) into (4), we obtain

$$(\partial_y^2 + \partial_z^2) u_x(y,z) = -\frac{\Delta p}{\mu l} \tag{6}$$

The flow velocity field is taken as zero at the boundaries of the channel, i.e., no-slip boundary condition is employed [15]. The flow in microfluidic channels is characterized by a parabolic velocity field, and the velocity of flow increases towards the center of the channel from the boundaries. The analytic solution of (6) for a rectangular cross-section channel, i.e., u_x^{rect}, is as [15]

$$\begin{aligned} u_x^{\text{rect}}(y,z) =& \frac{4h^2 \Delta p}{\pi^3 \mu l} \\ & \cdot \sum_{n=1,3,5,\cdots}^{\infty} \frac{1}{n^3} \left[1 - \frac{\cosh(\frac{n\pi y}{h})}{\cosh(\frac{n\pi w}{2h})} \right] \sin(\frac{n\pi z}{h}) \end{aligned} \tag{7}$$

where h and w are the height and width of the microfluidic channel, respectively. For an elliptical cross-section, analytic solution of (6), i.e., u_x^{elps}, is found as [15]

$$u_x^{\text{elps}}(y,z) = \frac{\Delta p (a^2 b^2)}{2\mu l (a^2 + b^2)} \left(1 - \frac{y^2}{a^2} - \frac{z^2}{b^2} \right) \tag{8}$$

To have an accurate analysis and prosperous design of microfluidic channels, disruption of laminar flow should be prevented. For low Reynold numbers, i.e. $\text{Re} < 1$, which is typical in microfluidic channels, fluid flow is not exposed to lateral mixing, i.e., turbulence, in turning channels. Due to viscous forces, velocity field gradients in the direction of the axial direction is prevented, i.e., $(\mathbf{u} \cdot \nabla)\mathbf{u} = 0$, and laminar flow is conserved for turning microfluidic channel [22, 23].

2.2.3 Volumetric Flow Rate

Using flow velocity solutions of microchannels, volumetric flow rate Q can be determined as

$$Q \triangleq \int_S u_x(y,z)\mathrm{d}y\mathrm{d}z \tag{9}$$

where S is the area of the cross-section of the microfluidic channel. Therefore, to get the volumetric flow rate in the rectangular channel n, i.e., Q_n^{rect}, we need to spatially integrate the velocity contributions (7) of each lamina as

$$\begin{aligned} Q_n^{\text{rect}} &= \int_0^{w_n}\int_0^{h_n} u_x^{\text{rect}}(y,z)\mathrm{d}z\mathrm{d}y \\ &= \frac{8h_n^3 w_n}{\pi^4 \mu l_n} \sum_{i=1,3,5,\cdots}^{\infty} \left[\frac{1}{i^4} - \frac{2h_n}{\pi w_n i^5}\tanh(\frac{i\pi w_n}{2h_n})\right]\Delta p_n \end{aligned} \tag{10}$$

Using $\sum_{i=1,3,5,\cdots}^{\infty} \frac{1}{i^4} = \pi^4/96$, and for channels with $w \gg h$ using $\tanh(\infty) = 1$, Q_n^{rect} in (10) can be further simplified as [15]

$$Q_n^{\text{rect}} \approx \frac{h_n^3 w_n}{12\mu l_n}\left(1 - 0.630\frac{h_n}{w_n}\right)\Delta p_n \tag{11}$$

Furthermore, flow rate in square channels can easily be obtained via setting $h = w$ as

$$Q_n^{\text{sqre}} \approx 0.370\frac{h_n^4}{12\mu l_n}\Delta p_n \tag{12}$$

However, due to assumption of $w \gg h$ for approximation, flow rate calculations for square channels exposed to error about 13%, while as the w/h ratio increases, this error diminishes, such as for $w/h = 2$ error is about 0.2% [15].

For the elliptical cross-section channel, flow rate is formulated via integration over an elliptically shaped cross-section with major axis radius a and minor axis radius b as

$$\begin{aligned} Q_n^{\text{elps}} &= \int_{-a_n}^{a_n}\int_{-b_n\sqrt{1-x^2/a_n^2}}^{b_n\sqrt{1-x^2/a_n^2}} u_x^{\text{elps}}(y,z)\mathrm{d}y\mathrm{d}z \\ &= \frac{\pi}{4\mu l_n}\frac{a_n^3 b_n^3}{a_n^2 + b_n^2}\Delta p_n \end{aligned} \tag{13}$$

Flow rate for a circular cross-section with radius a can be obtained via setting radius $r = b = a$ in (13) as

$$Q_n^{\text{circ}} = \frac{\pi r_n^4}{8\mu l_n}\Delta p_n \tag{14}$$

Table 1: Summary of Hydraulic Conductance for Different Microchannel Cross-sections

Cross-section	**Hydraulic Conductance**
Rectangular (G_n^{rect})	$\frac{h_n^3 w_n}{12\mu l_n}\left(1-0.630\frac{h_n}{w_n}\right)$
Square (G_n^{sqre})	$0.370\frac{h_n^4}{12\mu l_n}$
Elliptical (G_n^{elps})	$\frac{\pi}{4\mu l_n}\frac{a_n^3 b_n^3}{a_n^2+b_n^2}$
Circular (G_n^{circ})	$\frac{\pi r_n^4}{8\mu l_n}$

It is shown that for Pouseuille flow in microfluidic channels, there exists a linear relationship between volumetric flow rate Q and pressure drop Δp across the channel. This result is called Pouseuille-Hagen law and will be used to develop equivalent circuit theory for flow modeling in FMC.

2.2.4 Hydraulic Conductance and Equivalent Circuit Theory

So far, the calculation of the average flow rate in microfluidic channels is presented. In (11), (12), (13), and (14), for a pressure drop of Δp across the microfluidic channel, a constant flow rate Q is found. This linear relationship yields well-known circuit theory analysis tools applicable to microfluidic channels. The linear relation between flow in the channel and pressure drop across channel, i.e., Hagen-Poiseuille law, is given as

$$Q = G\Delta p \tag{15}$$

where G is the hydraulic conductance of the microfluidic channel. The hydraulic conductance of various cross-sections is presented in the Table 1. For the high aspect ratio rectangular channels, i.e., $h/w \to 0$), the hydraulic conductance of a channel becomes $G_n^{\text{rect}} = h_n^3 w_n/(12\mu l_n)$.

For low Re numbers in microfluidics, the addition of two finite length channels with different cross-section are shown to be still following the Pouiseulle flow definition, i.e., non-accelerating and laminar flow [15, 29]. Therefore, Hagen-Poiseuille law can still be applied, and equivalent conductance of the series added channels can be calculated using circuit

theory as

$$\begin{aligned} G_{\text{eq}} =& \frac{1}{\frac{1}{G_1} + \frac{1}{G_2} + \cdots + \frac{1}{G_N}} \\ =& \frac{\prod_{n=1}^{N} G_n}{\sum_{n=1}^{N} \prod_{\substack{i=1 \\ i \neq n}}^{N} G_i} \end{aligned} \tag{16}$$

where G_n is the conductance of channel n with length l_n, width w_n, and height h_n, i.e., $G_n = G(l_n, w_n, h_n)$. The equivalent conductance for parallel connected microfluidic channels can be obtained as

$$\begin{aligned} G_{\text{eq}} =& G_1 + G_2 + \cdots + G_N \\ =& \sum_{n=1}^{N} G_n \end{aligned} \tag{17}$$

For serial and parallel channels, the flow rate can be obtained from total pressure drop across the channels using (15). Furthermore, since the pressure drop across all parallel connected channels are the same by circuit theory, the total flow is divided among parallel sub-branches directly proportional to hydraulic conductance, as

$$Q_n = \frac{G_n}{G_{\text{eq}}} Q_+ \tag{18}$$

where Q_+ is the entering total flow rate to parallel branches. Moreover, hydraulic resistance of turning microchannels is shown to be equal to the one of the straight channel with the same cross-section and length [22, 23].

Here, we complete the lumped parameter modeling of flow rate in microfluidic channels. The microfluidic channels are modeled by hydraulic conductance based on the linear relation between the flow rate inside and the pressure drop across the channel. In the next subsection, the solution for flow velocity at each channel is formulated by utilizing the presented equivalent circuit model.

2.2.5 Analysis of Microfluidic Circuits for Flow Velocity

To analyze the microfluidic circuit, we use nodal formulation. A conservation of flow equation, i.e., KCL equation, is written for each node, where microfluidic channel n connects two

nodes. There exists one KCL equation for each node k. In matrix form, nodal equations are represented as

$$\mathbf{Gp} = \mathbf{Q_s} \tag{19}$$

where $\mathbf{p} = [p_1, p_2, \cdots, p_K]^{\mathrm{T}}$ for a microfluidic circuit of K nodes, entries of matrix $\mathbf{G}$ are the conductance between two nodes that are connected via single channel, and $\mathbf{Q_s}$ represents the sum of entering flow from flow sources to node k.

When $\mathbf{p}$ is determined, pressure drop across microchannels $\mathbf{\Delta p}$ is determined via the node-to-branch matrix $\mathbf{B}$ as

$$\mathbf{\Delta p} = \mathbf{Bp} \tag{20}$$

where $\mathbf{B}$ is an N-by-K matrix containing two entries of valued 1 with opposite signs at each row, which indicate pressure at which nodes should be subtracted to calculate pressure drop Δp_n for channel n. Then, multiplying pressure drop with hydraulic conductance of channels, flow rate across channels is found as

$$\mathbf{Q} = \mathbf{G_c}\mathbf{\Delta p} \tag{21}$$

where $\mathbf{Q} = [Q_1, Q_2, \cdots, Q_N]$ with Q_n is the flow rate in channel n, and $\mathbf{G_c}$ is a diagonal matrix with entries G_n for $n = 1, \cdots, N$.

Finally, area-averaged velocity u of fluid is obtained via dividing volumetric flow rate Q by cross-section area A of the microfluidic channels as

$$\mathbf{u} = \mathbf{A}^{-1}\mathbf{Q} \tag{22}$$

where $\mathbf{u} = [u_1, u_2, \cdots, u_N]$ with u_n is the area-averaged flow velocity in channel n, and $\mathbf{A}^{-1}$ is a diagonal matrix whose entries are reciprocal of channel cross-section area, i.e., $A_n^{-1} = 1/A_n$. Next, molecular transport analysis is conducted by incorporating flow velocity model tailored for FMC.

2.3 Molecular Transport Analysis

Molecules are subject to the convection-diffusion through the microfluidic channels with the effect of flow. We assume there is no existing concentration in the channel, i.e., system is

at rest. Molecules are released to or collected from the microfluidic channels by molecular transmitter and receiver, respectively. Here, we, first, formulate impulse response, transfer function, and delay of the concentration propagation through microfluidic channels for the FMC. Then, we investigate the duality of time-invariant and transnational-invariant properties of concentration propagation.

2.3.1 Impulse Response

The convection-diffusion equation is used to define behavior of mass transport inside flowing fluid. It is a linear partial differential equation defined as

$$\frac{\partial \phi}{\partial t} = -u\nabla\phi + D\nabla^2\phi \tag{23}$$

where D is the diffusion constant adjusted based on the cross-section parameters of the microfluidic channel due to the Taylor dispersion [24]. The convection-diffusion equation relates to the change of concentration ϕ in time on the left hand side, i.e., $\partial\phi/\partial t$, to convection ($u\nabla\phi$) and diffusion ($D\nabla^2\phi$) terms on the right hand side. Due to linearity property, solution for end-to-end concentration propagation can be written as linear combination of propagation in building blocks, such as straight and turning channels, and interconnections.

In Section 2.2, it is shown that fluid flow is unidirectional and is in x direction in microfluidic channels. Therefore, the concentration is invariant in the other directions. To analyze the molecular transport in microfluidic channels, the one-dimensional solution of convection-diffusion in the direction of flow, i.e., x, is sufficient to capture the convection-driven transport of molecules [29, 33, 30, 31, 32]. The finite amount of concentration injected ϕ into the flow in microfluidic channel at an instant t_0 by a point source located at x_0 can be modeled as an impulse using the Dirac delta function δ as

$$\phi(x,t) = \frac{M}{A}\delta(x - x_0, t - t_0) \tag{24}$$

where M is the amount of the mass, and A is the cross-section area, then M/A gives the mass per unit area. For a unity concentration, i.e., $M/A = 1$, response to such an input, i.e., impulse response, is obtained as [15]

$$h(x,t) = \frac{1}{\sqrt{4\pi D(t - t_0)}} \exp\Big(- \frac{(x - (x_0 + u(t - t_0)))^2}{4D(t - t_0)}\Big) \tag{25}$$

Defining $l = x - x_0$, and $\tau = t - t_0$, impulse response becomes

$$h(l,\tau) = \frac{1}{\sqrt{4\pi D\tau}} \exp\big(-\frac{(l-u\tau)^2}{4D\tau}\big) \tag{26}$$

2.3.2 Transfer Function

The frequency response of the channel to an impulse, i.e., transfer function, can be found via solving the frequency domain equivalent of convection-diffusion equation (23). Fourier transform of (23) is found by converting the derivative in time domain to multiplication with $j2\pi f$ in frequency domain as

$$j2\pi f\Phi(l,f) = -u\frac{\partial\Phi(l,f)}{\partial l} + D\frac{\partial^2\Phi(l,f)}{\partial l^2} \tag{27}$$

where Φ is the concentration spectral density, which is found by Fourier transform of concentration, i.e., $\Phi = \mathcal{F}\{\phi\}$. Using boundary conditions $\Phi(0,f) = 1$ and $\Phi(\infty,f) = 0$, the transfer function is obtained as

$$H_t(l,\omega) = e^{(u(1-\sqrt{1+\frac{j4\omega D}{u^2}})\frac{l}{2D})} \tag{28}$$

where the temporal frequency f is converted to angular frequency ω using identity $\omega = 2\pi f$. Assuming $|j4\omega D/u^2| < 1$, to have a converging series expansion, $\sqrt{1+j4\omega D/u^2}$ can be approximated as $1 + j2\omega D/u^2 + 2\omega^2 D^2/u^4$. Finally, we approximate the transfer function as

$$H_t(l,\omega) \approx e^{-(\frac{\omega^2 D}{u^3} + j\frac{\omega}{u})l} \tag{29}$$

where we assume $4\omega D/u^2 < 1$ during the derivation, the implication and the practicality of which is further elaborated in Section 2.3.4.

2.3.3 Delay

Propagation delay τ for traveling time of peak concentration level $\max_\tau ||\phi||$ to a distance l is found via setting $\partial h(l,\tau)/\partial\tau = 0$ as

$$De^{-\frac{(l-\tau u)^2}{4D\tau}} \frac{\big(l^2 - \tau(2D + \tau u^2)\big)}{8\sqrt{\pi}(D\tau)^{5/2}} = 0 \tag{30}$$

which yields

$$\tau = \frac{1}{u}\sqrt{\frac{D^2}{u^2} + l^2} - \frac{D}{u^2} \tag{31}$$

The dominance of convection over diffusion is determined by the dimensionless Peclet number (Pe) which is defined as $\mathrm{Pe} = ul/D$. For a large value of Pe, the molecular transport is said to be dominated by the convection, and for small Pe values, the transport is dominated by the diffusion. Using definition of Pe number, (31) is rewritten. Furthermore, since the molecular transport is dominated by the convection, i.e., $\mathrm{Pe} \gg 1$, and l is in the order of $\sim 10^{-2}$m, τ is approximated as

$$\begin{aligned}\tau =& \frac{1}{u}\sqrt{\frac{l^2}{\mathrm{Pe}^2} + l^2} - \frac{l}{u}\frac{1}{\mathrm{Pe}} \\ \approx& \frac{l}{u}(1 + \frac{1}{\mathrm{Pe}}) \\ \approx& \frac{l}{u}\end{aligned} \tag{32}$$

Since the delay is characterized by the length of the channel l and fluid flow velocity u, we express concentration, and impulse response for microfluidic channels based on distance l. Next, we investigate the spatial frequency response H_s due to translational-invariance apart from temporal frequency response H_t derived previously based on time-invariance.

2.3.4 Duality of Transfer Function

Here, we focus on derivation of spatial transfer function H_s and relate it to temporal frequency response H_t. To obtain H_s, we take the Fourier Transform of the impulse response with respect to spatial parameter l as

$$H_s(\nu) = \int_{-\infty}^{\infty} \frac{1}{\sqrt{4\pi D\tau}} e^{-\frac{(l-u\tau)^2}{4D\tau}} e^{-j2\pi\nu l} \mathrm{d}l \tag{33}$$

where ν is the spatial frequency and given by $\nu = 1/\lambda$ for a concentration signal with wavelength λ. We obtain transfer function based spatial frequency as

$$H_s(k) = e^{-(k^2 D + jku)\tau} \tag{34}$$

where k is the wave number defined as $k = 2\pi\nu$. The obtained transfer functions based on spatial frequency H_s and temporal frequency H_t, can be converted using the identity

$$\lambda f = u \tag{35}$$

which is the dual of the equality $\lambda f = c$ in electromagnetic waves, where c is the speed of light. Wave number k based on spatial frequency ν is converted to angular frequency ω based on temporal frequency f as

$$k = \frac{\omega}{u} \tag{36}$$

and temporal transfer function H_t can be obtained from spatial transfer function H_s by changing k to ω/u and τ to l/u. We use transfer function based on spatial frequency for analysis of concentration in microfluidic building blocks, and refer it as transfer function H.

During the derivation of the transfer function based on the temporal frequency, we assume $4\omega D/u^2 < 1$, which is related to the Pe as

$$k < \frac{\mathrm{Pe}}{4l} \tag{37}$$

In the microfluidic devices, Pe is in the range of $10 < \mathrm{Pe} < 10^5$ [25], and the considered distances are in the order of $\approx$ 10mm. Therefore, the given upper limit on the frequency, i.e., $\mathrm{Pe}/(4l)$, is far beyond the physically achievable frequencies due to the attenuation, which yields the assumption of $4\omega D/u^2 < 1$ practically meaningful.

2.4 Microfluidic Building Blocks and End-to-end Concentration Propagation in FMC

Closed-form and end-to-end models simplify the analysis and enable efficient-design of molecular communication techniques. In this section, our objective is to obtain the end-to-end concentration propagation model of FMC based on microfluidic building blocks. Therefore, we investigate the channels based on straight and turning configurations, and interconnections based on bifurcation and combining connections.

2.4.1 Channel Configurations

Here, we develop end-to-end propagation models for straight and turning channel configurations, which are illustrated in Fig. 5(a) and (b), respectively. To this end, impulse response, delay, and transfer function are determined.

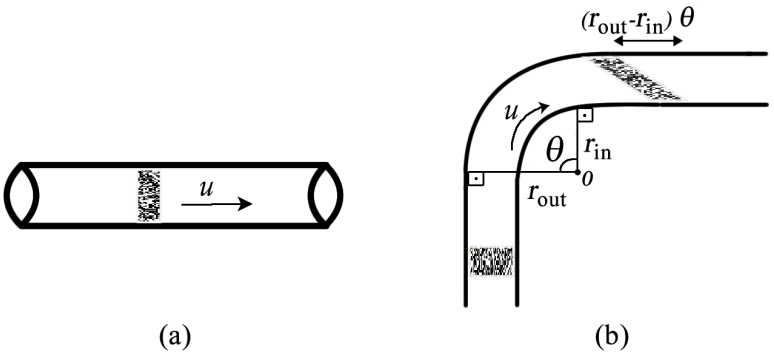

Figure 5: The building block shapes for straight (a) and turning (b) microfluidic channel configurations.

2.4.1.1 Straight Channels

Concentration propagation inside straight channel is illustrated in Fig. 5(a). Impulse response of the straight channel is found in (26), here we parametrize it according to channel specific variables as

$$h_{\text{str}}(l) = \frac{1}{\sqrt{4\pi D\tau}} \exp\left(-\frac{(l-u\tau)^2}{4D\tau}\right) \tag{38}$$

where u is the flow velocity in the microfluidic channel, and τ is the delay of the microfluidic channel given by $\tau_{\text{str}} = l/u$. For an input concentration ϕ_+ into straight microfluidic channel, the output concentration ϕ_- can be obtained via convolution of input and impulse response $(h_{\text{str}} * \phi_+)(l)$ as

$$\phi_-(l) = \int_{-\infty}^{+\infty} h_{\text{str}}(x)\phi_+(l-x)\mathrm{d}x \tag{39}$$

Transfer function of straight channel is derived in (34), and it is parametrized as

$$H_{\text{str}}(k) = e^{-(k^2D+jku)\tau} \tag{40}$$

Spectrum of the output concentration can be obtained via multiplication of transfer function and input concentration spectrum $\Phi_-(k) = H(k)\Phi_+(k)$.

2.4.1.2 Turning Channels

Here, we extend our model for straight channels to turning channels. In Section 2.2.2, we have pointed out the invariance of flow velocity at turning channels in microfluidics

[22, 23]. Due to turning, inner and outer radius of the channel are different, which causes different laminas to travel different lengths [26]. Using the linearity property, we calculate propagation of concentration for each lamina using the straight channel model, then add the contribution from each lamina to reach impulse response of the turning channel. The concentration propagation inside the turning microfluidic channel is illustrated in Fig. 5(b), in which turning angle θ, and the radius of the inner and the outer wall of the turning microfluidic channel, i.e., r_{in} and r_{out}, respectively, are depicted as well.

Vertex of θ is defined as the intersection point O of the lines drawn orthogonal to the inner or outer walls at the end of the straight microfluidic channels. Lengths of these drawn lines give radiuses of the the inner or outer wall of the turning microfluidic channel, i.e., r_{in} or r_{out}, based on whether they are drawn orthogonal to the inner or the outer wall, respectively. When circles are drawn using defined inner and outer radiuses with centre point O, the arcs that are subtending angle θ give the inner and outer walls, respectively, of the turning channel which connects two straight microfluidic channels.

We define r_Δ as the difference of the radius of the outer and the inner wall of the microfluidic channel as

$$r_\Delta = r_{\text{out}} - r_{\text{in}} \tag{41}$$

Using (38), for each lamina in the flow, impulse response is

$$h_\Delta(l) = \frac{1}{r_\Delta \theta} \frac{1}{\sqrt{4\pi D\tau}} e^{-\frac{(l-u\tau+x')^2}{4D\tau}} \tag{42}$$

where θ is the angle of turn, x' is the change in the traveled path with respect to the axial length l due to turning shape. Contributions from each lamina are integrated and the impulse response for the turning channel is found as

$$h_{\text{turn}}(l) = \frac{1}{r_\Delta \theta} \int_{-\frac{r_\Delta \theta}{2}}^{\frac{r_\Delta \theta}{2}} \frac{1}{\sqrt{4\pi D\tau_{\text{turn}}}} e^{-\frac{(l-u\tau+x')^2}{4D\tau_{\text{turn}}}} \mathrm{d}x' \tag{43}$$

where τ_{turn} is taken as the average delay of the laminas in the turning microfluidic channel and is found according to the symmetry around central lamina as $\tau_{\text{turn}} = (l + r_\Delta \theta/2)/u$. Impulse response of a turning channel h_{turn} is the same as an ideal integrator with an

equivalent axial length straight microfluidic channel

$$h_{\text{turn}}(l) = (h_{\text{str}} * \frac{h_{\text{int}}}{r_\Delta \theta})(l) \tag{44}$$

where h_{str} is the impulse response of a straight channel having same length with the central arc length of the turning channel, and h_{int} is

$$h_{\text{int}}(l) = \begin{cases} 1, & |l| \leq \frac{r_\Delta \theta}{2} \\ 0, & |l| > \frac{r_\Delta \theta}{2} \end{cases}$$

The transfer function of a turning channel is obtained via Fourier Transform of the (43) as

$$\begin{aligned} H_{\text{turn}}(k) = &\int_{-\infty}^{\infty} \frac{1}{r_\Delta \theta} \\ &\cdot \int_{-\frac{r_\Delta \theta}{2}}^{\frac{r_\Delta \theta}{2}} \frac{1}{\sqrt{4\pi D \tau_{\text{turn}}}} e^{-\frac{(l - u\tau_{\text{turn}} + x')^2}{4D\tau_{\text{turn}}}} \mathrm{d}x' e^{-jkl} \mathrm{d}l \\ =&e^{-(k^2 D + jku)\tau_{\text{turn}}} \cdot \frac{\sin(r_\Delta \theta k/2)}{r_\Delta \theta k/2} \end{aligned} \tag{45}$$

which is the frequency response of corresponding integrator

$$H_{\text{turn}}(k) = H_{\text{str}}(k) H_{\text{int}}(k) \tag{46}$$

where H_{int} is defined using normalized sinc function as

$$\begin{aligned} H_{\text{int}}(k) =& \frac{\sin(r_\Delta \theta k/2)}{r_\Delta \theta k/2} \\ =& \text{sinc}(\frac{r_\Delta \theta}{2\pi} k) \end{aligned} \tag{47}$$

Therefore, turning channel can be seen as an integrator which is a low-pass filter.

Since the obtained impulse response, delay, and transfer function formulations respond to a signal in a future position, we shift them by $r_\Delta \theta/2$ to make them causal and obtain the impulse response, delay, and transfer function for turning channel as

$$h_{\text{turn}}(l) = \frac{1}{r_\Delta \theta} \int_0^{r_\Delta \theta} \frac{1}{\sqrt{4\pi D \tau_{\text{turn}}}} e^{-\frac{(l - u\tau_{\text{turn}} + x')^2}{4D\tau_{\text{turn}}}} \mathrm{d}x' \tag{48}$$

where delay is given by $\tau_{\text{turn}} = (l + r_\Delta \theta)/u$. Furthermore, shifted transfer function is as

$$H_{\text{turn}}(k) = e^{-(k^2 D + jku)\tau_{\text{turn}}} \text{sinc}(\frac{r_\Delta \theta}{2\pi} k) e^{-jk r_\Delta \theta/2} \tag{49}$$

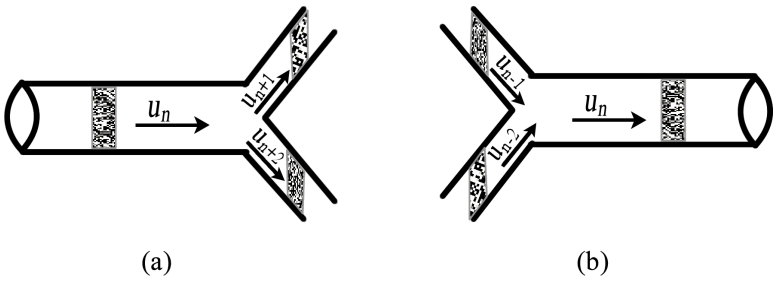

Figure 6: Building block shapes for bifurcation (a) and combining (b) interconnection configurations.

2.4.2 Interconnection Configurations

Here, we model concentration propagation for interconnection of multiple channels, which are illustrated in Fig. 5(a) and (b) for bifurcation and combining, respectively. There is no pressure drop and delay in interconnection models. Pressure drop and delay are given by the channels connected to the interconnection node. Overall, we find effect of bifurcation and combining on concentration and spectral density.

2.4.2.1 Bifurcating Interconnection

In bifurcating connection, flow is separated proportional to conductance G_n of the diverging microfluidic channels. By conservation of mass, concentration divergence to channels, i.e., ϕ_n^-, from inlet concentration ϕ_+, is formulated as

$$\phi_n^-(l) = \frac{G_n}{G_{\text{eq}}}\phi_+(l) \tag{50}$$

Similarly, bifurcating channel results in down scale of the output concentration spectral density as

$$\Phi_n^-(k) = \frac{G_n}{G_{\text{eq}}}\Phi_+(k) \tag{51}$$

Therefore we define transfer function of the bifurcating channel as

$$H_n^{\text{bif}} = \frac{G_n}{G_{\text{eq}}} \tag{52}$$

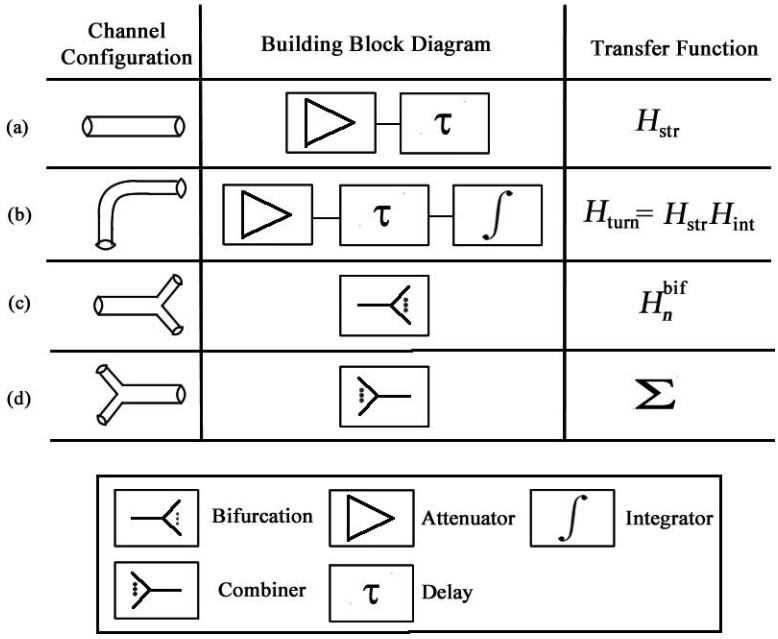

Figure 7: Building blocks of microfluidic channels for end-to-end molecular transport analysis.

2.4.2.2 Combining Interconnection

Combining connection is composed of converging channels. Output concentration ϕ_- is given by the addition of entering concentration from connected channels, i.e., ϕ_n^+, as

$$\phi_-(l) = \sum_{n=0}^{N} \phi_n^+(l) \tag{53}$$

Accordingly, output spectrum becomes the addition of the converging concentrations

$$\Phi_-(l) = \sum_{n=0}^{N} \Phi_n^+(l) \tag{54}$$

2.4.3 The End-to-end Model of Concentration Propagation

The end-to-end model is developed using the system-theoretic molecular transport analysis of the microfluidic building blocks, which are summarized in Fig. 7, and provides the impulse response, delay, and transfer function for concentration propagation in FMC.

End-to-end impulse response of an arbitrary microfluidic circuit h_{e2e} is determined via convolution of the impulse response of each building block as

$$h_{\text{e2e}}(l) = (h_1 * h_2 * \cdots * h_N)(l) \tag{55}$$

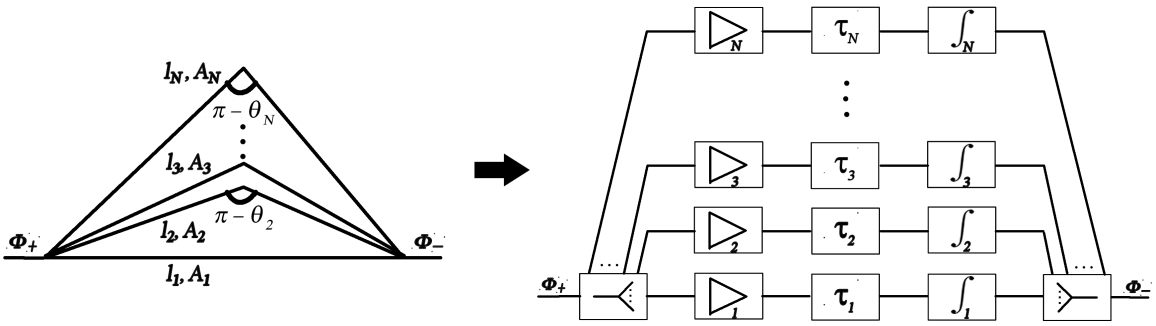

Figure 8: Microfluidic and building block representation of FIR filter.

and for a given transmitted molecular concentration, received concentration level is obtained as

$$\phi_-(l) = (h_{\text{e2e}} * \phi_+)(l) \tag{56}$$

where ϕ_- and ϕ_+ are received and transmitter concentration levels, respectively. Performed system-theoretic analysis for molecular transport in FMC is also utilized to determine end-to-end propagation delay τ_{e2e} via addition of delay of each building blocks as

$$\tau_{\text{e2e}} = \sum_n \tau_n \tag{57}$$

Lastly, the end-to-end transfer function can be determined using performed system-theoretic analysis via multiplying frequency response of building blocks of microfluidic circuit as

$$H_{\text{e2e}}(k) = \prod_n H_n(k) \tag{58}$$

and the spectrum of the received molecular concentration is obtained for a given transmitted concentration as

$$\Phi_-(k) = H_{\text{e2e}}(k)\Phi_+(k) \tag{59}$$

where Φ_- and Φ_+ are the received and transmitted concentration spectrum, respectively. The developed end-to-end model is used to design microfluidic circuits to yield desired end-to-end transfer function H_{e2e} at the receiver.

2.5 Least-squares FIR Filtering via Microfluidics

In this section, the utilization of microfluidic channels to create an FIR filter is presented. Specifically, least-squares FIR filtering is used to optimize microfluidic channel parameters

according to desired concentration spectral density (CSD).

Suppose we want to design an FIR filter for a given set of frequency domain constraints, i.e., pass and stop bands. For a given constant pressure drop across the microfluidic channels that are first bifurcating then combining as in Fig. 8 between transmitter and receiver, transfer function of individual channels can be adjusted via proper design of length and the cross-section of the channels such that desired FIR filtering operation can be achieved. To this end, first, we give overview of linear least-squares filter design, then show mapping of channel parameters according to obtained filter coefficients, and we derive the required aspect-ratio of the channel. Lastly, we outline design steps for microfluidic channels, and formulate end-to-end transfer function.

2.5.1 Overview of Linear Least-squares Filter Design

Transfer function of an FIR filter is given by

$$H(k) = \sum_{n=-N}^{N} \alpha_n e^{-jkn} \tag{60}$$

where $2N + 1$ is the order of the FIR filter. An empirical FIR filtering structure using microfluidic channels is illustrated in Fig. 8. The coefficient sequence α_n is symmetric, i.e., $\alpha_n = \alpha_{-n}$, to have a linear phase filter. The desired frequency response is represented in terms of pass- and stop-bands in the frequency domain $[0, \pi]$. In each pass- and stop-band, the frequency is sampled with k_{sample} spacing, and $M = \pi / k_{\text{sample}}$ is the number of frequencies resulting from frequency domain sampling, such that the frequency response is discretized into M linear equations of the form

$$H(k_m) = \alpha_0 + 2 \sum_{n=1}^{N} \alpha_n \cos(k_m n) \tag{61}$$

where k_ms are the frequencies whose frequency responses are calculated for $m = 1, \cdots, M$. To determine the corresponding filter coefficients to the given desired output concentration spectrum, we define $\boldsymbol{\alpha}$ which contains filter coefficients to be found, $\mathbf{z}$ as the vector containing desired magnitude of the transfer function at frequencies k_m. Overall, state space representation of the system is given as

$$\mathbf{z} \cong \boldsymbol{\Lambda} \boldsymbol{\alpha} \tag{62}$$

where $\boldsymbol{\alpha} = [\alpha_0, \cdots, \alpha_N]^{\mathrm{T}}$, $\mathbf{z} = [H(k_1), \cdots, H(k_M)]^{\mathrm{T}}$, and $\boldsymbol{\Lambda}$ is an M-by-$(N+1)$ matrix as

$$\boldsymbol{\Lambda} = \begin{bmatrix} 1 & 2\cos(k_1) & 2\cos(2k_1) & \cdots & 2\cos(Nk_1) \\ 1 & 2\cos(k_2) & 2\cos(2k_2) & \cdots & 2\cos(Nk_2) \\ \vdots & \vdots & \vdots & \ddots & \vdots \\ 1 & 2\cos(k_M) & 2\cos(2k_M) & \cdots & 2\cos(Nk_M) \end{bmatrix} \tag{63}$$

The least-squares optimization problem is formulated as

$$\min_{\boldsymbol{\alpha}} ||\boldsymbol{\Lambda}\boldsymbol{\alpha} - \mathbf{z}||_2 \tag{64}$$

which is equivalent to minimizing quadratic error function J defined as

$$\begin{aligned} J(\boldsymbol{\alpha}) \triangleq & ||\boldsymbol{\Lambda}\boldsymbol{\alpha} - \mathbf{z}||_2^2 \\ = & \boldsymbol{\alpha}^{\mathrm{T}}\boldsymbol{\Lambda}^{\mathrm{T}}\boldsymbol{\Lambda}\boldsymbol{\alpha} - \boldsymbol{\alpha}^{\mathrm{T}}\boldsymbol{\Lambda}^{\mathrm{T}}\mathbf{z} - \mathbf{z}^{\mathrm{T}}\boldsymbol{\Lambda}\boldsymbol{\alpha} + \mathbf{z}^{\mathrm{T}}\mathbf{z} \end{aligned} \tag{65}$$

To minimize J, by taking derivative with respect to $\boldsymbol{\alpha}$ and equating to 0, it is found that

$$\boldsymbol{\Lambda}^{\mathrm{T}}\boldsymbol{\Lambda}\boldsymbol{\alpha} = \boldsymbol{\Lambda}^{\mathrm{T}}\mathbf{z} \tag{66}$$

For a given desired frequency response constraints composed of desired magnitude at pass-band frequency ranges and suppression at stop-band frequency ranges, the FIR filter coefficients can be determined via least-squares method as

$$\boldsymbol{\alpha} = \left[\left(\boldsymbol{\Lambda}^{\mathrm{T}}\boldsymbol{\Lambda}\right)^{-1}\boldsymbol{\Lambda}^{\mathrm{T}}\right]\mathbf{z} \tag{67}$$

where $\boldsymbol{\alpha}$ contains the obtained filter coefficients via least-squares method. Non-positive α_n values are dropped, as well as non-positive length channels as

$$H(k) = \sum_{n=1}^{N} \alpha_n e^{-j\beta_n} \tag{68}$$

where $\beta_n = kn$, and linear phase property no longer holds. Obtained filter coefficients, i.e., α_n, and complex exponential exponents, i.e., β_n, are mapped to length and cross-section parameters of microfluidic channels to achieve the desired transfer function between transmitter and receiver in FMC.

2.5.2 Length and Area Design of Microfluidic Channels

Here, we map the filter parameters, i.e., α and β, in (68) to microfluidic channel parameters, i.e., length and cross-section area, based on the transfer function of microfluidic building blocks in Fig. 7 and pressure drop constraint Δp. The FIR filter consisting of tapped microfluidic channels in the shape of nested isosceles triangles is depicted in Fig. 8.

The obtained α_n values using least-squares optimization in (67) are normalized due to dropped non-positive values and mapped to the microfluidic channel transfer function (40) as

$$\alpha_n = e^{-k^2 D \tau_n} \tag{69}$$

from which we obtain the desired delay in microfluidic channel n as

$$\tau_n = -\frac{\ln(\alpha_n)}{k^2 D} \tag{70}$$

The complex exponential exponents, i.e., β_n, are mapped using (40) and (68) as

$$\beta_n = k u_n \tau_n \tag{71}$$

Using $l_n = u_n \tau_n$, and $\beta_n = kn$, the required length of the microfluidic channel n is found as

$$l_n = Ln \tag{72}$$

where $n = 1, \cdots, N$, and L is defined as the scaling factor for length of the microfluidic channels, i.e. l_n values are calculated as integer multiples of L as $l_n = Ln$. Furthermore, L provides frequency scaling of the overall frequency response of the FIR filter, such that fine-tuning of pass- and stop-band frequencies of the FIR filter can be performed, which is further elaborated via numerical results in Section 2.6.2.

Using (32), (70), and (72), the required area-averaged flow velocity u_n at the microfluidic channel n is found as

$$u_n = -\frac{k^2 D n}{\ln(\alpha_n)} \tag{73}$$

Furthermore, the cross-section area of the channel must be adjusted accordingly by equating flow velocity u_n to pressure drop constraint Δp_n. Using (15), (22), and (73), required cross-section area is formulated as

$$A_n = -\frac{\ln(\alpha_n) Q_n}{k^2 D n} \tag{74}$$

Next, based on formulated cross-section area of microfluidic channels, we derive required aspect ratio of them.

2.5.3 Aspect Ratio Design of Microfluidic Channels

In this section, using (74) and formulated linear conductance relation between Δp and u for rectangular, square, elliptical, and circular cross-sections in Section 2.2.3, required aspect-ratio of microfluidic channels are determined.

2.5.3.1 Rectangular and Square Cross-sections

Using conductance for a rectangular channel G_n^{rect} given in the Table 1 and (74), we end up with the equality

$$w_n h_n = -\frac{\ln(\alpha_n) h_n^3 w_n \Delta p_n}{12\mu k^2 D n^2} \left(1 - 0.630 \frac{h_n}{w_n}\right) \tag{75}$$

We define aspect ratio of the rectangular channel as $\gamma = w/h$, and replacing width w with γh, we obtain γ as

$$\gamma_n^{\text{rect}} = \frac{0.63 h_n^2 \Delta p_n}{h_n^2 \Delta p_n + \frac{12\mu k^2 D n^2}{\ln(\alpha_n)}} \tag{76}$$

Using the determined α_n in (67), for a given height h_n and Δp_n, the channel cross-sections can be designed according to desired filtering operation. Furthermore, for a square channel γ_n is equal to 1, and h_n can be obtained as

$$h_n = \sqrt{-\frac{12\mu k^2 D n^2}{0.37 \Delta p_n \ln(\alpha_n)}} \tag{77}$$

2.5.3.2 Elliptical and Circular Cross-sections

Using conductance for an elliptical microfluidic channel G_n^{ellps} given in the Table 1 and area formulation in (74), the following equality is found for cross-section of the microfluidic channel

$$a_n b_n = -\frac{\ln(\alpha_n)}{4\mu k^2 D n^2} \frac{a_n^3 b_n^3}{a_n^2 + b_n^2} \Delta p_n \tag{78}$$

Aspect ratio of the elliptical microfluidic channel is defined as the ratio of the major axis length to minor axes as $\gamma = a/b$ from which we can obtain desired aspect ratio γ_n^{ellps} as follows

$$\gamma_n^{\text{ellps}} = \sqrt{-\frac{4\mu k^2 D n^2}{\ln(\alpha_n) b_n^2 \Delta p_n + 4\mu k^2 D n^2}} \tag{79}$$

For a circular channel radius $r = a = b$, desired radius can be found as

$$r_n = 2\sqrt{-\frac{2\mu k^2 D n^2}{\ln(\alpha_n)\Delta p_n}} \tag{80}$$

2.5.4 Overview of Microfluidic Channel Design

Here, we summarize the design procedure for microfluidic channels. The calculation of required microfluidic channel length and aspect ratio corresponding the desired frequency response is presented step-by-step.

To form the tapped delay line FIR filter via linear least-squares filtering, overall design procedure can be grouped under three main steps as follows

1. From the given desired pass and stop bands of the frequency response, the channel design problem is formulated as a least-squares FIR filtering problem as presented in (62).

2. From the formulated least-squares problem, required α and β values are determined for each microfluidic channel to be mapped to microfluidic channel parameters.

3. Obtained α and β values enable the design of a tapped delay line filter using microfluidic channels. Length and cross-section aspect ratio of channels are designed according to the found α and β, and the given cross-section shape and pressure-drop between the transmitter and the receiver.

The output spectrum of the devised microfluidic FIR filter is given by

$$\begin{aligned}\Phi_-(k) &= \sum_{n=1}^{N} H_n^{\text{str}}(k) H_n^{\text{int}}(k) \Phi_+(k) \\ &= \sum_{n=1}^{N} e^{-k^2 D \tau_n} e^{-jkLn} \text{sinc}(\frac{r_n^{\Delta}\theta_n}{2\pi}k) \Phi_+(k)\end{aligned} \tag{81}$$

where H_n^{str} is the transfer function of the microfluidic channel n with the length l_n, the aspect ratio γ_n, and the pressure drop Δp_n; H_n^{int} is the transfer function of the turn n with the angle $\theta_n = \pi - 2\arcsin(l_1/(2l_n))$, and the difference of inner and outer radius r_n^{Δ}.

This concludes our discussion on design of microfluidic circuits. Next, we present numerical results, and discuss the accuracy and practical issues regarding the performance of the microfluidic channel design.

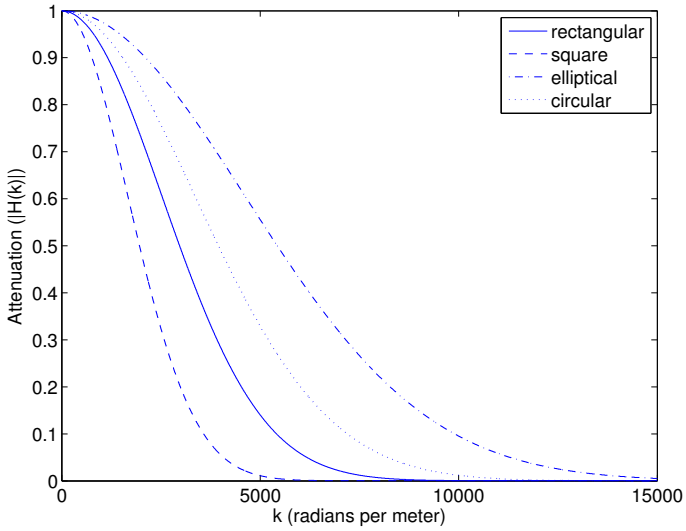

(a)

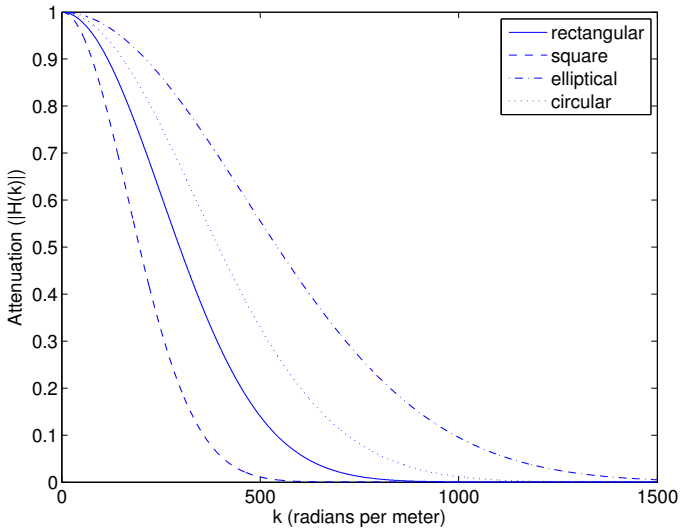

(b)

Figure 9: Attenuation of the concentration propagation in the straight channel. The magnitude of the transfer functions with different cross-sections against wave number k, for the channel lengths of 10mm and 100mm in (a) and (b), respectively.

Table 2: Summary of Flow Velocities (u) in Different Channel Cross-sections

Cross-section	$l = 10 \cdot 10^{-3}$m	$l = 100 \cdot 10^{-3}$m
Rectangular	$1.27 \cdot 10^{-4}$ m/s	$1.27 \cdot 10^{-5}$ m/s
Square	$5.55 \cdot 10^{-5}$ m/s	$5.55 \cdot 10^{-6}$ m/s
Elliptical	$4.25 \cdot 10^{-4}$ m/s	$4.25 \cdot 10^{-5}$ m/s
Circular	$2.25 \cdot 10^{-4}$ m/s	$2.25 \cdot 10^{-5}$ m/s

2.6 Numerical Results

In this section, we, first, study the transfer functions developed for FMC in microfluidic channels. Specifically, we investigate the effect of channel cross-section and length for straight channels, and effect of turning angle θ and difference of inner and outer turning radius r_Δ for turning channels. Then, example design of band-pass and band-stop filters via least-squares FIR filtering are presented for FMC. During numerical evaluations, viscosity μ of the fluid is set to 10^{-3}Pa·s, and diffusion constant D is set to $10 \cdot 10^{-10}$m^2/s. Furthermore, the results presented in Fig. 9−12 with respect to the wave number k can be converted to the angular frequency ω using the identity given in (36).

2.6.1 Concentration Propagation

The concentration propagation is studied in two parts, i.e., straight and turning channels. For straight channels with rectangular, square, elliptical, and circular cross-sections, transfer function is investigated for channel length l of 10 and 100mm. For turning channels with varying turn angles θ, the transfer function is investigated for inner and outer radius differences r_Δ of 50 and 100μm. The pressure drop Δp across channels is set to 500Pa.

2.6.1.1 Straight Channel

For rectangular channels, height is $h = 6\mu$m and width is $w = 25\mu$m. For the square microfluidic channels, height is $h = 6\mu$m. For the elliptical microfluidic channels, major axis radius is $a = 25\mu$m, minor axis radius is $b = 6\mu$m. For circular channel, radius is $r = 6\mu$m. Results for channel length $l = 10$mm and 100mm are presented in Fig. 9. The corresponding flow velocities u are tabulated in the Table 2.

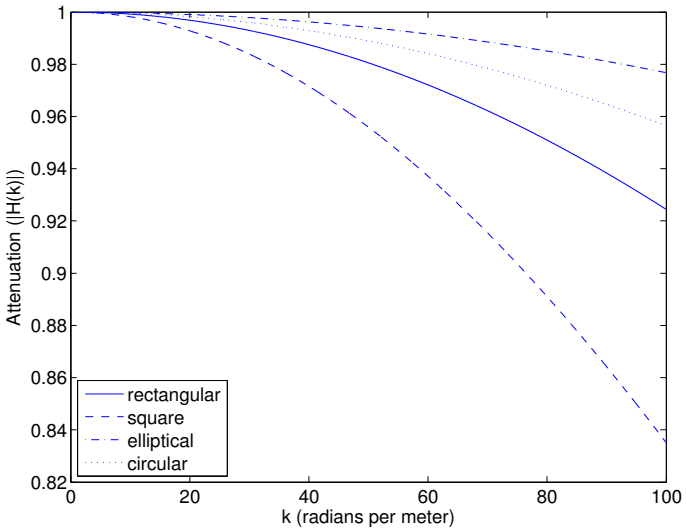

Figure 10: Attenuation of the concentration propagation for a low range of frequencies representing the spectrum of interest for the bacteria-based biological oscillator applications. The magnitude of the transfer functions with different cross-sections against the wave number k, for a straight channel with a length of 100mm.

The concentration signals with higher frequency can be transported with less attenuation between a transmitter and receiver pair in the elliptical and the circular channels compared to the rectangular and the square channels. When the channel length is increased from 10mm to 100mm, the achievable frequencies are decreased in the order of 10 from Fig. 9(a) to (b). The achievable frequencies in the channels are inversely scaled by the rate of increase in the distance between transmitter and receiver.

The presented results in Fig. 9 for attenuation can be utilized to assess performance of the MC among different bacteria populations in the microfluidic channels. A biological oscillator development is performed in [27] based on the quorum sensing, where the period of concentration signal is in the order of minutes and even hours, i.e., the frequency of the signal is in the order of 10^{-2} and 10^{-4} s^{-1}. Accordingly, the attenuation of concentration is presented in the Fig. 10 for the low range of frequencies, i.e., up to $k = 100$ radians per meter which is equal to the temporal frequency of $f = 2.02 \cdot 10^{-4}$, $8.83 \cdot 10^{-5}$, $6.76 \cdot 10^{-4}$, and $3.58 \cdot 10^{-4}$ s^{-1} for rectangular, square, elliptic, and circular channels, respectively. It is observed in Fig. 10 that for the frequencies below 10 radians per meter, attenuation in the

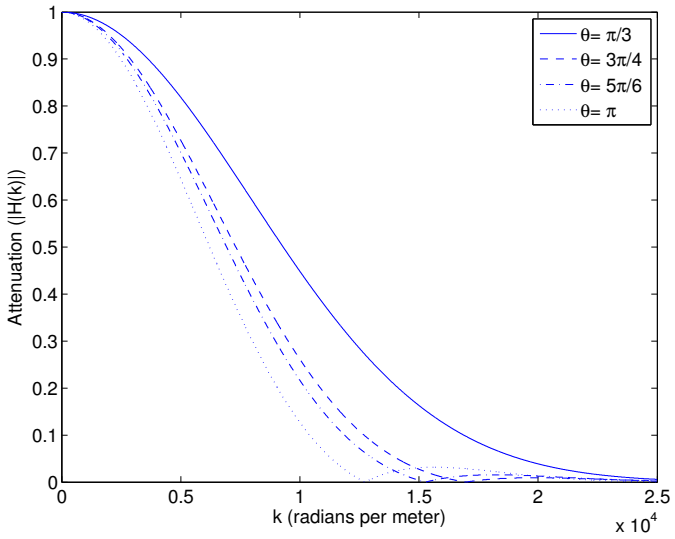

(a)

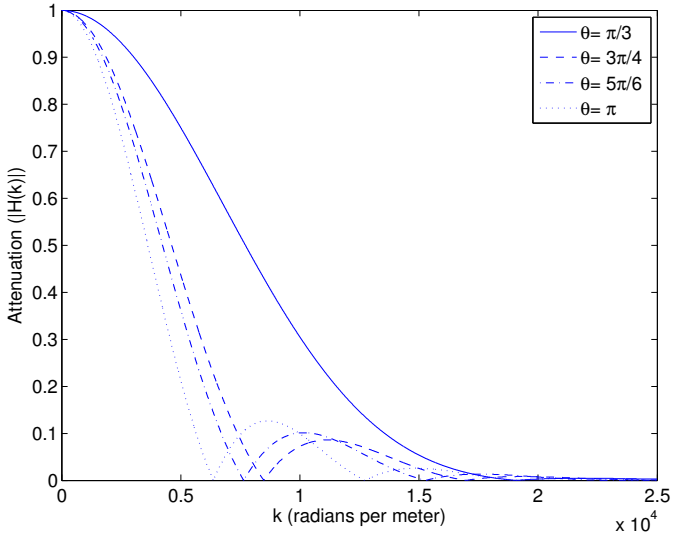

(b)

Figure 11: Attenuation of concentration propagation in turning channel. The magnitude of the transfer functions with different turning angles against wave number k, for radius difference of 50 and 100μm in (a) and (b), respectively.

microfluidic channels becomes negligible.

2.6.1.2 Turning Channel

The turning channel results for rectangular channels are presented in Fig. 11. The channel height h is taken to be 10μm, width w is taken as 50μm, and channel length is 5mm. The

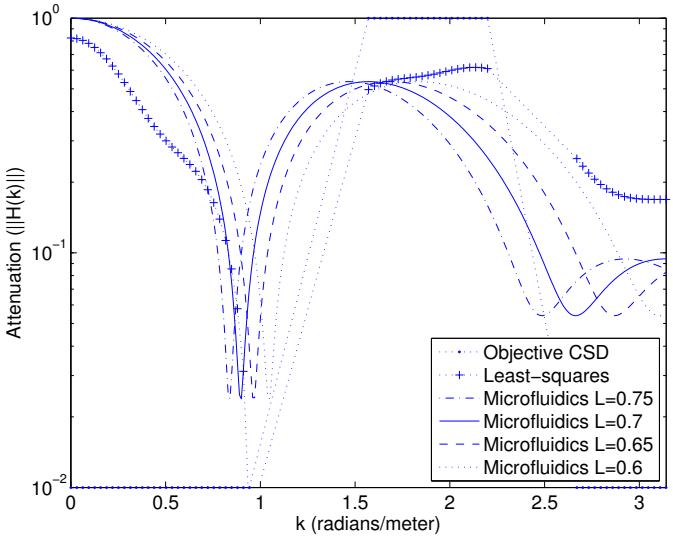

(a)

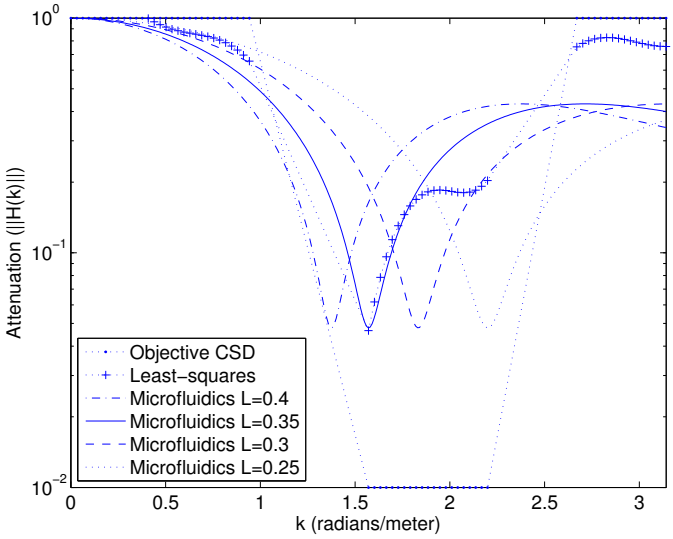

(b)

Figure 12: The frequency response of devised band-pass (a) and band-stop (b) filters.

inner and outer radius differences of $r_\Delta = 50$ and 100μm are used. The turning angle θ is selected as $\pi/3$, $3\pi/4$, $5\pi/6$, and π.

As the turning angle increases from $\pi/3$ to π, achievable frequencies in the turning channel decreases. When the inner and outer radius of turn r_Δ is increased from 50 to 100μm, achievable frequencies decrease for the same channel length in Fig. 11(a) and (b), respectively. Furthermore, the achievable frequencies in the channels is adversely effected

by increasing turning angle, and this effect is further amplified for higher r_Δ.

The frequency response becomes 0 when the wave number k is a positive integer i multiple of the reciprocal of the difference of the traveled paths by the outermost lamina and the innermost lamina, i.e., $1/(r_\Delta\theta)$, as

$$k = \frac{1}{r_\Delta\theta} i \tag{82}$$

This effect is peculiar to the concentration propagation in turning microfluidic channels, and it is due to the addition of phase shifted laminas that cancel out the frequency components given by (82) at the output signal. From the mathematical point of view, the turning channel performs integration of the input signal, and since integration of a sinusoidal signal over a complete period, or multiple complete periods would yield 0, frequency components matching this definition vanish, which are characterized in (82).

2.6.2 Microfluidic FIR Filtering

Here, we present two example designs of microfluidic channels for FIR filtering in FMC. The FIR filter structure is illustrated in Fig. 8. The value of N is set to 10. Pressure drop across channels is set to $\Delta P = 100$Pa. The rectangular channels are used for design. The height of channels is selected as $h = 5\mu$m. The width w of channels is determined according to desired aspect ratio based on the filter constraints. The difference of inner and outer radius at turn is taken as $r_\Delta = 5\mu$m. In each stop and pass band, the frequency is sampled with 0.01 spacing. Magnitude in pass bands is set to 1, and suppression amount in stop bands is set to 10^{-2}. After least-squares optimization of filter coefficients α_n, only positive coefficients are used for channel design. Branches of filter with non-positive coefficient are removed, i.e., α_n is set to 0 for those channels. For aspect ratio design, k in (76) is set to π. Results for band-pass and band-stop filtering are presented in Fig. 12.

The band-pass filter has one pass band, i.e., $0.5\pi - 0.7\pi$, and two stop bands, i.e., $0 - 0.3\pi$ and $0.85\pi - \pi$. The objective frequency response of the band-pass filter and its least-squares approximation are presented in Fig. 12(a). For band-pass filtering, the effect of scaling factor L is studied for $L = 0.75$, 0.7, 0.65, and 0.5. The band-stop filter has one stop band, i.e., $0.5\pi - 0.7\pi$, and two pass bands, i.e., $0 - 0.3\pi$ and $0.85\pi - \pi$. The

objective frequency response of the band-stop filter and its least-squares approximation are presented in Fig. 12(b). For band-stop filtering, the effect of scaling factor L is studied for $L = 0.4$, 0.35, 0.3, and 0.25. Transfer function of the devised microfluidic FIR filter can be fine-tuned to a desired pass and stop bands via adjusting L appropriately. Magnitude of the frequencies in the received CSD can be controlled, and the unwanted frequencies can be suppressed by placing the devised microfluidic FIR filter between the transmitter and the receiver patches, such as a biological oscillator based on bacteria population [27].

2.7 Highlights

This chapter provides a comprehensive coverage of the microfluidic channels with fluid flow for molecular communication systems. An analytical study of the propagation of the molecules is performed incorporating the physical system parameters.

The goal of the propagation modeling is to determine the distortion effects caused on the molecular signal with respect to the distance, fluid flow parameters (pressure drop, flow velocity, microfluidic channel geometry, fluid type), and type of the molecule (diffusion constant). Even though the emphasis of the chapter is on channel modeling and design, necessary fluid flow fundamentals are also included, since the molecules are carried by fluid flow in the microfluidic channel. Linear systems theory is applied to physical laws of mass transport. Propagation models for the basic microfluidic channel shapes (straight and turning) and cross-sections (rectangular, square, elliptical, circular) are developed incorporating the characteristics of the fluid flow and mass transport in the microfluidic channels.

A linear channel model can be solved directly, and the methodologies developed to assess performance of linear communication systems can also be applicable for molecular communication over microfluidic channels, e.g., detection and estimation theory and information theory for linear communication channels. The noise effects on the molecular propagation over microfluidic channels can affect the performance of a molecular communication system, which will be the subject of the next chapter.

Time-varying molecular signals are common in biology. The time scales for many of these signals range from a fraction of a second to several hours, e.g., protein activation

and signaling, paracrine and endocrine cell-cell communication, inflammatory response). In the second part of this work, an interconnection configuration of microfluidic channels is proposed to filter out the unwanted fluctuations (differentiate between fast or slow changes) in the transmitted molecular signal.

The developed models of molecular propagation over microfluidic channels are integrated with the frequency selective signal processing techniques. A mathematical framework is developed to design length and cross-section of interconnected microfluidic channels. Two example designs are presented for the filtering of the unwanted fluctuations using interconnected microfluidic channels.

CHAPTER III

END-TO-END PROPAGATION NOISE AND MEMORY ANALYSIS FOR MICROFLUIDIC CHANNELS

In this chapter, a linear end-to-end channel model is developed capturing the effects of the diffusion and the junction transition at the chambers as well as the microfluidic channel shapes and the fluid flow. The spectral density of the propagation noise is studied and the flat frequency bands are identified for the chambers and the microfluidic channel. The Additive White Gaussian Noise (AWGN) model is developed based on the chamber, the microfluidic channel, and the fluid flow parameters for the end-to-end propagation noise. Additionally, the molecular memory due to inter-diffusion among transmitted molecular signals is modeled. This work was first presented in [2] In Section 3.2, we present a review of related work on noise analysis. We present the propagation model for FMC in Section 3.3. The building blocks of noises in FMC are formulated, and noise spectrum is investigated in Section 3.4. In Section 3.5, molecular memory analysis is presented. Numeric results are presented in Section 3.6.

3.1 Motivation

The analysis of the noise effects for undergoing mass transport mechanisms at the chambers and the microfluidic channel is essential to facilitate development of efficient and practical MC techniques. So far, the propagation modeling and the chemical noise analysis for transmitter and receiver for MC have been a research focus in recent years[7],[13],[11]. The noise effects on the diffusion-based concentration signal propagation in a free space MC system are studied in [10], under the assumption that the molecules propagate from the transmitter to the receiver solely via diffusion. Furthermore, the utilization of the microfluidic channels with fluid flow for FMC is investigated in [1]. While the microfluidic channels with fluid flow enhances the propagation of concentration signal, the FMC paradigm necessitates a new propagation noise notion. This new notion should address the noise effects on the received

signal: 1) transition from/to molecular transport by diffusion in the transmitter/receiver chamber to/from molecular transport by flow in the microfluidic channel; and 2) the random diffusion of molecules inside the chambers and microfluidic channel. Additionally, the investigation of the molecular memory effect due to self-interference created by diffusion of molecules between the transmitted molecular signals is vital.

Our work is motivated by the fact that an efficient FMC system can be devised when the noise and memory effects are understood and predicted by using the developed analytic framework. The notion of controlling the noise and memory effects for efficient FMC via design of chambers and microfluidic channels distinguishes our work from other existing noise analyses that solely focus on identification of noise sources and developing models on top of them [10, 11]. To the best of our knowledge, the noise and memory effects in MC have not been studied from this perspective before.

In this work, first, the propagation model presented in [1] is extended, and a linear end-to-end model incorporating the propagation through the chambers is proposed. Then, the building blocks of the propagation noise is developed based on the autocorrelation function of the molecular signal under the effects of the transition from chamber to microfluidic channel, and vice versa, at junctions, and the diffusion at the chambers and microfluidic channel. Spectral densities of the propagation noise for the transmitter chamber, the microfluidic channel, and the receiver chamber are formulated. Frequency ranges at which spectral density of noise is flat-band are investigated based on the chamber, microfluidic channel, and flow parameters. An Additive White Gaussian Noise (AWGN) model is proposed for FMC in accordance with the flat-band frequency range in the spectral density of the end-to-end propagation noise. Furthermore, the memory due to the diffusion of transmitted molecular signal is analyzed. The statistical properties of the received memory component is studied based on the transmission, the transmitter/receiver chamber, the microfluidic channel, and the fluid flow parameters. Moreover, the effect of molecular memory on end-to-end propagation noise is revealed. Some of the salient features of this study are listed as follows:

- **An Analysis of the Propagation Noise**: Building blocks for the spectral density

of the propagation noise are defined. The end-to-end propagation noise is obtained based on the spectral density of noise at the transmitter chamber, the microfluidic channel, and the receiver chamber. AWGN model for the FMC paradigm is developed.

- **A Linear Molecular Memory Model**: The memory effect due to inter-diffusion of the previously transmitted molecules signals inside microfluidic channel and chambers is analyzed. The memory level is characterized based on the transmission frequency and the distance. The amplitude and the variance of the memory component in the received signal is derived based on the FMC system parameters. Furthermore, the effect of memory on molecular noise is studied, and the end-to-end propagation noise is extended to include this effect.

These are the truly novel aspects of our work and are the main contribution of the proposed analysis of the propagation noise and the memory for MC over microfluidic channels.

3.2 Related Work

The molecular transport over microfluidic channels is investigated in depth in many papers in the last decade [29, 30, 31, 32, 33, 34, 35] where the microfluidic device aspects are explored in depth for the concentration propagation via diffusion and flow, i.e., convection. These contributions aim to find the optimum device parameters to shape the input concentration through the microfluidic channels. More recently, the generation of the higher harmonics of the input concentration wave is investigated based on the microfluidic channel parameters and the interconnection of microfluidic channels [36]. However, the utilization of concentration as a signal for communication between a transmitter and receiver pair is not considered. As a consequence, none of the above studies investigate the noise or memory effects on the concentration signal in microfluidic channels to empower the FMC systems.

On the other hand, there was an extensive research effort on propagation modeling for MC in recent years [7, 1, 37]. For example, solutions have been proposed independent from noise and memory effects for solely diffusion-based free space concentration propagation [7]. Although the investigation of molecular signaling based on the diffusion and convection mechanisms is extremely important, the research on the noise and memory effects is vital

to design efficient yet practical FMC systems. In [10], the molecular noise is studied for a diffusion-based MC system. However, the effects of fluid flow, the chamber, and the microfluidic channel parameters on molecular noise have not been investigated so far. In [11], the noise analysis is performed on the receiver side neglecting molecular noise effects and assuming a specific chemical receiver architecture based on receptor-ligand kinetics. Additionally, MC using individual molecules is studied based on simulation experiments without analytic formulation under ideal transmitter and diffusion-based propagation assumptions [38, 39].

In contrast, in our work we present the propagation noise and memory effects for an FMC system, where the transmitter and the receiver chambers are connected via the microfluidic channel with the fluid flow. The microfluidic channel configurations that yield flat-band noise spectral density are investigated, and the design principles for physical parameters of the MC system to have a valid linear MC model are highlighted.

3.3 End-to-end Molecular Propagation in FMC

In the following discussions, we formally define the physical model of the molecular communication over microfluidic channels. Before proceeding to the analysis of the propagation noise and the memory effects on the received concentration signal, we introduce the notion of the transmitter and the receiver chambers, and develop a linear end-to-end model for the propagation of the released molecules from the transmitter in the transmitter chamber to the receiver in the receiver chamber. We also incorporate the delays, and the transfer functions for the transmitter and the receiver chambers into the developed end-to-end model, and set the stage for the noise and memory analysis by defining the noise and the memory effects on the concentration signal.

3.3.1 Physical Model

Consider the typical MC applications involving the sensing of the chemical signals by the transmitter, and communication of event features with the receiver. We assume that the molecular transmitter and receiver are placed in transmitter and receiver chambers, respectively, which are connected via a microfluidic channel with fluid flow as shown in Fig.1.

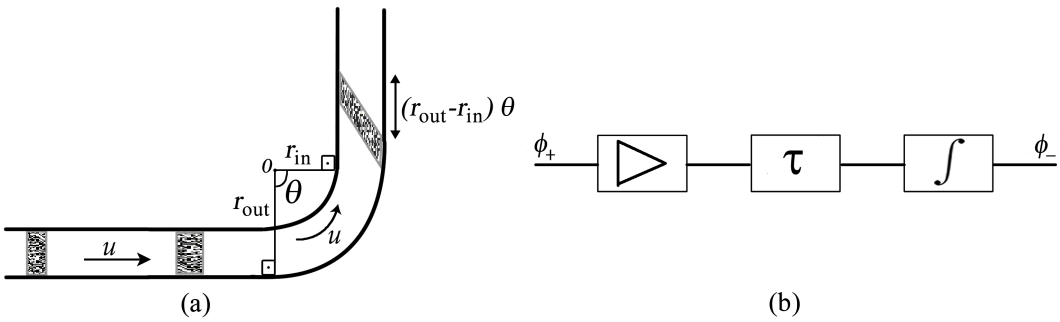

Figure 13: Molecular propagation inside the turning microfluidic channel with angle θ (a) and block diagram representation (b).

The main rationale behind such a flow-induced molecular communication notion is that the propagation of the input concentration signal ϕ_+ generated by the transmitter is enhanced by the fluid flow, which alleviates dispersion of the molecules, i.e., path-loss, and propagation time, i.e., the delay τ, of the received concentration signal ϕ_-. The transmitter and the receiver chambers contain the application specific molecular systems such as a bacteria population [9]. The transmitter generates a concentration signal to communicate the features of the sensed chemical event with the receiver. Here, our focus is on the molecular transport, i.e., the propagation, the mechanisms, hence, the specifics of such a concentration generation process based on chemical kinetics are application dependent and beyond the scope of our work.

In fact, the impulse response, the delay, and the transfer function for molecular propagation in microfluidic channels are derived as functions of the channel length l_{ch}, height a_{ch}, width b_{ch}, turning angle θ, and pressure drop across the channel Δp in [1]. The fluid flow in the microfluidic channel is taken to be laminar, steady, unidirectional, and driven by the pressure drop across the microfluidic channel [16]. The area-averaged flow velocity u for a rectangular cross-section microfluidic channel is given by [15]

$$u = \frac{a_{\text{ch}}^2}{12\mu l_{\text{ch}}} \left(1 - 0.63\frac{a_{\text{ch}}}{b_{\text{ch}}}\right) \Delta p \tag{83}$$

where μ is the viscosity of the fluid. We also assume that due to very short distance in the order of $\sim \mu m$ at transmitter and receiver chambers, propagation velocity by diffusion at chambers is comparable to propagation via flow in microfluidic channel. One-dimensional

solution of the convection-diffusion equation is used to analyze molecular transport via flow in the microfluidic channels [29],[30],[31],[32],[33]. The concentration propagation in the microfluidic channel is illustrated in Fig. 13(a). In the turning channels, the inner and the outer radius of the microfluidic channel, i.e., r_{in} and r_{out}, are different, which causes different laminas to travel different lengths. The cross-section of the microfluidic channel is invariant, and hence, the difference $r_{\text{out}} - r_{\text{in}}$ is equal to a_{ch}. The impulse response of the turning channel, i.e., $\theta > 0$, is given by [1]

$$h_{\text{ch}}(l) = \frac{1}{a_{\text{ch}}\theta} \int_0^{a_{\text{ch}}\theta} \frac{1}{\sqrt{4\pi D\tau_{\text{ch}}}} e^{-\frac{(l-u\tau_{\text{ch}}+x')^2}{4D\tau_{\text{ch}}}} \mathrm{d}x' \tag{84}$$

where the height a_{ch}, and length l_{ch} parameters are illustrated in Fig. 14(a), τ_{ch} is given by $\tau_{\text{ch}} = (l_{\text{ch}} + a_{\text{ch}}\theta)/u$, which is the average delay based on the symmetry around central lamina in the turning channel, and D is the effective diffusion coefficient adjusted according to the Taylor dispersion in rectangular channels based on the intrinsic molecular diffusion coefficient D_0 as [51]

$$D = \left(1 + \frac{8.5u^2 a_{\text{ch}}^2 b_{\text{ch}}^2}{210 D_0^2 (a_{\text{ch}}^2 + 2.4 a_{\text{ch}} b_{\text{ch}} + b_{\text{ch}}^2)}\right) D_0 \tag{85}$$

The turning microfluidic channel depicted in Fig. 13(a) can be seen as an integrator due to its impulse response, which is also a low-pass filter. The impulse response of a straight microfluidic channel, i.e., $\theta = 0$, is given by

$$\begin{aligned} h_{\text{ch}}^{\text{str}}(l) &= \lim_{\theta \to 0} \frac{1}{a_{\text{ch}}\theta} \int_0^{a_{\text{ch}}\theta} \frac{1}{\sqrt{4\pi D\tau_{\text{ch}}}} e^{-\frac{(l-u\tau_{\text{ch}}+x')^2}{4D\tau_{\text{ch}}}} \mathrm{d}x' \\ &= \frac{1}{\sqrt{4\pi D\tau_{\text{ch}}}} e^{-\frac{(l-u\tau_{\text{ch}})^2}{4D\tau_{\text{ch}}}} \end{aligned} \tag{86}$$

Furthermore, the transfer function of the turning microfluidic channel is found by taking the Fourier Transform of (84) and expressed using normalized sinc function as

$$H_{\text{ch}}(k) = e^{-(k^2 D + jku)\tau_{\text{ch}}} \text{sinc}\left(\frac{a_{\text{ch}}\theta}{2\pi} k\right) e^{-jka_{\text{ch}}\theta/2} \tag{87}$$

where k is the angular spatial frequency, i.e., wave number. The transfer function $H_{\text{ch}}(k)$ can be simplified for a straight channel using $\theta = 0$ as

$$H_{\text{ch}}^{\text{str}}(k) = e^{-(k^2 D + jku)\tau_{\text{ch}}} \tag{88}$$

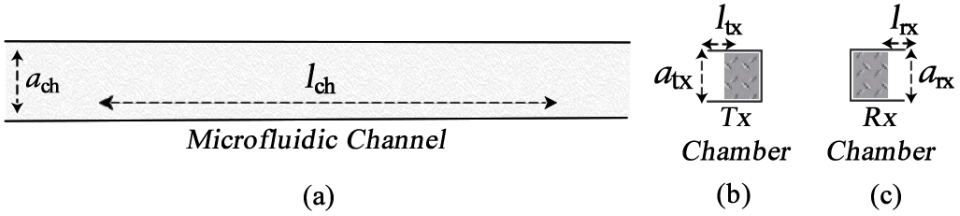

Figure 14: The illustration of length l_{ch}, l_{tx}, and l_{rx} parameters, and height a_{ch}, a_{tx}, and a_{rx} parameters for the microfluidic channel (a), the transmitter chamber (b), and the receiver chamber (c), respectively.

Overall, the molecular propagation inside microfluidic channel can be represented using block diagrams via a series connection of attenuator, delay, and integrator elements as depicted in Fig. 13(b). Next, we model the concentration propagation in the chambers, and the effect of transition at the junctions to/from the microfluidic channel from the transmitter chamber and to the receiver chamber, respectively.

3.3.2 Impact of the Chambers on the Molecular Propagation

The received concentration signal can be obtained via convolution of the input signal with the transmitter, the microfluidic channel, and the receiver impulse responses. Although, the concentration propagation in the microfluidic channel is investigated in [1], the impulse responses, the transfer functions, and the delays of the transmitter and the receiver chambers are yet to be explored. Here, we provide a model including molecular propagation in chambers as well as from/to chambers to/from microfluidic channel at the junctions.

3.3.2.1 Transmitter Chamber

To model the concentration propagation in the transmitter chamber, the solution of the diffusion equation for a point source placed in the chamber, i.e., impulse response, is used. The diffusion equation is defined as [15]

$$\frac{\partial \phi}{\partial \tau} = D_0 \frac{\partial^2 \phi}{\partial l^2} \tag{89}$$

which relates the variation of concentration in time domain to variation of concentration in space domain. The solution of the diffusion equation for a point source input, i.e.,

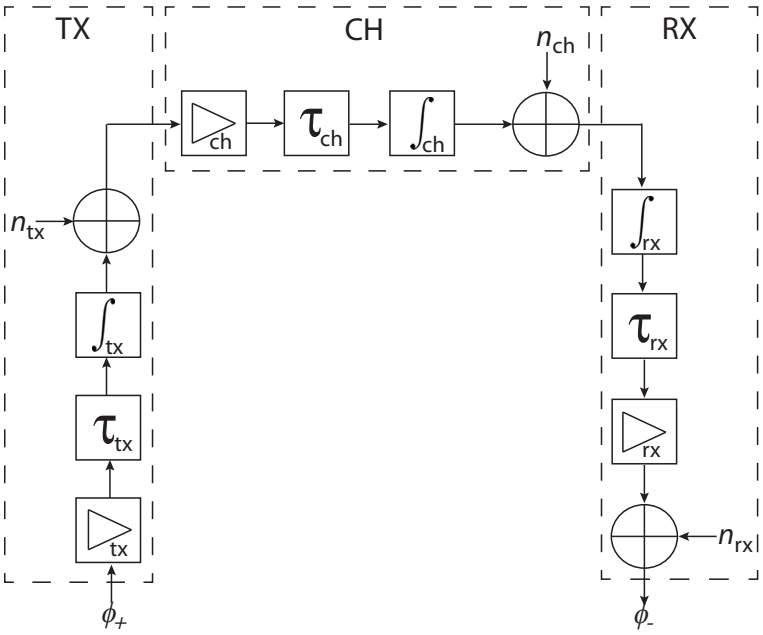

Figure 15: Block diagram representation of linear end-to-end signal model.

$\phi_+(l) = \delta(l)$; where δ is the Dirac delta function, is given by

$$h'_{\text{tx}}(l) = \frac{1}{\sqrt{4\pi D_0 \tau_{\text{tx}}}} e^{-\frac{l^2}{4D_0\tau_{\text{tx}}}} \tag{90}$$

where τ_{tx} is the delay at the transmitter chamber, which is calculated based on the travel time of peak level of concentration, i.e., $\max_{\tau_{\text{tx}}} ||\phi||$ via setting

$$\left.\frac{\partial h'_{\text{tx}}}{\partial \tau_{\text{tx}}}\right|_{l=l_{\text{tx}}} = 0, \tag{91}$$

which gives

$$\frac{l_{\text{tx}}^2 - 2D_0\tau_{\text{tx}}}{8\sqrt{\pi}(D_0\tau_{\text{tx}})^{5/2}} D_0 e^{-\frac{l_{\text{tx}}^2}{4D_0\tau_{\text{tx}}}} = 0 \tag{92}$$

from which τ_{tx} is found as

$$\tau_{\text{tx}} = \frac{l_{\text{tx}}}{2D_0} \tag{93}$$

Due to the finite size height a_{tx} of the transmitter chamber, which is illustrated in Fig. 14(b), the transmitted concentration signal has a pulse width as large as the chamber height a_{tx} at the junction between the transmitter chamber and the microfluidic channel, where the center of the transmitter junction is taken as the origin of the transmitter coordinate axis.

The impulse response of a such behavior, i.e., the junction impulse response, is captured by a scaled rect function to match the chamber height as

$$h_{\text{tx}}^{\text{jct}}(l) = \frac{1}{a_{\text{tx}}}\text{rect}(\frac{1}{a_{\text{tx}}}l - \frac{1}{2}) \tag{94}$$

where the signal is shifted by half chamber height $a_{\text{tx}}/2$ to keep system causality, and $\text{rect}(l)$ is

$$\text{rect}(l) = \begin{cases} 1, & |l| \leq 1/2 \\ 0, & |l| > 1/2 \end{cases}$$

The delay due to shifting of the signal, i.e., $a_{\text{tx}}/(2u)$, is incorporated into microfluidic channel delay in Section 3.3.3.

The overall impulse response of transmitter chamber is formulated as

$$\begin{aligned} h_{\text{tx}}(l) =& (h_{\text{tx}}^{\text{jct}} * h'_{\text{tx}})(l) \\ =& \frac{1}{a_{\text{tx}}} \int_0^{a_{\text{tx}}} \frac{1}{\sqrt{4\pi D\tau_{\text{tx}}}} e^{-\frac{(l-x)^2}{4D\tau_{\text{tx}}}} \,\text{d}x \end{aligned} \tag{95}$$

where τ_{tx} is as given in (93). For a transmitter chamber with a height of $a_{\text{tx}} = 0$, the impulse response of the transmitter chamber reduces to (90). The transfer function for transmitter chamber H_{tx} is found by taking Fourier Transform of the impulse response, i.e., $\mathcal{F}\{h_{\text{tx}}\}$, and using normalized sinc function as

$$H_{\text{tx}}(k) = e^{-k^2 D\tau_{\text{tx}}}\text{sinc}(\frac{a_{\text{tx}}}{2\pi}k)e^{-jka_{\text{tx}}/2} \tag{96}$$

3.3.2.2 Receiver Chamber

Similar to the transmitter chamber, for the concentration propagation in the receiver chamber, we also utilize the solution of the diffusion equation (89) for a point source according to the receiver chamber parameters, i..e, the receiver chamber length l_{rx}, and the receiver chamber height a_{rx}. The receiver chamber performs as an integrator during the transition of concentration from the microfluidic channel to the chamber, whose behavior can be captured by an auxiliary rect function similar to transmitter side (94), where the center of the receiver junction is taken as the origin of the receiver coordinate axis, and hence, the concentration signal is shifted by half chamber height $a_{\text{rx}}/2$ to achieve causality, as

$$h_{\text{rx}}^{\text{jct}}(l) = \frac{1}{a_{\text{rx}}}\text{rect}(\frac{1}{a_{\text{rx}}}l - \frac{1}{2}) \tag{97}$$

The delay due to shifting of the signal, i.e., $a_{\text{rx}}/(2u)$, is incorporated into the microfluidic channel delay in Section 3.3.3. Using the solution of the diffusion equation at the transmitter chamber for a point source in (90), the impulse response for the concentration propagation in the receiver chamber is obtained as

$$h'_{\text{rx}}(l) = \frac{1}{\sqrt{4\pi D_0 \tau_{\text{rx}}}} e^{-\frac{l^2}{4D_0\tau_{\text{rx}}}} \tag{98}$$

The impulse response of the receiver chamber incorporating the effect of the receiver junction is formulated as

$$\begin{aligned} h_{\text{rx}}(l) =& (h'_{\text{rx}} * h^{\text{jct}}_{\text{rx}})(l) \\ =& \frac{1}{a_{\text{rx}}} \int_0^{a_{\text{rx}}} \frac{1}{\sqrt{4\pi D_0 \tau_{\text{rx}}}} e^{-\frac{(l-x)^2}{4D\tau_{\text{rx}}}} \, \mathrm{d}x \end{aligned} \tag{99}$$

where the delay of the receiver chamber τ_{rx} can be obtained by solving (92) for the receiver chamber as

$$\tau_{\text{rx}} = \frac{l_{\text{rx}}}{2D_0} \tag{100}$$

Similar to the transmitter chamber case, it is observed that for a receiver chamber with a height of $a_{\text{rx}} = 0$, the impulse response of the transmitter chamber reduces to (98). Finally, the transfer function of the receiver chamber is given by $\mathcal{F}\{h_{\text{rx}}\}$ as

$$H_{\text{rx}}(k) = e^{-(k^2 D + jku)\tau_{\text{rx}}} \text{sinc}(\frac{a_{\text{rx}}}{2\pi} k) e^{-jka_{\text{rx}}/2} \tag{101}$$

Overall, the impulse responses, the delays, and the transfer functions are provided for the chambers and the microfluidic channel. Next, we propose the linear end-to-end model for FMC and identify the noise and memory effects on the end-to-end signal propagation.

3.3.3 Linear End-to-end Signal Model

The transmitted molecular signal ϕ_+ can be represented by

$$\phi_+(l) = m(l) e^{j2k_0 l} \tag{102}$$

where k_0 is the carrier frequency of the molecular oscillators placed in the transmitter and receiver chambers, $m(l)$ is the message signal, which is a wide-sense stationary process

subject to variance constraint ψ^2 as

$$\mathrm{E}[m^2(l)] = \psi^2 \tag{103}$$

For signal reception, we consider the propagation of the leading edge of the molecular signal at carrier frequency k_0. Therefore, for MC channel response, gain of the system is calculated for a delay of τ_{tx}, τ_{ch}, and τ_{rx} in transmitter chamber, microfluidic channel, and receiver chamber, respectively. The signal gain at the transmission frequency k_0 and delay τ_{tx} for the transmitter chamber α_{tx} is found using Wiener-Khinchin theorem as

$$\begin{aligned}\alpha_{\mathrm{tx}} =& |H_{\mathrm{tx}}(k_0)| \\ =& \exp(-k_0^2 D_0 \tau_{\mathrm{tx}}) \mathrm{sinc}(\frac{a_{\mathrm{tx}}}{2\pi} k_0)\end{aligned} \tag{104}$$

For the microfluidic channel, the signal gain at the transmission frequency k_0 and delay τ_{ch}, is found as

$$\begin{aligned}\alpha_{\mathrm{ch}} =& |H_{\mathrm{ch}}(k_0)| \\ =& \exp(-k_0^2 D \tau_{\mathrm{ch}}) \mathrm{sinc}(\frac{a_{\mathrm{ch}}\theta}{2\pi} k_0)\end{aligned} \tag{105}$$

For the receiver chamber, the signal gain at the transmission frequency k_0 and delay τ_{rx} is found as

$$\begin{aligned}\alpha_{\mathrm{rx}} =& |H_{\mathrm{rx}}(k_0)| \\ =& \exp(-k_0^2 D_0 \tau_{\mathrm{rx}}) \mathrm{sinc}(\frac{a_{\mathrm{rx}}}{2\pi} k_0)\end{aligned} \tag{106}$$

Combining the attenuation at the chambers and the microfluidic channel, the linear end-to-end model of the FMC is illustrated in Fig. 15. Using the developed system-theoretic model, we incorporate the noise and the memory effects into a linear end-to-end signal model. The linear received signal model for the molecular receiver is formulated as

$$\begin{aligned}\chi =& \alpha_{\mathrm{rx}} \left(\alpha_{\mathrm{ch}} \left(\alpha_{\mathrm{tx}} \varphi + n_{\mathrm{tx}}\right) + n_{\mathrm{ch}}\right) + n_{\mathrm{rx}} \\ =& \alpha_{\mathrm{e2e}} \varphi + n_{\mathrm{e2e}}\end{aligned} \tag{107}$$

where φ and χ are the magnitudes of the transmitted and received signals, i.e., $\varphi = |\Phi_+(k_0)|$ and $\chi = |\Phi_-(k_0)|$, respectively; α_{e2e} is the end-to-end signal gain given by $\alpha_{\mathrm{tx}}\alpha_{\mathrm{ch}}\alpha_{\mathrm{rx}}$; n_{tx},

n_{ch}, and n_{rx} are the the noise effects at the output of the transmitter chamber, microfluidic channel, and receiver chamber; n_{e2e} is the end-to-end noise term given by

$$n_{\text{e2e}} = \alpha_{\text{rx}}\alpha_{\text{ch}}n_{\text{tx}} + \alpha_{\text{rx}}n_{\text{ch}} + n_{\text{rx}} \tag{108}$$

Incorporating the transmitter and the receiver chamber delays, the end-to-end delay is formulated as

$$\tau_{\text{e2e}} = \tau_{\text{rx}} + \frac{a_{\text{rx}}}{2u} + \tau_{\text{ch}} + \frac{a_{\text{tx}}}{2u} + \tau_{\text{tx}} \tag{109}$$

where $a_{\text{tx}}/(2u)$ and $a_{\text{rx}}/(2u)$ are the delays added to provide causality for the transmitter and the receiver chamber impulse responses. We add these delays into τ_{ch} to incorporate into travel time inside microfluidic channel, and define the extended microfluidic channel delay τ^*_{ch} as

$$\tau^*_{\text{ch}} = \tau_{\text{ch}} + \frac{a_{\text{tx}} + a_{\text{rx}}}{2u} \tag{110}$$

The memory effects due to diffusion of previously transmitted molecular signals inside microfluidic channel and chambers will be elaborated and incorporated into linear end-to-end model in Section 3.5. Next, we derive the building blocks of the propagation noise, and investigate the spectral density of the end-to-end propagation noise on the received concentration.

3.4 Propagation Noise Analysis

In this section, for the linear signal model in (107), the noise effects on the received concentration signal are characterized using the autocorrelation of the corresponding impulse responses of the transmitter chamber (96), the microfluidic channel (84), and the receiver chamber (99). To this end, first, building blocks of noise autocorrelations are defined based on the propagation of the concentration signal by diffusion and at the junction transition, which are similar to thermal and shot noise effects, respectively, in electronic circuits. Then, autocorrelation of the propagation noise at the chambers and the microfluidic channel are formulated. Finally, spectral density of the end-to-end propagation noise is obtained, and statistical properties are studied.

3.4.1 Building Blocks of the Molecular Noise

The molecules forming a concentration signal are under continuous displacement due to the Brownian motion. Therefore, discrete and independent motion of molecules results in a noncontinuous concentration signal, and the molecules passing at the junction between the microfluidic channel and the chambers vary in an unpredictable way. Diffusion noise defined as the noise effect due to Brownian motion of the molecules during diffusion-based and convection-based transport of molecules. Junction transition noise is observed when the molecules are transported by the flow in the only one direction. The molecular propagation at the junctions between the chambers and the microfluidic channel are exposed to such noise effects. In the following subsections, to characterize the propagation noise effects, autocorrelation functions of the diffusion noise and the junction transition noise, i.e., R_{diff} and R_{jct}, are formulated as the building blocks of the propagation noise at the chambers and the microfluidic channel.

3.4.1.1 Diffusion Noise Autocorrelation Function

For the diffusion noise, using the given solutions of the diffusion equation for the transmitter and receiver chambers in (90) and (98), respectively, we define the generalized impulse response of the propagation by diffusion as

$$h_{\text{diff}}(l) = \frac{1}{\sqrt{4\pi D_0 \tau_{\text{diff}}}} e^{-\frac{l^2}{4D_0\tau_{\text{diff}}}} \tag{111}$$

where τ_{diff} is the diffusion duration. The autocorrelation of the concentration signal for the diffusion noise is given by

$$R_{\text{diff}}(\xi) = (\phi_-(l) * \phi_-(-l))(\xi) \tag{112}$$

where $\phi_-(l) = (h_{\text{diff}} * \phi_+)(l)$. For an input concentration of $\phi_+(l) = \delta(l)$, the autocorrelation function of the diffusion noise is obtained as

$$\begin{aligned} R_{\text{diff}}(\xi) &= \int_{-\infty}^{\infty} h_{\text{diff}}(l+\xi) h_{\text{diff}}(l) \mathrm{d}l \\ &= \frac{1}{\sqrt{8\pi D_0 \tau_{\text{diff}}}} e^{-\frac{\xi^2}{8D_0\tau_{\text{diff}}}} \end{aligned} \tag{113}$$

Furthermore, spectral density of diffusion noise is given by $\mathcal{F}\{R_{\text{diff}}\}$ as

$$S_{\text{diff}}(k) = e^{-2k^2 D\tau_{\text{diff}}} \tag{114}$$

3.4.1.2 Junction Transition Noise Autocorrelation Function

Based on impulse responses of the transmitter and the receiver junctions, i.e., $h_{\text{jct}}^{\text{tx}}$ and $h_{\text{jct}}^{\text{rx}}$, respectively, a generic impulse response is defined as

$$h_{\text{jct}}(l) = \frac{1}{a_{\text{jct}}}\text{rect}(\frac{1}{a_{\text{jct}}}l) \tag{115}$$

where a_{jct} is the chamber height. Similar to the calculation of the autocorrelation function R_{diff} for diffusion noise in (112), the autocorrelation of junction transition noise R_{jct} is given by

$$R_{\text{jct}}(\xi) = (\phi_-(l) * \phi_-(-l))(\xi) \tag{116}$$

where concentration signal $\phi_-(l) = (h_{\text{jct}} * \phi_+)(l)$. For an input signal of $\phi_+(l) = \delta(l)$, R_{jct} is found as

$$\begin{aligned} R_{\text{jct}}(\xi) =& \int_{-\infty}^{\infty} h_{\text{jct}}(l+\xi)h_{\text{jct}}(l)\text{d}l \\ =& \frac{1}{a_{\text{jct}}^2}\int_{-\infty}^{\infty} \text{rect}(\xi + \frac{1}{a_{\text{jct}}}l)\text{rect}(\frac{1}{a_{\text{jct}}}l)\text{d}l \end{aligned} \tag{117}$$

which is evaluated as

$$R_{\text{jct}}(\xi) = \begin{cases} \frac{1}{a_{\text{jct}}} - \frac{|\xi|}{a_{\text{jct}}^2}, & |\xi| \leq a_{\text{jct}} \\ 0, & \text{otherwise} \end{cases} \tag{118}$$

Furthermore, the spectral density for the junction transition noise is found via Fourier Transform of the autocorrelation function $\mathcal{F}\{R_{\text{jct}}\}$ as

$$\begin{aligned} S_{\text{jct}}(k) =& \text{sinc}^2(\frac{a_{\text{jct}}}{2\pi}k) \\ =& \frac{\sin^2(a_{\text{jct}}k/2)}{a_{\text{jct}}^2 k^2/4} \end{aligned} \tag{119}$$

3.4.2 Autocorrelation Analysis

Here, we formulate the autocorrelation of the propagation noise at the transmitter chamber, the microfluidic channel, and the receiver chamber using the developed building blocks of the propagation noise in the previous subsection.

3.4.2.1 Transmitter Chamber

The noise variance in the transmitter chamber is given by the diffusion of the transmitted concentration as

$$\begin{aligned}\Lambda_{\text{tx}}^2 &= \left(1 - \exp(-2k_0^2 D\tau_{\text{tx}})\right)\psi^2 \\ &\approx \left(1 - \left(-2k_0^2 D_0\tau_{\text{tx}} + 1\right)\right)\psi^2 \\ &= 2k_0^2 D_0\tau_{\text{tx}}\psi^2 \end{aligned} \tag{120}$$

where the Taylor series expansion of $\exp(x) \approx x+1$ for $x \approx 0$ is used. Combining the Fourier Transform of the diffusion and junction transition autocorrelation functions in (114) and (119), respectively, the spectral density of the transmitter chamber noise is obtained as

$$\begin{aligned}S_{\text{tx}}(k) =& \Lambda_{\text{tx}}^2 S_{\text{diff}}^{\text{tx}}(k) S_{\text{jct}}^{\text{tx}}(k) \\ =& 2k_0^2 D_0\tau_{\text{tx}}\psi^2 e^{-2k^2 D\tau_{tx}} \text{sinc}^2(\frac{a_{\text{tx}}}{2\pi}k) \end{aligned} \tag{121}$$

where $S_{\text{diff}}^{\text{tx}}$ and $S_{\text{jct}}^{\text{tx}}$ are the Fourier Transform of the autocorrelation of diffusion and junction transition adjusted to the transmitter chamber parameters.

3.4.2.2 Microfluidic Channel

Diffusion of the concentration signal through microfluidic channel gives the noise variance in the microfluidic channel as

$$\begin{aligned}\Lambda_{\text{ch}}^2 =& \alpha_{\text{tx}}^2 \left(1 - \exp(-2k_0^2 D\tau_{\text{ch}}^*)\text{sinc}^2(\frac{a_{\text{ch}}\theta}{2\pi}k_0)\right)\psi^2 \\ \approx& \alpha_{\text{tx}}^2\psi^2 + \alpha_{\text{tx}}^2 k_0^2 D\tau_{\text{ch}}^* \text{sinc}^2(\frac{a_{\text{ch}}\theta}{2\pi}k_0)\psi^2 \\ & - \alpha_{\text{tx}}^2 \text{sinc}^2(\frac{a_{\text{ch}}\theta}{2\pi}k_0)\psi^2 \end{aligned} \tag{122}$$

where the Taylor series expansion of $\exp(x) \approx x + 1$ for $x \approx 0$ is used. The spectral density of the straight microfluidic channel, i.e., $\theta = 0$, is as

$$S_{\text{ch}}(k) = \Lambda_{\text{ch}}^2 S_{\text{diff}}^{\text{ch}}(k) \tag{123}$$

where $S_{\text{diff}}^{\text{ch}}$ is the Fourier Transform of the autocorrelation of diffusion noise adjusted to microfluidic channel parameters, which is given by

$$S_{\text{diff}}^{\text{ch}}(k) = \alpha_{\text{tx}}^2 2k_0^2 D\tau_{\text{ch}}^*\psi^2 e^{-2k^2 D\tau_{ch}} \tag{124}$$

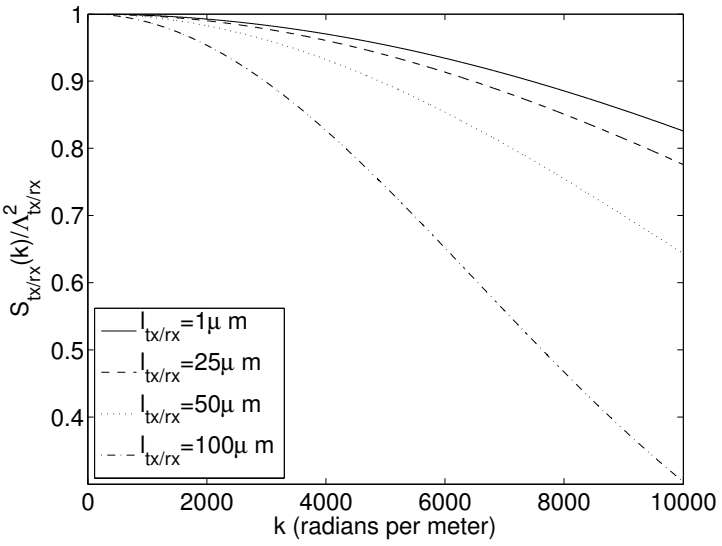

(a)

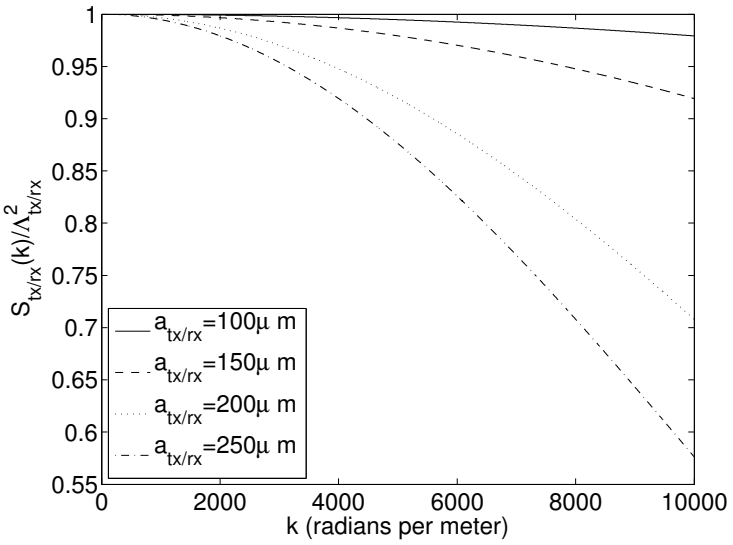

(b)

Figure 16: Transmitter and receiver chamber noise spectral densities for various chamber length $l_{\mathrm{tx/rx}}$ (a) and chamber height $a_{\mathrm{tx/rx}}$ (b) values.

3.4.2.3 Receiver Chamber

Diffusion of the concentration signal in the receiver chamber gives the the receiver chamber noise variance as

$$\begin{aligned}\Lambda^2_{\mathrm{rx}} =& \alpha^2_{\mathrm{tx}}\alpha^2_{\mathrm{ch}}\left(1-\exp(-2k_0^2 D_0\tau_{\mathrm{rx}})\right)\psi^2 \\ \approx& \alpha_{\mathrm{tx}}\alpha_{\mathrm{ch}}2k_0^2 D_0\tau_{\mathrm{rx}}\psi^2 \end{aligned} \tag{125}$$

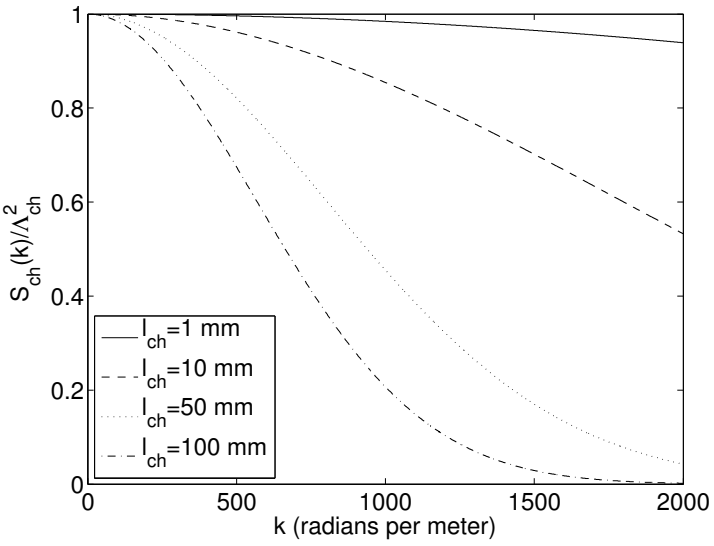

Figure 17: Spectral density of the microfluidic channel noise for various length $l_{\rm ch}$ values.

where the Taylor series expansion of $\exp(x) \approx x+1$ for $x \approx 0$ is used. Combining the Fourier Transform of the diffusion and junction transition noise autocorrelation functions in (114) and (119), respectively, the spectral density of the receiver chamber noise is obtained as

$$\begin{aligned} S_{\rm rx}(k) =& \Lambda_{\rm rx}^2 S_{\rm diff}^{\rm rx}(k) S_{\rm jct}^{\rm rx}(k) \\ =& \alpha_{\rm tx}^2 \alpha_{\rm ch}^2 2k_0^2 D_0 \tau_{\rm rx} \psi^2 e^{-2k^2 D \tau_{rx}} {\rm sinc}^2(\frac{a_{\rm rx}}{2\pi}k) \end{aligned} \tag{126}$$

where $S_{\rm diff}^{\rm rx}$ and $S_{\rm jct}^{\rm rx}$ are the Fourier Transform of the autocorrelation of diffusion and junction transition adjusted to receiver chamber parameters.

3.4.3 The Noise Model for FMC

Here, we investigate the spectral densities of the three propagation noises, i.e., transmitter chamber noise $n_{\rm tx}$, microfluidic channel noise $n_{\rm ch}$, and the receiver chamber noise $n_{\rm rx}$. In Fig. 16(a) and (b), the normalized chamber noise spectral density is depicted for various chamber length $l_{\rm tx/rx}$ and chamber height $a_{\rm tx/rx}$ values, respectively. It is shown that for sufficiently small wave number k, noise CSD can be taken as flat-band for transmitter and receiver chamber noises. Due to flat-band noise spectral density, the amplitude of the propagation noise can be taken as Gaussian distributed for the transmitter and receiver

chambers. For the transmitter chamber noise, probability distribution is given by

$$n_{\text{tx}} \sim \mathcal{N}\left(0, \Lambda_{\text{tx}}^2\right) \tag{127}$$

where Λ_{tx}^2 is the transmitter chamber noise variance given by

$$\Lambda_{\text{tx}}^2 = 2k_0^2 D_0 \tau_{\text{tx}} \psi^2 \tag{128}$$

For the receiver chamber noise, probability distribution is given by

$$n_{\text{rx}} \sim \mathcal{N}\left(0, \Lambda_{\text{rx}}^2\right) \tag{129}$$

where Λ_{rx}^2 is the receiver chamber noise variance given by

$$\Lambda_{\text{rx}}^2 = 2k_0^2 D_0 \tau_{\text{rx}} \alpha_{\text{ch}}^2 \alpha_{\text{tx}}^2 \psi^2 \tag{130}$$

Furthermore, in Fig. 17, it is shown that the spectral density of the noise at microfluidic channel can be taken as a flat-band for sufficiently small k values. Therefore, the amplitude distribution of the microfluidic channel noise can also be taken as Gaussian, i.e.,

$$n_{\text{ch}} \sim \mathcal{N}\left(0, \Lambda_{\text{ch}}^2\right) \tag{131}$$

where Λ_{ch}^2 is the microfluidic channel noise variance and can be approximated for a straight microfluidic channel as

$$\Lambda_{\text{ch}}^2 = 2k_0^2 D \tau_{\text{ch}}^* \alpha_{\text{tx}}^2 \psi^2 \tag{132}$$

Therefore, the end-to-end propagation noise can be approximated as Additive White Gaussian Noise (AWGN) based on the chamber and microfluidic channel parameters. Based on the end-to-end model given in (108), the distribution of the end-to-end propagation noise is obtained as

$$\begin{aligned} n_{\text{e2e}} \sim & \alpha_{\text{rx}} \alpha_{\text{ch}} n_{\text{tx}} + \alpha_{\text{rx}} n_{\text{ch}} + n_{\text{rx}} \\ \sim & \mathcal{N}\left(0, \Lambda_{\text{e2e}}^2\right) \end{aligned} \tag{133}$$

where Λ_{e2e}^2 is the variance of the end-to-end propagation noise and is given by

$$\Lambda_{\text{e2e}}^2 = 2k_0^2 (D_0 \tau_{\text{tx}} \alpha_{\text{ch}} \alpha_{\text{rx}}^2 + \alpha_{\text{tx}}^2 D \tau_{\text{ch}}^* \alpha_{\text{rx}}^2 + \alpha_{\text{tx}}^2 \alpha_{\text{ch}}^2 D_0 \tau_{\text{rx}}) \psi^2 \tag{134}$$

Since the frequency range of the flat-band noise spectral density is much smaller for microfluidic channel noise compared to the chamber noises, we will further investigate the frequency ranges where the end-to-end propagation noise spectral density is flat-band in Section 3.6.2 for various microfluidic channel lengths, turning angles, and pressure drop values. Next, we investigate the memory effects in FMC.

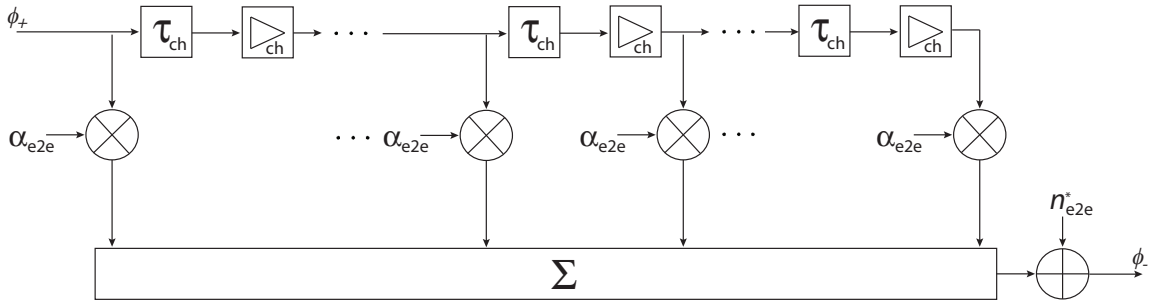

Figure 18: Block diagram representation of the linear memory model.

3.5 Memory Analysis

Memory effect is caused by the self-interference of the molecular signal through the transmitter/receiver chambers and microfluidic channel due to the diffusion of the transmitted signal. In this section, we present a linear model of memory for FMC. Furthermore, we also investigate the effect of memory on the end-to-end propagation noise. Finally, we present the end-to-end signal model with memory.

3.5.1 Linear Memory Model

The transmitted signal diffuses throughout the transmitter camber, microfluidic channel, and receiver chamber, respectively. Therefore, when the transmission wave number is sufficiently large, transmitted signal will be exposed to the self-interference. For transmission wave number k_0, required propagation time for channel memory τ_{mem} is defined equal to period of the transmitted signal as

$$\begin{aligned}\tau_{\text{mem}} =& \frac{1}{f_0} \\ =& \frac{2\pi}{k_0 u}\end{aligned} \tag{135}$$

where identity $ku = 2\pi f$ for molecular signals is used [1]. When propagation time is higher than the τ_{mem}, the received signal becomes exposed to the memory. The linear memory model is given in Fig. 18. Based on the wave number k and the distance, the multiple memory branches may become active. The memory coefficient $\beta_{\text{tx/rx}}$ for transmitter/receiver chambers is defined as

$$\beta_{\text{tx/rx}} = e^{(-k_0 D_0 \frac{2\pi}{u})} \tag{136}$$

and the memory coefficient β_{ch} for microfluidic channel is defined as

$$\beta_{\text{ch}} = e^{(-k_0 D \frac{2\pi}{u})} \tag{137}$$

The memory is composed of three parts, i.e., the transmitter camber, the microfluidic channel, and the receiver chamber, as

$$I = I_{\text{rx}} + I_{\text{ch}} + I_{\text{tx}} \tag{138}$$

For the memory at the chambers, required condition on channel for memory is given by

$$\tau_{\text{mem}} < \tau_{\text{tx/rx}} \tag{139}$$

Accordingly, the memory level, i.e., the number of active branches in the presented model shown in Fig. 18, is given by

$$\eta_{\text{tx/rx}} = \left\lfloor \frac{\tau_{\text{tx/rx}}}{\tau_{\text{mem}}} \right\rfloor \tag{140}$$

For the memory at the microfluidic channel, required condition for memory is given by

$$\tau_{\text{mem}} < \tau_{\text{ch}} \tag{141}$$

Accordingly, the memory level at the microfluidic channel is equal to

$$\eta_{\text{ch}} = \left\lfloor \frac{\tau_{\text{ch}}}{\tau_{\text{mem}}} \right\rfloor \tag{142}$$

In Fig. 19, memory level for chambers and microfluidic channel is presented with respect to the transmission frequency. For numerical results, chamber length $l_{\text{tx/rx}}$ is 1μm, flow velocity is 10^{-4}m/s, and the microfluidic channel length l_{ch} is taken as 50mm. It is observed that memory level $\eta_{\text{tx/rx}}$ is 0 for the whole frequency ranges of interest, meanwhile the

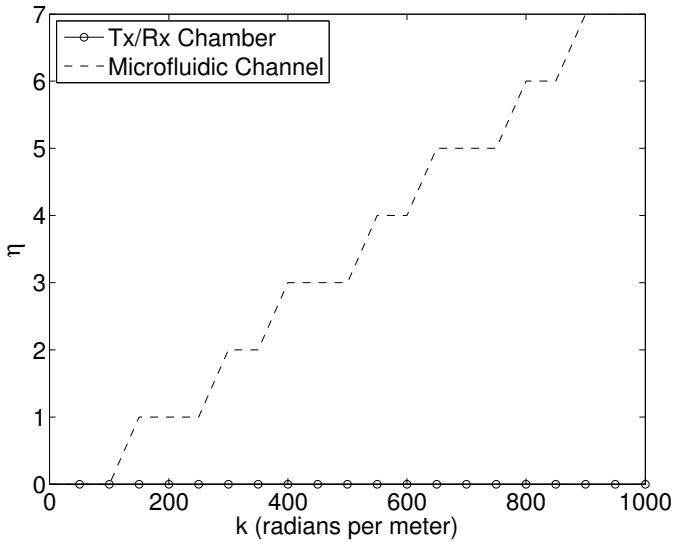

Figure 19: Memory level at transmitter/receiver chambers $\eta_{\text{tx/rx}}$ and microfluidic channels η_{ch} versus the wave number k.

memory level for the microfluidic channel η_{ch} increases with frequency as a step function and enables more memory branches at the microfluidic channel. Therefore, the end-to-end memory magnitude in (138) can be approximated based on the microfluidic channel memory as

$$I \approx I_{\text{ch}} \tag{143}$$

Based on the end-to-end signal model given in (107), magnitude of the memory component in received molecular signal is given by

$$\begin{aligned} I =& \sum_{i=1}^{\eta_{\text{ch}}} \alpha_{\text{rx}} \beta_{\text{ch}}^{i} \alpha_{\text{ch}} \alpha_{\text{tx}} \varphi \\ =& \alpha_{\text{rx}} \alpha_{\text{ch}} \alpha_{\text{tx}} \frac{e^{-k_0 D \frac{\pi}{u}} - e^{-k_0 D \frac{2\pi}{u}(\eta_{\text{ch}}+1)}}{1 - e^{-k_0 D \frac{2\pi}{u}}} \varphi \end{aligned} \tag{144}$$

Furthermore, the variance of the memory component in the received molecular signal is given by

$$\begin{aligned} \mathrm{E}[I^2] =& \sum_{i=1}^{\eta_{\text{ch}}} \alpha_{\text{rx}}^2 \beta_{\text{ch}}^{2i} \alpha_{\text{ch}}^2 \alpha_{\text{tx}}^2 \psi^2 \\ =& \alpha_{\text{rx}} \alpha_{\text{ch}} \alpha_{\text{tx}} \frac{e^{-2k_0 D \frac{2\pi}{u}} - e^{-2k_0 D \frac{2\pi}{u}(\eta_{\text{ch}}+1)}}{1 - e^{-2k_0 D \frac{2\pi}{u}}} \psi^2 \end{aligned} \tag{145}$$

Next, we continue our memory analysis with the effect of memory on the end-to-end molecular propagation noise.

3.5.2 End-to-end Propagation Noise due to Memory

In addition to the memory model presented in the previous subsection, the end-to-end propagation noise variance is further amplified due to the self-interference of the transmitted signal molecules at the transmitter/receiver chambers and the microfluidic channel. Since the memory level at the chambers is shown to be taken as 0 in the previous subsection, to incorporate the effect of memory into the end-to-end propagation noise, we use the definition of the microfluidic channel noise in Section 3.4.2.2. For a τ_{mem} satisfying (141), the noise variance due to memory is found as

$$\begin{aligned}\Lambda^2_{\text{MEM}} =& \sum_{i=1}^{\eta_{\text{ch}}} \alpha^2_{\text{tx}} \left(1 - \alpha^2_{\text{ch}} \beta^{2i}_{\text{ch}}\right) \alpha^2_{\text{rx}} \psi^2 \\ =& \sum_{i=1}^{\eta_{\text{ch}}} \alpha^2_{\text{tx}} \left(1 - e^{-2k_0^2 D(\tau_{\text{ch}} + \frac{1}{f_c} i)}\right) \alpha^2_{\text{rx}} \psi^2 \\ \approx& \alpha^2_{\text{tx}} \alpha^2_{\text{rx}} 2k_0^2 D \left(\eta \tau_{\text{ch}} + \frac{\eta(\eta+1)}{2f_0}\right) \psi^2 \end{aligned} \tag{146}$$

where the first order Taylor series expansion of $\exp(x) \approx x + 1$ for $x \approx 0$ is used.

Furthermore, similar to the microfluidic channel noise spectral density, the spectral density of the propagation noise due to memory is obtained as

$$\begin{aligned} S_{\text{MEM}}(k) =& \Lambda^2_{\text{MEM}} S^{\text{ch}}_{\text{diff}}(k) \\ =& \alpha^2_{\text{tx}} \alpha^2_{\text{rx}} k_0^2 D \left(2\eta \tau_{\text{ch}} + \frac{\eta(\eta+1)}{f_0}\right) \psi^2 e^{-2k^2 D \tau_{ch}} \end{aligned} \tag{147}$$

The noise spectral density with memory, i.e., spectral density of the unified end-to-end propagation noise, can also be taken as flat-band for sufficiently small k. Therefore, the unified end-to-end propagation noise n^*_{e2e} can be taken as Gaussian distributed. Based on the end-to-end model given in (108), the distribution of the unified end-to-end propagation noise is found as

$$n^*_{\text{e2e}} \sim \mathcal{N}\left(0, \Lambda^2_{\text{e2e}} + \Lambda^2_{\text{MEM}}\right) \tag{148}$$

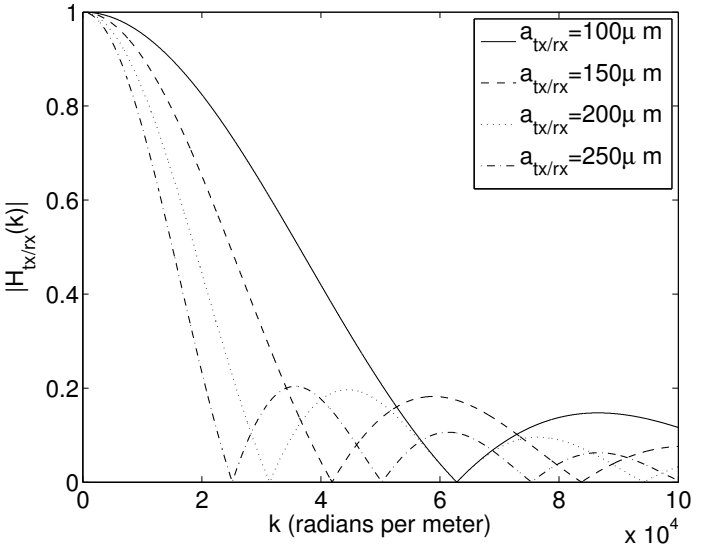

(a)

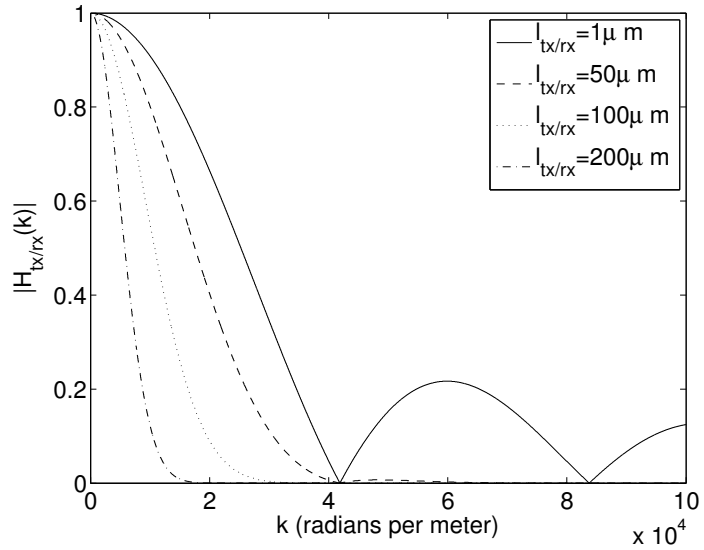

(b)

Figure 20: Chamber attenuation based on chamber height $a_{\text{tx/rx}}$ (a) and chamber length $l_{\text{tx/rx}}$ (b).

3.5.3 End-to-end Signal Model with Memory

The tapped delay-line model of molecular memory is illustrated in Fig. 18. The linear end-to-end model in (107) can be rearranged using (144) and (148) as

$$\begin{aligned}\chi =& \alpha_{\text{rx}}\alpha_{\text{ch}}\alpha_{\text{tx}}\varphi + n^*_{\text{e2e}} + I \\ =& \left(\frac{1-e^{-k_0 D\frac{2\pi}{u}(\eta_{\text{ch}}+1)}}{1-e^{-k_0 D\frac{2\pi}{u}}}\right)\alpha_{\text{rx}}\alpha_{\text{ch}}\alpha_{\text{tx}}\varphi + n^*_{\text{e2e}}\end{aligned} \tag{149}$$

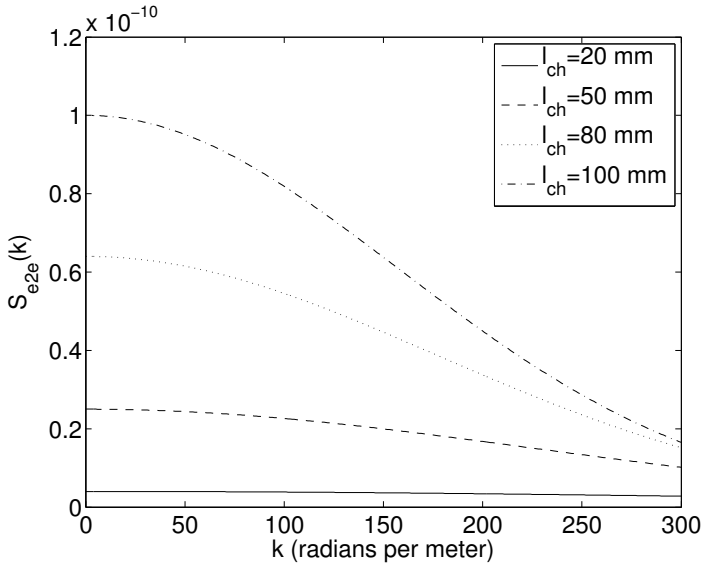

(a)

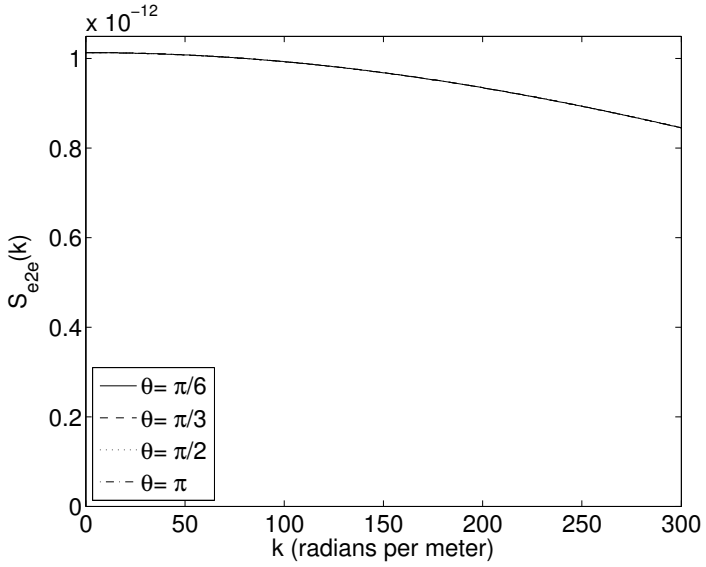

(b)

Figure 21: The end-to-end propagation noise CSD based on length l_{ch} (a) and turning angle θ (b).

Overall, the performed analyses for the end-to-end propagation noise and molecular memory provide an analytical framework to devise communication schemes for molecular communication over the microfluidic channels. Furthermore, the noise and memory models presented here complement the propagation analysis in [1].

3.6 Numerical Results

In this section, obtained analytical results are numerically elaborated. We, first, study the signal propagation at the transmitter and receiver chambers. Specifically, we investigate the effect of the chamber height and length for the transmitter and receiver chambers in Fig. 20(a) and (b). Then, we investigate the CSD of end-to-end propagation noise for microfluidic channel length l_{ch}, turning angle θ, and pressure drop Δp in Fig. 21(a) and (b), and Fig. 22, respecitvely. During numerical evaluations, viscosity μ of the fluid is set to $10^{-3}\text{Pa}\cdot\text{s}$, and diffusion constant D_0 is set to $10\cdot 10^{-10}\text{m}^2/\text{s}$.

3.6.1 Attenuation at the Transmitter and Receiver Chambers

The concentration propagation in chambers is studied in two parts, i.e., chamber height and length. To elaborate effect of chamber height $a_{\text{tx/rx}}$, chamber transfer function is investigated for channel length l_{ch} of 10μm with respect to various chamber heights from 100μm to 250μm in Fig. 20(a). To illustrate the effect of chamber length $l_{\text{tx/rx}}$, chamber transfer function is investigated for a chamber height $a_{\text{tx/rx}}$ of 150μm with respect to various chamber lengths from $1\mu m$ to 200μm in Fig. 20(b).

In Fig. 20(a), it is observed that as the chamber height decreases, i.e., for a shorter chamber height, the signal is exposed to less attenuation. The concentration signals with higher frequency can be transported with less attenuation at the transition junction from/to the shorter height chambers to/from microfluidic channel compared to the longer height chambers. In Fig. 20(b), when the chamber length is decreased from 200μm to 1μm, the achievable frequencies are decreased as well. While $l_{\text{tx/rx}}$ is equal to 50, 100, and 200 μm attenuation due to diffusion dominates and junction transition effect is negligible, however, for $l_{\text{tx/rx}} = 1\mu$m, attenuation due to junction transition outweighs the diffusion attenuation.

Overall, the chamber transfer function is equal to 0 when the wave number k is a positive integer, i.e., i, multiple of the reciprocal of the chamber height, i.e., $1/(a_{\text{tx/rx}})$, as

$$k = \frac{1}{a_{\text{tx/rx}}} i \tag{150}$$

This effect is peculiar to the concentration propagation at the chamber junction, and it is due to the transition that cancel out the frequency components given by (150) at the output

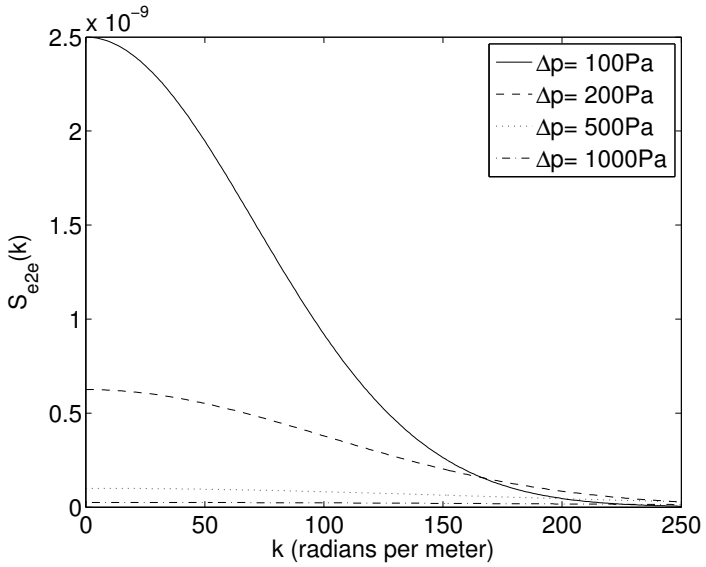

Figure 22: The end-to-end propagation noise CSD based on the pressure drop across the microfluidic channel.

signal. To explain quantitatively, the chamber junction transition performs the integration of the input signal, and since the integration of a sinusoidal signal over a complete period, or the multiple complete periods would yield 0, the frequency components matching this definition vanish, which are stated in (150).

3.6.2 End-to-end Propagation Noise

In Section 3.4.3, it is shown that the CSD of noise at microfluidic channel dominates the CSD of the noises at chambers. Therefore, the end-to-end propagation noise CSD is studied in three parts, i.e., the microfluidic channel length l_{ch}, the turning angle θ, and the pressure drop Δp. To elaborate effect of the microfluidic channel length l_{ch}, the end-to-end CSD is investigated for a pressure drop Δp of 500Pa, height a_{ch} and width b_{ch} of 25 and 5 μm with respect to the various lengths from 20mm to 100mm in Fig. 21(a). To illustrate effect of the turning angle θ on the end-to-end noise CSD, l_{ch} is assumed as 100 mm, and the end-to-end CSD is investigated with respect to various turning angles from $\pi/6$ to π radians in Fig. 21(b). To illustrate effect of the pressure drop Δp on end-to-end noise CSD, end-to-end CSD is investigated with respect to various pressure drop values from 100 Pa to 1000 Pa in Fig. 22.

It is observed in Fig. 21(a) that as the distance between transmitter and receiver chambers increases, frequency range of the flat-band CSD decreases, i.e., as the microfluidic channel length decreases, the flat-band region of the end-to-end propagation noise CSD increases. Therefore, AWGN channel assumption for FMC holds for a limited range of frequencies based on the l_{ch}. Furthermore, the noise variance decreases by 10 times while the distance is decreased from 100 mm to 20 mm. Moreover, in Fig. 21(b), it is shown that turning channel effect is negligible for the end-to-end propagation noise CSD. In Fig. 22, it is shown that the flat-band region of end-to-end CSD increases from a few radians per meter to the order of 100 radians per meter, while pressure drop is increased from 100 to 1000 Pa. The end-to-end propagation noise variance is reduced while the pressure drop is increased from 100 to 1000 Pa, as well. Furthermore, these frequency ranges also conform with the biological oscillators based on quorum sensing [27]. Therefore, end-to-end propagation noise in FMC over microfluidic channels can be approximated as AWGN for microfluidic channels with sufficient channel length l_{ch} and pressure drop Δp.

Overall, the performed CSD analysis provides a basis for characterization of noise at the receiver based on the microfluidic channel parameters. Here, we focus on flat-band region, and the AWGN channel model for FMC over microfluidic channels. However, using proposed end-to-end propagation noise CSD, analysis of frequencies beyond flat-band region can also be performed for MC, such as colored noise models can be developed.

3.7 Highlights

In this chapter, first, the propagation model for microfluidic channels is extended to incorporate the impact of the molecular transmitter and receiver placed in the chambers (see Fig. 1). Diffusion-based molecular propagation and transition from chambers to the microfluidic channel are studied and mathematically modeled.

In communication systems, noise represents the imperfections or random errors that negatively effects the communication performance (information rates). The noise effects in the microfluidic molecular communication system are identified as: 1) transition from/to molecular transport by diffusion in the transmitter/receiver chamber to/from molecular

transport by flow in the microfluidic channel; and 2) the random diffusion of molecules inside the chambers and microfluidic channel. These two noise effects are treated as the building blocks of the overall noise on the molecular signal.

To model the noise effects, spectral density of the molecular signal is formulated. The spectral density incorporates the physical parameters of the microfluidic channels. Flat-band frequency ranges in the spectral density are identified. It is shown that for the varying molecular signals, noise distribution can be approximated as white Gaussian.

In the second part of this work, transmission of a sequence of molecular signals is investigated. Previously transmitted molecular signals in a sequence diffuse throughout the microfluidic channel and cause disturbance on the current transmission. Utilizing the developed propagation model for molecular communication over microfluidic channels, the impact memory on the current transmission is analytically modeled incorporating the transmission period parameters (duration between the molecular signals in a sequence) and the distance between the transmitter and receiver.

The analysis of the noise and memory effects in this work using mathematical modeling expand the knowledge on molecular communication over microfluidic channels and aims to further support the investigation on communication performance in terms of information rates and bit-error rate. The results provided in this chapter of the thesis constitute an initial study on the noise effects on a basic design of a microfluidic molecular communication system (see Fig. 1), and further study is expected in the future to utilize these results to analyze more specific microfluidic molecular communication system implementations.

CHAPTER IV

INTERFERENCE MODELING AND CAPACITY ANALYSIS FOR MICROFLUIDIC MULTIPLE ACCESS CHANNEL

In this chapter, the impact of the interference on the molecular communication (MC) between a transmitter and receiver pair which are connected through a microfluidic channel containing fluid flow is investigated. The interference modeling and the capacity analysis is performed based on the microfluidic channel geometry, the flow velocity, and the distance. Additionally, three different microfluidic interference channel configurations, i.e., both-sided interference (microfluidic X channel), one-sided interference (microfluidic Z channel), and interference-free, are proposed based on the distance of the receiver from the interfering transmitter, microfluidic channel cross-section, and the fluid flow velocity. This work was first presented in [3]. In Section 4.2, we provide the system model for the MC over microfluidic channels. In Section 4.3, we model the interference in the microfluidic channels. In Section 4.4, capacity of the microfluidic MC channel under interference is investigated. In Section 4.5, MIC configurations are presented.

4.1 Motivation

Towards enabling the parallel molecular processing and computation on a chip, microfluidic channels can also be used to connect multiple transmitter and receiver pairs. The microfluidic MC channel, can empower parallel testing, processing, and preparation of the chemical samples on a microfluidic chip. In the multi-pair MC communication system, we consider that each transmitter is aimed to communicate using same type of molecules with only its designated receiver. However, the transmissions of multiple transmitters using same type of molecules yield interference to each other. The interference effect coupled with the physical limitations of microfluidic channels call for a thorough analysis and efficient design of MC schemes to realize nano communications in microfluidic platforms. The research on the information-theoretic study of the MC has been a field of interest recently [12], [41], [65],

[66]. So far, to the best of our knowledge, there is no prior work on analytical modeling of interference and capacity analysis for microfluidic channels from the MC point of view.

In [67], for the MC based on free-space diffusion, modeling of interference is performed for multiple transmitting nanomachines. The transmitters are taken to be spatial Poisson distributed, and the statistics of the received signal is studied. The provided analysis aims to characterize interference in free-space MC under random distribution of transmitters, which is not applicable to microfluidic MC channels. In [12], the information capacity of a free-space MC system is investigated. The capacity is expressed based on the diffusion constant, the distance between the transmitter and the receiver, and the bandwidth of the transmitted signal. Additionally, the thermodynamic power spent at the transmitter for molecule emission is used for capacity evaluation. The capacity formulation for MC is applicable only for single molecular transmitter and receiver pair, and for purposes of solely diffusion-based molecular propagation. In [41], the information capacity in a molecular nanonetwork is investigated based on stochastic models in chemically reacting systems. The free-space MC models for a transmitter and receiver pair, single transmitter and multiple receivers, and multiple transmitter and single receiver scenarios are proposed. For each of these models, the capacity expressions are derived for molecular transport solely based on diffusion. However, the capacity analyses in [12, 41] do not capture the attenuation, and the noise characteristics of the flow-induced molecular transport and are not suitable for the MC over microfluidic channels.

In this chapter, based on the channel modeling and the noise analysis performed in [1] and [2], respectively, we investigate the interference effects and the capacity of the microfluidic MC channel, i.e., Microfluidic Interference Channel (MIC). The interference amplitude and variance, and the interference-induced noise at the receiver are modeled first. In the course of this work, we focus on the received signal level and do not assume any underlying encoding and modulation schemes. Then, the MC link capacity under interference is studied for the single interfering transmitter and the multiple interfering transmitter cases. The impact of the distance as well as the number of interfering transmitters are investigated.

The microfluidic MC channel capacity is shown to be severely constrained under the interference, which requires development of practical detection schemes considering capabilities of the biological molecular receivers, e.g., genetically engineered bacteria, to distinguish transmission of designated transmitter from interferer signals.

Furthermore, the placement of the chambers on the opposite sides of the microfluidic channel is also investigated for two pairs of transmitter and receiver. Each transmitter communicates with its designated receiver on the same side of the microfluidic channel, and causes interference to the undesignated receiver on the opposite side based on the flow velocity and the microfluidic channel configuration. Accordingly, three microfluidic channel configurations are presented based on the distance of the receiver from the interfering transmitter, microfluidic channel cross-section and the fluid flow: 1) microfluidic X channel, i.e., both receivers are exposed to interference, 2) microfluidic Z channel, i.e., only one of the receivers is exposed to the interference, and 3) microfluidic interference-free channel, i.e., none of the receivers is exposed to interference. The provided analysis for capacity, enables information-theoretic evaluation of the microfluidic MC systems. The throughput and the accuracy of these systems can be assessed via the information theory.

4.2 Microfluidic Molecular Communication Channel

In this section, we present the system model for the microfluidic MC channel, which forms the basis of interference modeling and capacity analysis. The microfluidic channel and chamber dimensions are illustrated in Fig. 1. The molecular transmitter and the receiver are placed in the chambers which are attached to a connecting microfluidic channel with fluid flow. It can be inferred from [2] that the microfluidic MC channel can be reasonably modeled as a linear communication channel, and the memoryless AWGN model of a microfluidic MC system can be developed when the range of frequencies for a molecular signal is limited to a few mHz, which conforms with the capabilities of biological oscillators such as genetically engineered bacteria [27, 71, 73, 43].

The transmitter node modulates information on the molecular signal x by changing the level, i.e., the amount, of the released molecular concentration. We assume the transmitter

nodes are adjusted to change the released concentration level with a rate of $f_0 = 1/T_0$, and T_0 is the period of the signal. Furthermore, we assume the bandwidth of the molecular receiver is greater or equal to f_0, i.e., the molecular receiver is capable of responding the changes in the received signal level with a frequency of f_0. Therefore, the molecular receiver can respond to changes in the input signal with frequency f_0 by the transmitter. The transmitted molecular signal x is subject to a variance constraint ϕ^2 for each transmission as

$$\mathrm{E}[x^2] \leq \phi^2 \tag{151}$$

The received molecular signal y is given by

$$y = \alpha x + n \tag{152}$$

where α is the channel gain, and n is AWGN [2]. We provide below the complete channel model for the MC link between a transmitter and a receiver pair, i.e., point-to-point MC link.

4.2.1 Attenuation

The fluid flow is characterized as laminar, steady, unidirectional, and driven by the pressure drop across the microfluidic channel [16]. For the rectangular cross-section microfluidic channel, the area-averaged flow velocity u_{ch}, which is also the propagation velocity through the microfluidic channel, is given by [15]

$$u_{\mathrm{ch}} = \frac{a_{\mathrm{ch}}^2}{12\mu l_{\mathrm{ch}}} \left(1 - 0.63\frac{a_{\mathrm{ch}}}{b_{\mathrm{ch}}}\right) \Delta p \tag{153}$$

where μ is the viscosity of the fluid, l_{ch} is the microfluidic channel length, a_{ch} is the microfluidic channel height, b_{ch} is the microfluidic channel width, and Δp is the pressure drop across the microfluidic channel. Molecular transport via the fluid flow is modeled via the one-dimensional solution of the convection-diffusion equation for the microfluidic channel [29, 30, 31, 32, 33].

In this chapter, we use the temporal frequency f for analysis, apart from our former works based on spatial frequency ν, i.e., in radians $k = 2\pi\nu$ [1, 2]. The equality of both

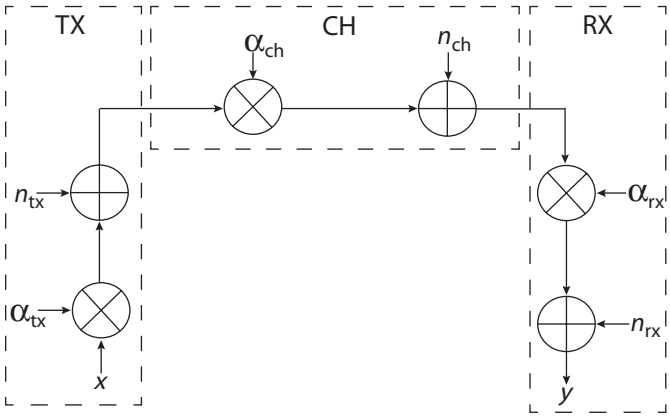

Figure 23: Block diagram representation of the microfluidic AWGN channel.

representations for molecular propagation is presented in [1]. The conversion is provided by [1]

$$f = \frac{k}{2\pi u} \tag{154}$$

where u is the propagation velocity in the medium. While spatial frequency provides compact representation for formulations, temporal frequency is preferred during the course of this work to relate our results to time-scale and the operating frequency of the molecular transmitters and receivers.

The block diagram representation of signal propagation between the transmitter and the receiver pair is given in Fig. 23. We take the transmitter and the receiver chambers identical, i.e., the gains of the transmitter and the receiver chambers are equal. The end-to-end channel gain α is defined as

$$\alpha = \alpha_{\text{ch}} \alpha_{\text{tx/rx}}^2 \tag{155}$$

where α_{ch} is the gain of the microfluidic channel, $\alpha_{\text{tx/rx}}$ is the gain of the transmitter and the receiver chambers. Both chambers have equal gain, i.e., $\alpha_{\text{tx/rx}} = \alpha_{\text{tx}} = \alpha_{\text{rx}}$, since the transmitter and chambers are taken to be identical. For the microfluidic channel, the signal gain is given in [2] based on the obtained impulse response for the microfluidic channel with the laminar flow in [1]. Here, we assume the microfluidic channel is straight, and hence, the

signal gain α_{ch} in [2] reduces to

$$\alpha_{\text{ch}} = \exp(-\frac{4\pi^2 f_0^2}{u_{\text{ch}}^2} D\tau_{\text{ch}}) \tag{156}$$

where D is the Taylor dispersion adjusted diffusion coefficient for the rectangular microfluidic channels, which is given by [51]

$$D = \left(1 + \frac{8.5u_{\text{ch}}^2 a_{\text{ch}}^2 b_{\text{ch}}^2}{210D_0^2(a_{\text{ch}}^2 + 2.4a_{\text{ch}}b_{\text{ch}} + b_{\text{ch}}^2)}\right) D_0, \tag{157}$$

and τ_{ch} is the propagation delay from the transmitter chamber to the receiver chamber, which is referred as extended microfluidic channel delay in [2] and given by

$$\tau_{\text{ch}} = \frac{l_{\text{ch}} + a_{\text{tx/rx}}}{u_{\text{ch}}} \tag{158}$$

where $a_{\text{tx/rx}}$ is the width of transmitter and receiver chambers. Both chambers have equal width, i.e., $a_{\text{tx/rx}} = a_{\text{tx}} = a_{\text{rx}}$, since the transmitter and the receiver chambers are taken to be identical, which is illustrated in Fig. 1.

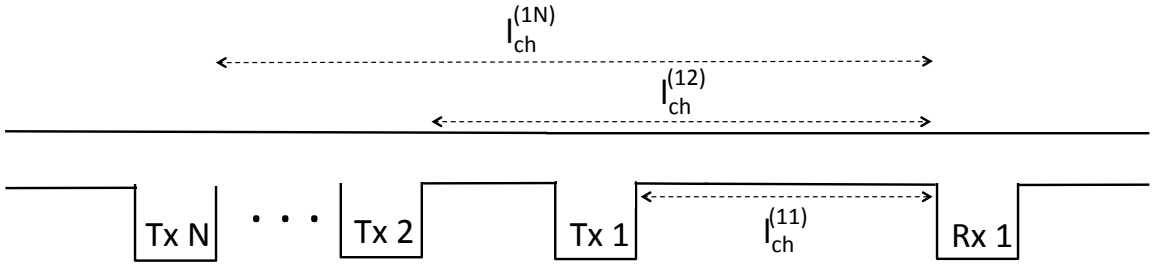

Figure 24: The illustration of the multiple transmitters (Tx1, Tx 2, $\cdots$, Tx N), and the receiver (Rx 1) placed on the microfluidic channel. The distances $l_{\text{ch}}^{(11)}$, $\cdots$, $l_{\text{ch}}^{(1N)}$ represent the separation between the transmitters and the Rx 1.

For the identical transmitter and the receiver chambers, the signal gain is obtained as [2]

$$\alpha_{\text{tx/rx}} = \exp(-\frac{4\pi^2 f_0^2}{u_{\text{tx/rx}}^2} D_0\tau_{\text{tx/rx}})\text{sinc}(\frac{a_{\text{tx/rx}}}{u_{\text{tx/rx}}} f_0) \tag{159}$$

where $\tau_{\text{tx/rx}}$ and $u_{\text{tx/rx}}$ is the propagation delay and the propagation velocity, respectively, at the transmitter and the receiver chambers. Due to the identical dimensions, the propagation delays at the both chambers are equal, i.e., $\tau_{\text{tx/rx}} = \tau_{\text{tx}} = \tau_{\text{rx}}$, which is given by [2]

$$\tau_{\text{tx/rx}} = \frac{l_{\text{tx/rx}}^2}{2D_0} \tag{160}$$

where $l_{\mathrm{tx/rx}}$ is the distance of the transmitter and the receiver placed in the chambers to the microfluidic channel, which is illustrated in Fig. 1. The distances inside the identical chambers are equal for both transmitter and receiver, i.e., $l_{\mathrm{tx/rx}} = l_{\mathrm{tx}} = l_{\mathrm{rx}}$. The propagation velocity at the both chambers are also equal, i.e., $u_{\mathrm{tx/rx}} = u_{\mathrm{tx}} = u_{\mathrm{rx}}$, which is obtained using (160) as

$$\begin{aligned} u_{\mathrm{tx/rx}} =& \frac{l_{\mathrm{tx/rx}}}{\tau_{\mathrm{tx/rx}}} \\ =& \frac{2D_0}{l_{\mathrm{tx/rx}}} \end{aligned} \tag{161}$$

The received signal is said to be under the effect of memory when the molecular signal period is less than the propagation duration of the signal through the microfluidic channel, i.e., the following condition is satisfied [2]

$$\frac{1}{f_0} < \tau_{\mathrm{ch}} \tag{162}$$

During this study, we focus on the frequencies in the range of a few millihertz (mHz) based on the capabilities and time-scale of the bacteria-based receivers, which are proposed as the potential nanomachines to test and implement molecular receivers [9, 71, 73]. Therefore, for the physical system we have, $1 \gg f_0 \tau_{\mathrm{ch}}$, and hence, MC channel can be taken as memoryless.

4.2.2 Molecular Noise

For sufficiently small frequencies, i.e., the frequency range of biological oscillators based on the genetically engineered bacteria, spectral density of the received molecular signal is shown to be flat, and hence, the Gaussian distribution assumption is valid for molecular noise [2]. Therefore, the microfluidic MC channel can be treated as a AWGN channel for sufficiently small transmission frequency ranges.

The noise effects on the received signal are illustrated in the block diagram in Fig. 23. The propagation noise n is composed of the transmitter/receiver chamber, and the microfluidic channel noises. The molecular propagation noise is shown to be well-approximated based on microfluidic channel noise in [2]. The variance of the microfluidic channel noise

σ^2 of the n is derived in [2] as

$$\sigma^2 = (2\alpha_{\text{tx/rx}}^4 \frac{D\tau_{\text{ch}}}{u_{\text{ch}}^2} + 4\frac{D_0\tau_{\text{tx/rx}}}{u_{\text{tx/rx}}^2}\alpha_{\text{ch}}^2\alpha_{\text{tx/rx}}^2)4\pi^2 f_0^2\phi^2 \tag{163}$$

The distribution of propagation noise n is taken as

$$n \sim \mathcal{N}\left(0, \sigma^2\right) \tag{164}$$

Next, we model interference in microfluidic channels before proceeding to the capacity analysis.

4.3 Interference in Microfluidic Molecular Communication Channel

In this section, an interference model for MIC is presented. Each transmitter attempts to communicate with the receiver, meanwhile causing interference to other transmitters signal at the receiver, which is illustrated in Fig. 24. We assume there is no coordination among the transmitters.

We characterize the interference based on the received signal rather than assuming employed modulation and coding techniques. The interference effect is modeled based on the flow velocity, channel dimensions, and the distance between the transmitters and the receiver. In the following subsections, we present an analytic model for the interference magnitude and interference-induced noise.

4.3.1 Interference Magnitude and Variance at the Receiver

For the interference modeling, we assume that all chambers are identical. The channel gain α_{ij} for the interfering signal from transmitter j at the receiver i is obtained based on (155) as

$$\alpha_{ij} = \alpha_{\text{ch}}^{(ij)}\alpha_{\text{tx/rx}}^2 \tag{165}$$

where $\alpha_{\text{tx/rx}}$ is given in (159), and $\alpha_{\text{ch}}^{(ij)}$ is the microfluidic channel gain between the transmitter j and the receiver i, which is given based on (156) as

$$\alpha_{\text{ch}}^{(ij)} = \exp(-\frac{4\pi^2 f_0^2}{u_{\text{ch}}^2} D\tau_{\text{ch}}^{(ij)}) \tag{166}$$

where $\tau_{\text{ch}}^{(ij)}$ is the delay between the transmitter j and receiver i, which is given based on the distance $l_{\text{ch}}^{(ij)}$ between interferer chamber j and the receiver chamber i using (158) as

$$\tau_{\text{ch}}^{(ij)} = \frac{l_{\text{ch}}^{(ij)}}{u_{\text{ch}}} \tag{167}$$

The variance ζ_{ij}^2 of the interference from interferer j at the receiver i is defined to incorporate the interference at the receiver i as

$$\zeta_{ij}^2 = (\alpha_{\text{ch}}^{(ij)})^2 \alpha_{\text{tx/rx}}^4 \phi_j^2 \tag{168}$$

where ϕ_j^2 is the interferer signal variance. Furthermore, the memory condition given in (162) also does not hold for interferer signals, i.e.,

$$\frac{1}{f_0} \gg \tau_{\text{ch}}^{(ij)} \tag{169}$$

Therefore, all transmissions in the MIC are memoryless. Next, we analyze the interference-induced noise of the MIC link using the performed modeling for interference magnitude here.

4.3.2 Interference-induced Molecular Noise

In MIC, the receiver i is also exposed to the interference-induced noise n_{ij} from transmitter j. The noise in the microfluidic channel is shown to be dominating the noise in the chambers [2]. The interference-induced noise variance ξ_{ij}^2 at the receiver i due to the interference caused by transmitter j can be obtained based on the attenuation in the microfluidic channel as

$$\xi_{ij}^2 = (1 - (\alpha_{\text{ch}}^{(ij)})^2) \alpha_{\text{tx/rx}}^4 \phi_j^2 \tag{170}$$

For the frequency range of interest, i.e., a few mHz, the molecular noise is shown to be taken distributed as white Gaussian [2]. Thus, the distribution interference-induced noise n_{ij} is given by

$$n_{ij} \sim \mathcal{N}\left(0, \xi_{ij}^2\right) \tag{171}$$

Table 3: The values of the Physical Parameters

Parameter	Value
D_0 (Diffusion constant)	$10^{-9}\mathrm{m}^2/\mathrm{s}$
a_{ch} (microfluidic channel width)	$250\mu\mathrm{m}$
b_{ch} (microfluidic channel height)	$10\mu\mathrm{m}$
$a_{\mathrm{tx/rx}}$ (chamber width)	$150\mu\mathrm{m}$
$l_{\mathrm{tx/rx}}$ (chamber length)	$1\mu\mathrm{m}$
u_{ch} (flow velocity)	$10^{-2}\mathrm{m/s}$

4.3.3 Multiple Transmitters

Due to received signal from multiple transmitters, we assume that the molecular receiver is capable of detecting and producing a distinct response for multiple levels of received concentration signal. Furthermore, the largest distance between transmitters and the receiver, i.e., the distance between Tx N and the RX in Fig. 24, is sufficiently small, i.e.,

$$T_0 \gg \frac{l_{\mathrm{ch}}^{(1N)} + a_{\mathrm{tx/rx}}}{u_{\mathrm{ch}}}, \tag{172}$$

that all signals can be taken as received all together, and then, a total response is produced by the molecular receiver. Moreover, the difference in transmission instants of multiple transmitters is negligible due to low rate of change in the signal level f_0, i.e., large signal period T_0 compared to the total propagation delay as stated in (172).

4.4 Capacity Analysis

In this section, we analyze the capacity of the microfluidic MC channel under the interference from single and multiple interferer transmitter cases. The Signal-to-Interference and Noise Ratio (SINR) and capacity expressions are derived for the MIC, and the impact of physical parameters is elaborated.

4.4.1 Single Interferer

Here, we assume there are two transmitters that are attached to the microfluidic channel, i.e., Tx 1 and Tx 2 in Fig. 24. The transmitters cause interference to each other at the receiver. We focus on the individual MC capacity of the transmitters with a receiver

connected to the microfluidic channel, i.e., RX in Fig. 24. Therefore, the impact of the interference from a single interferer transmission on the MIC capacity is investigated.

4.4.1.1 SINR

The variance of the received signal at the receiver i under the interference is given by

$$\psi_i^2 = \alpha_i^2 \phi_i^2 + \sigma_i^2 + \zeta_{ij}^2 + \xi_{ij}^2 \tag{173}$$

where α_i and ϕ_i^2 represent the channel gain and the variance of the transmitted molecular signal, respectively; ζ_{ij}^2 represent the variance of the interference component in the received signal caused by the interferer j at the receiver i; σ_i^2 is the variance of the molecular propagation noise at receiver i; ξ_{ij}^2 represents the variance of the interference-induced noise in the received signal caused by the interferer j at the receiver i. The computation of α_i, σ_i^2, ζ_{ij}^2, and ξ_{ij}^2 are given in (155), (163), (168) and (170) respectively. Overall, the noise distribution for MIC is given by

$$\begin{aligned} n_i \sim & n_{ii} + n_{ij} \\ \sim & \mathcal{N}\left(0, \sigma_i^2 + \xi_{ij}^2\right) \end{aligned} \tag{174}$$

Signal-to-Interference and Noise Ratio (SINR) at receiver i under interference from interferer j is obtained as

$$\text{SINR}_i = \frac{\psi_i^2}{\sigma_i^2 + \zeta_{ij}^2 + \xi_{ij}^2} \tag{175}$$

4.4.1.2 Capacity

In our analysis, we look at the frequencies in the range of few mHz such that MC channel can be taken as linear [2]. We further assume that the transmitted signal is drawn from a Gaussian distribution. Accordingly, we utilize the AWGN channel capacity as the basis of our analysis.

The mutual information among the transmitter i and the receiver i under the interference from transmitter j can be found via definition of the mutual information and the entropy

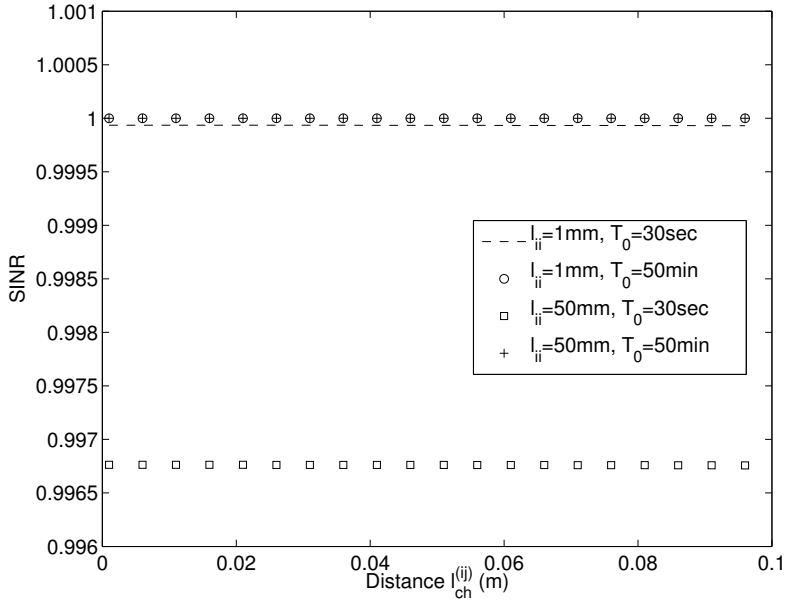

Figure 25: SINR with respect to the interferer distance $l_{\text{ch}}^{(ij)}$.

of a Gaussian random variable given in [68] as

$$\begin{aligned} I(x_i;y) =& \frac{1}{2}\log_2\left(2\pi e\left(\alpha_{ii}^2\phi_i^2+\zeta_{ij}^2+\sigma_i^2+\xi_{ij}^2\right)\right) \\ & -\frac{1}{2}\log_2\left(2\pi e\left(\zeta_{ii}^2+\zeta_{ij}^2+\sigma_i^2+\xi_{ij}^2\right)\right) \\ =& \frac{1}{2}\log_2\left(1+\frac{\alpha_{ii}^2\phi_i^2}{\zeta_{ij}^2+\sigma_i^2+\xi_{ij}^2}\right) \text{ bits per channel use} \end{aligned} \tag{176}$$

Based on the fact that transmitter changes the transmitted signal level with an interval of $1/f_0$, i.e., degrees of freedom per second is f_0, which can also be perceived as the channel use duration, so the capacity is

$$C_i = \frac{1}{T_0}\log_2\left(1+\frac{\alpha_i^2\phi_i^2}{\sigma_i^2+\zeta_{ij}^2+\xi_{ij}^2}\right) \text{ bits/second} \tag{177}$$

Under the assumption that the variance of the transmitted signals from both transmitters are equal, i.e., $\phi_i^2=\phi_j^2$, the capacity of the MC link between the designated transmitter i and the receiver i under a single interferer j can be obtained based on the physical system

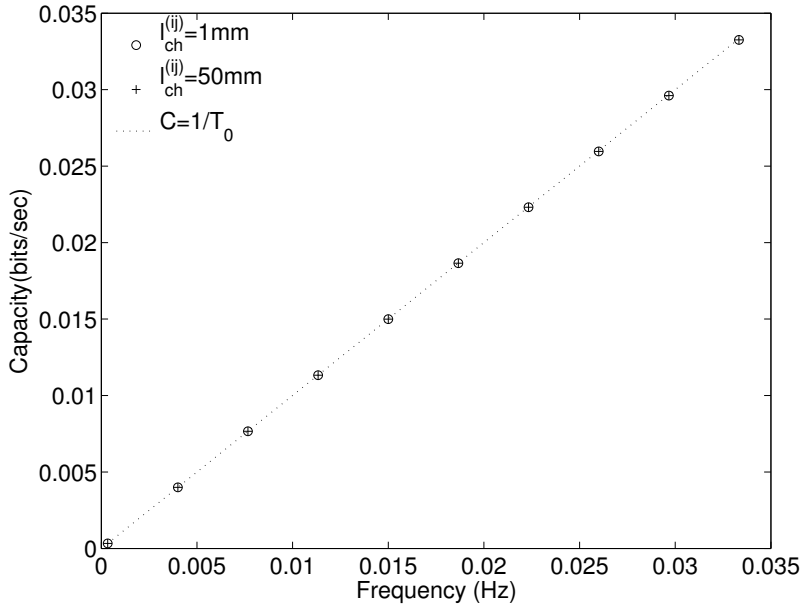

Figure 26: Capacity with respect to the frequency $f_0 = 1/T_0$.

parameters as

$$C_i = \frac{1}{T_0}\log_2\left(1+\alpha_i^2\Big/\Big(\right.$$
$$+\left(2\alpha_{\text{tx/rx}}^4\frac{D\tau_{\text{ch}}^{(ii)}}{u_{\text{ch}}^2}+4\frac{D\tau_{\text{tx/rx}}}{u_{\text{tx/rx}}^2}(\alpha_{\text{ch}}^{(ii)})^2\alpha_{\text{tx/rx}}^2\right)4\pi^2\frac{1}{T_0^2}$$
$$\left.+\alpha_{ij}^2+(1-(\alpha_{\text{ch}}^{(ij)})^2)\alpha_{\text{tx/rx}}^4\phi_j^2\Big)\right)\text{bits/second} \tag{178}$$

The SINR and the capacity for the single interferer case are studied numerically in Fig. 25 and Fig. 26, respectively. For the evaluations, the parameter values given in Table 3 are used. We characterize the SINR and the capacity with respect to the distance $l_{\text{ch}}^{(ij)}$ between the interfering transmitter j and the designated receiver i. The distance $l_{\text{ch}}^{(ii)}$ between the designated transmitter i and the designated receiver i is evaluated at 1mm and 50mm. The period T_0 of the receiver is evaluated at 30sec and 50min.

In Fig. 25, the SINR at the receiver i is presented with respect to the distance of the interferer transmitter. The SINR curves are shown to be upper bounded by 1 and stay constant for various T_0 and $l_{\text{ch}}^{(ii)}$ pairs. In Fig. 26, we study of the capacity under a single interferer with respect to f_0. Since the SINR is constant and almost equal to 1, capacity is

shown to be linearly scaling with the reciprocal of the channel use duration. Additionally, it should be noted that the channel capacity curves in Fig. 26 overlaps for different $l_{\text{ch}}^{(ij)}$ values due to negligible change in the SINR.

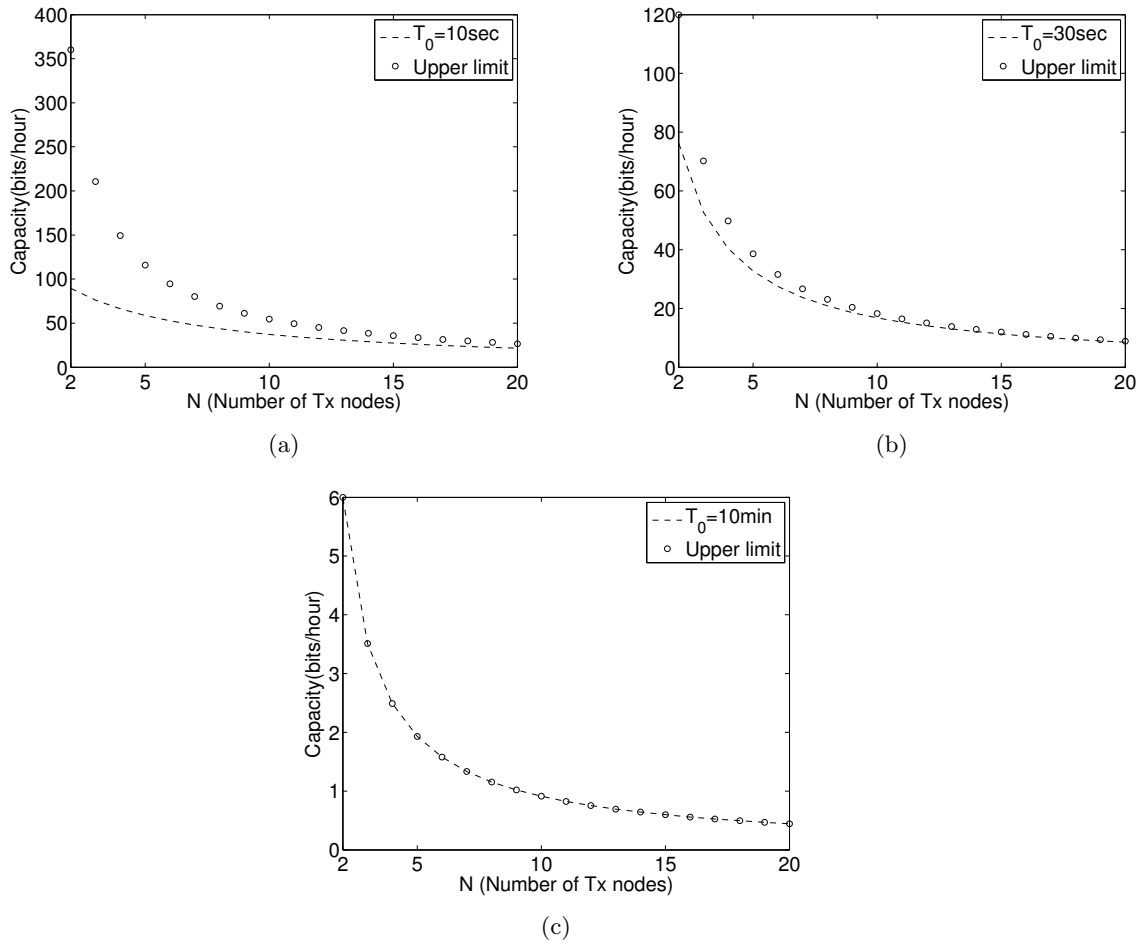

Figure 27: The capacity under multiple interferers in (182) versus the upper limit in (183) for $T_0 = 10$sec (a), $T_0 = 30$sec (b), and $T_0 = 10$min (c).

4.4.2 Multiple Interferers

Here, we assume there are multiple transmitters that are attached to the microfluidic channel, i.e., Tx 1 to Tx N in Fig. 24. The impact of interference from multiple interferers on the MC capacity of a single transmitter and receiver pair is studied.

4.4.2.1 SINR

Under multiple interferers, the variance of the received signal at the receiver i is given by

$$\psi_i^2 = \alpha_i^2 \phi_i^2 + \sigma_i^2 + \sum_{j=2}^{N} \zeta_{ij}^2 + \xi_{ij}^2 \tag{179}$$

where N is the number of transmitters. We take Tx 1 as the designated transmitter with $N-1$ remaining interferers. Overall, the noise distribution under multiple interferers is given by

$$\begin{aligned} n_i \sim & n_{ii} + \sum_{j=2}^{N} n_{ij} \\ \sim & \mathcal{N}\left(0, \sigma_i^2 + \sum_{j=2}^{N} \xi_{ij}^2\right) \end{aligned} \tag{180}$$

Accordingly, the SINR at receiver i under interference is obtained as

$$\text{SINR}_i = \frac{\psi_i^2}{\sigma_i^2 + \sum_{j=2}^{N} \zeta_{ij}^2 + \xi_{ij}^2} \tag{181}$$

4.4.2.2 Capacity

Similar to single interferer case, based on the AWGN model, the capacity under multiple interferers is obtained as

$$C_i = \frac{1}{T_0} \log_2 \left(1 + \frac{\alpha_{ii}^2 \phi_i^2}{\sigma_i^2 + \sum_{j=2}^{N} \zeta_{ij}^2 + \xi_{ij}^2} \right) \text{bits/second} \tag{182}$$

We further extend our analysis over the case where the variances of the input signals from all transmitters are equal in value, i.e., $\phi_i = \phi_j$ for all $i, j \in \{1 \cdots N\}$. The capacity of the

receiver i is obtained based on physical system parameters as

$$
\begin{aligned}
C_i &= \frac{1}{T_0}\log_2\Bigg(1+\alpha_{ii}^2\Big/ \\
&\quad\Bigg(\Bigg(2\alpha_{\text{tx/rx}}^4\frac{D\tau_{\text{ch}}^{(ii)}}{u_{\text{ch}}^2}+4\frac{D\tau_{\text{tx/rx}}}{u_{\text{tx/rx}}^2}(\alpha_{\text{ch}}^{(ii)})^2\alpha_{\text{tx/rx}}^2\Bigg)4\pi^2\frac{1}{T_0^2} \\
&\quad+\sum_{j=2}^{N}(\alpha_{\text{ch}}^{(ij)})^2\alpha_{\text{tx/rx}}^4+(1-(\alpha_{\text{ch}}^{(ij)})^2)\alpha_{\text{tx/rx}}^4\Bigg)\Bigg) \\
&= \frac{1}{T_0}\log_2\Bigg(1+\alpha_{ii}^2\Big/ \\
&\quad\Bigg(\Bigg(2\alpha_{\text{tx/rx}}^4\frac{D\tau_{\text{ch}}^{(ii)}}{u_{\text{ch}}^2}+4\frac{D\tau_{\text{tx/rx}}}{u_{\text{tx/rx}}^2}(\alpha_{\text{ch}}^{(ii)})^2\alpha_{\text{tx/rx}}^2\Bigg)4\pi^2\frac{1}{T_0^2} \\
&\quad+(N-1)\alpha_{\text{tx/rx}}^4\Bigg)\Bigg) \\
&\leq \frac{1}{T_0}\log_2\left(\frac{N}{N-1}\right)\text{bits/second}
\end{aligned}
\tag{183}
$$

where we utilized the fact that attenuation is negligible due to signal period and practical distance values in the range of $1-100$mm, hence, $\alpha_{ii}^2\approx 1$, $\alpha_{\text{tx/rx}}\approx 1$, and $(2\alpha_{\text{tx/rx}}^4\frac{D\tau_{\text{ch}}^{(ii)}}{u_{\text{ch}}^2}+4\frac{D\tau_{\text{tx/rx}}}{u_{\text{tx/rx}}^2}(\alpha_{\text{ch}}^{(ii)})^2\alpha_{\text{tx/rx}}^2)4\pi^2\frac{1}{T_0^2}\approx 0$.

In (183), it is observed that channel capacity decays from 1 bit/per channel use to 0 as N increases from 2 to infinity. Furthermore, similar to single interferer case, capacity scales linearly with reciprocal with the channel use duration.

Numerical results are provided for capacity under multiple interferers in Fig. 27(a), Fig. 27(b), and Fig. 27(c) for $T_0=10$sec, $T_0=30$sec, and $T_0=10$min, respectively. The values of the physical parameters are listed in Table 3, $l_{\text{ch}}^{(11)}$ is set to 50mm, and the displacement between interfering Tx nodes is taken 0.5mm. The upper limit on capacity under multiple interferers in (183) is shown to be providing a better approximate of the capacity in (182) as T_0 is increased from 10sec to 10min. Accordingly, the provided upper limit can be regarded as a good approximation of the MC capacity under interference for the frequencies in the range of a few mHz and below, where biological molecular transceivers are expected to operate [43].

4.5 Microfluidic Interference Channel Configurations

Microfluidic interference channels can be realized via various design choices such as utilizing the concentration of distinct type of molecules for communication between different transmitter and receiver pairs, or placing different pairs on distinct microfluidic channels. The use of distinct molecules requires engineering of the specific transmitter and the receiver nodes capable of processing different types of molecular concentrations, meanwhile, the separation of different transmitter and receiver pairs onto distinct microfluidic channels requires larger microfluidic chip size area as well as additional micropumps. Here, we specifically investigate the placement of the two transmitter and receiver pairs on the opposite sides of the microfluidic channel, which use the concentration of same type of molecules for MC.

Each receiver is exposed to the interference from its undesignated transmitter on the opposite side, when its distance to the chamber of the undesignated transmitter is large enough, such that the transmitted signal by the undesignated transmitter j can traverse, i.e., diffuse across the microfluidic channel, and reach to the receiver placed at the opposing side. Using the delay expression for the diffusion-based propagation in (160), the condition for the distance between the transmitter j and the receiver i for the interference from the transmitter j at the receiver i is given by

$$l_{\mathrm{ch}}^{(ij)} \gg u_{\mathrm{ch}} \tau_{\mathrm{int}} \tag{184}$$

where $i \neq j$, and τ_{int} is the needed duration to have the interference by diffusion of the molecules from the one side of the channel to the opposing side, which is obtained via the diffusion delay as

$$\tau_{\mathrm{int}} = \frac{a_{\mathrm{ch}}^2}{2D_0} \tag{185}$$

In the following, we describe different MIC configurations based on the distance of the receivers to their corresponding interfering transmitter. Three MIC configurations, namely, the both-sided interference, i.e., the microfluidic X channel, the one-sided interference, i.e., the microfluidic Z channel, and the interference-free configuration are defined.

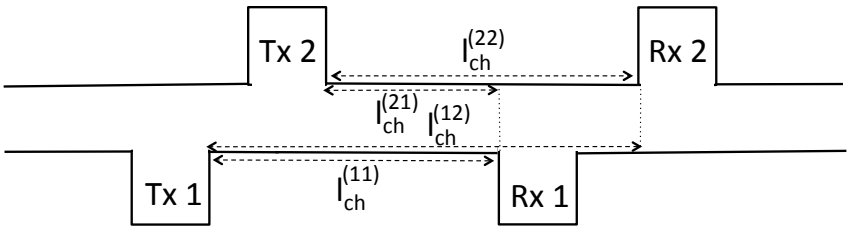

Figure 28: The microfluidic X, i.e., the both-sided interference, channel.

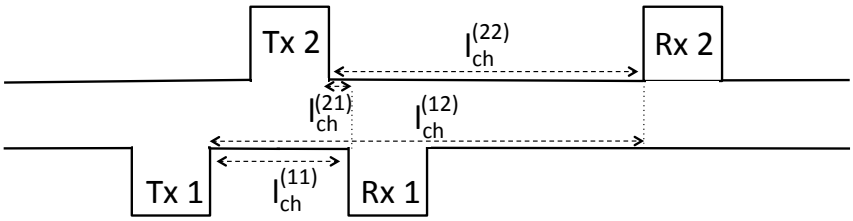

Figure 29: The microfluidic Z, i.e., the one-sided interference, channel.

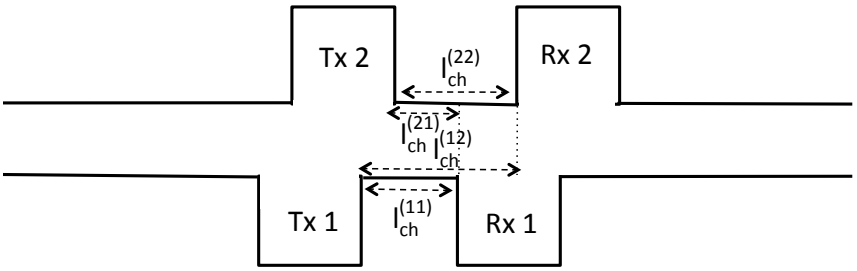

Figure 30: The microfluidic interference-free channel.

4.5.1 Microfluidic X Channel

In this configuration, both receivers are exposed to the interference from the non-designated transmitter, which is illustrated in Fig. 28. The necessary condition defined in (184) is satisfied for both receivers. The distances between both receivers and their corresponding undesignated transmitters are sufficiently large so that transmitted molecular signal can traverse across the microfluidic channel, i.e.,

$$l_{\mathrm{ch}}^{(12)} \gg u_{\mathrm{ch}}\tau_{\mathrm{int}}, \quad \text{and} \quad l_{\mathrm{ch}}^{(21)} \gg u_{\mathrm{ch}}\tau_{\mathrm{int}} \tag{186}$$

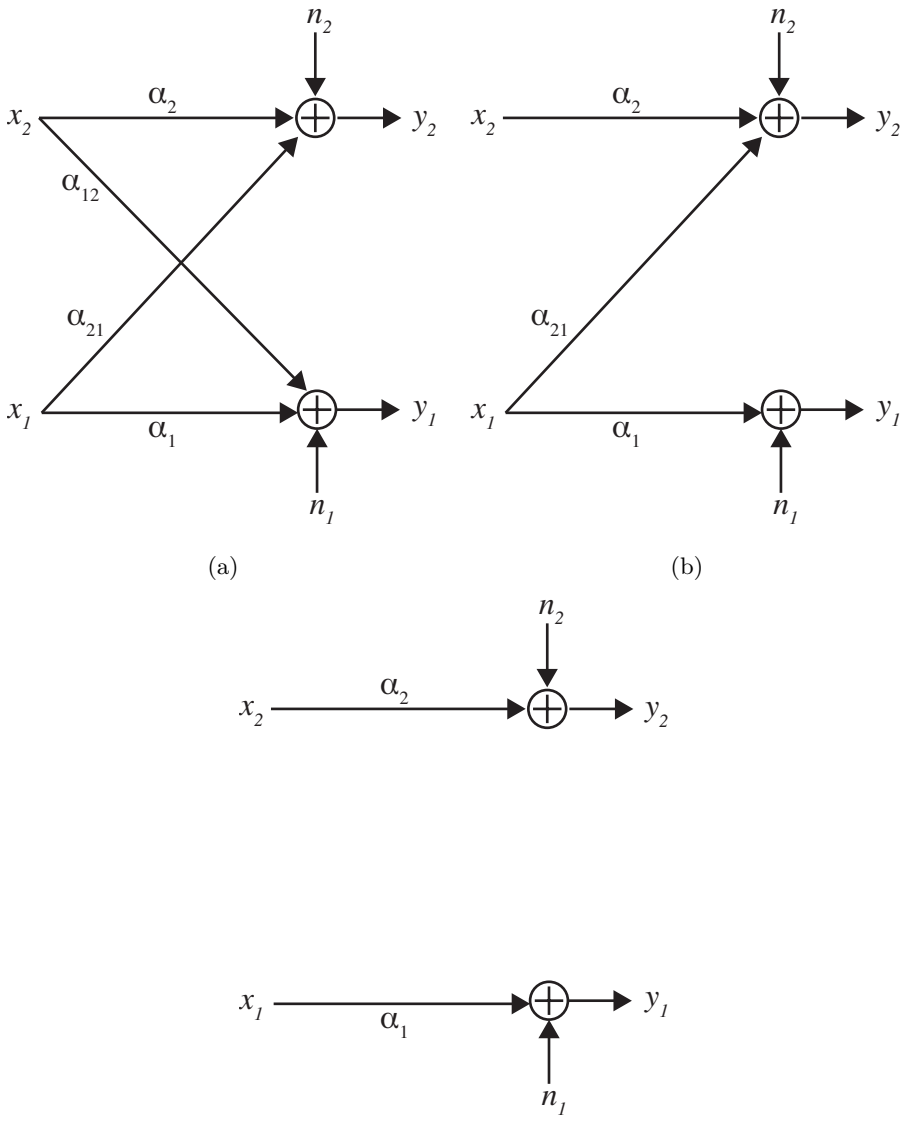

Figure 31: Block diagram representation of the three MIC configurations: both-sided interference (a), one-sided interference (b), and inferference-free (c).

The block diagram representation of the microfluidic X channel is given in Fig. 31(a). The capacity of the MC between the Tx 1 and the Rx 1 is obtained via (178) as

$$C_1 = \frac{1}{T_0}\log_2\left(1+\alpha_1^2\Big/\left(\left(2\alpha_{\text{tx/rx}}^4\frac{D\tau_{\text{ch}}^{(11)}}{u_{\text{ch}}^2}+4\frac{D\tau_{\text{tx/rx}}}{u_{\text{tx/rx}}^2}(\alpha_{\text{ch}}^{(11)})^2\alpha_{\text{tx/rx}}^2\right)4\pi^2\frac{1}{T_0^2}+(\alpha_{12}^2+(1-(\alpha_{\text{ch}}^{(12)})^2)\alpha_{\text{tx/rx}}^4\right)\right) \tag{187}$$

and likewise the capacity of the MC between the Tx 2 and the Rx 2 is

$$C_2 = \frac{1}{T_0}\log_2\Bigg(1+\alpha_2^2\Big/\Bigg(\Bigg(\Big(2\alpha_{\text{tx/rx}}^4\frac{D\tau_{\text{ch}}^{(22)}}{u_{\text{ch}}^2}+4\frac{D\tau_{\text{tx/rx}}}{u_{\text{tx/rx}}^2}(\alpha_{\text{ch}}^{(22)})^2\alpha_{\text{tx/rx}}^2\Big)4\pi^2\frac{1}{T_0^2} + (\alpha_{21}^2+(1-(\alpha_{\text{ch}}^{(21)})^2)\alpha_{\text{tx/rx}}^4\Big)\Bigg)\Bigg) \tag{188}$$

4.5.2 Microfluidic Z Channel

In this configuration, only one of the receivers is exposed to the interference, which is illustrated in Fig. 29. The required condition in (184) for interference holds only for one of the receivers. One of the receivers is placed sufficiently close to its undesignated transmitter such that the molecules released from undesignated transmitter do not travel to the opposing side of the microfluidic channel. Meanwhile the other receiver and its corresponding undesignated transmitter is sufficiently far apart so that the transmitted molecular signal can traverse the microfluidic channel from one side to the other. Thereby, based on Fig.29 the following conditions are satisfied:

$$l_{\text{ch}}^{(12)} \gg u_{\text{ch}}\tau_{\text{int}}, \quad \text{and} \quad l_{\text{ch}}^{(21)} \ll u_{\text{ch}}\tau_{\text{int}} \tag{189}$$

The block diagram representation of the microfluidic Z channel is presented in Fig. 31(b), where $\alpha_{12} = 0$. In this MIC configuration, the capacity of the MC between the Tx 1 and the Rx 1 is as in (187), while the MC capacity expression for Tx 2 and the Rx 2 in (188) reduces to

$$C_2 = \frac{1}{T_0}\log_2\Bigg(1+\alpha_2^2\Big/\Bigg(\Big(2\alpha_{\text{tx/rx}}^4\frac{D\tau_{\text{ch}}^{(22)}}{u_{\text{ch}}^2}+4\frac{D\tau_{\text{tx/rx}}}{u_{\text{tx/rx}}^2}(\alpha_{\text{ch}}^{(22)})^2\alpha_{\text{tx/rx}}^2\Big)4\pi^2\frac{1}{T_0^2}\Big)\Bigg) \tag{190}$$

4.5.3 Interference-free Configuration

When both receivers are at a distance to their corresponding undesignated transmitters closer than the required distance for the interference, none of the receivers are exposed

to the interference from its non-designated receiver, which is illustrated in Fig. 30. The condition given in (184) does not hold for both receivers, i.e.,

$$l_{\mathrm{ch}}^{(12)} \ll u_{\mathrm{ch}}\tau_{\mathrm{int}}, \quad \text{and} \quad l_{\mathrm{ch}}^{(21)} \ll u_{\mathrm{ch}}\tau_{\mathrm{int}} \tag{191}$$

This placement of the receivers is called the interference-free configuration. The interference-free configuration is illustrated in Fig. 31(c), where $\alpha_{12} = 0$ and where $\alpha_{21} = 0$. In this MIC configuration, the capacity of the MC between the Tx 1 and the Rx 1 is as in (190), while the MC capacity expression for Tx 1 and the Rx 1 in (187) reduces to

$$\begin{aligned} C_1 =& \frac{1}{T_0}\log_2\left(1+\alpha_1^2\Big/\right. \\ & \left.\left(2\alpha_{\mathrm{tx/rx}}^4\frac{D\tau_{\mathrm{ch}}^{(11)}}{u_{\mathrm{ch}}^2}+4\frac{D\tau_{\mathrm{tx/rx}}}{u_{\mathrm{tx/rx}}^2}(\alpha_{\mathrm{ch}}^{(11)})^2\alpha_{\mathrm{tx/rx}}^2\right)4\pi^2\frac{1}{T_0^2}\right)\right) \end{aligned} \tag{192}$$

4.6 Highlights

Multiple transmitters connected to the same microfluidic channel can enable parallel processing and computation for the applicatios of synthetic biology. However, when multiple transmitters access the microfluidic channel simultaneously, they cause multiple access interference to each other's molecular signals at their corresponding receiver.

In this work, the objective is the analysis of the communication performance under multiple access interference. Therefore, first, a model of the multiple access interference is developed utilizing the developed propagation and noise models in the previous chapters of this thesis. The developed multiple access interference model allows us to study the communication performance under arbitrary number of interfering transmitters.

Combining the developed models for propagation, noise, and interference with the information theory, an upper bound on the maximum achievable information rate (Shannon capacity) is obtained for single interferer and arbitrary number of interferers. Furthermore, for the double-sided placement of two transmitter and receiver pairs, microfluidic channel configurations are defined analogous to two-user interference channels in telecommunication systems: 1) both-sided interference (X channel), 2) one-sided interference (Z channel), 3) interference-free configuration.

CHAPTER V

DETECTION OF PAM MOLECULAR SIGNALS WITH BACTERIAL RECEIVERS ON A MICROFLUIDIC CHANNEL

In this chapter, the detection of the molecular signals using bacterial signal transduction is investigated. The input-output relation, the timing issues, and the noise effects for the bacteria response are characterized based on both analytical and experimental observations. Sampling schemes for the raw bacteria response are proposed based on the total response duration, the peak value, the ramp-up slope, and the ramp-down slope. The sampling based on the ramp-up slope is shown to be statistically favorable for the detection of PAM molecular signals. This work provides a basis for the sampling of the raw bacteria response and enables accurate detection of PAM molecular signals via bacterial response for MC and sensing applications. This work was first presented in [4]. In Section 5.2, the bacterial signal transduction is theoretically studied. In Section 5.3, the timing and noise issues in the bacteria response is investigated empirically based on experiments from a microfluidic platform. In Section 5.4, the sampling of the raw bacteria response is discussed, and the statistical characterization is performed. The detection of molecular signals via sampling the ramp-up slope is elaborated in Section 5.5.

5.1 Motivation

The molecular propagation have been extensively studied and can be found in many works [7, 10, 1, 2]. The information-theoretic fundamental limits related to MC are analyzed in [12, 3, 41]. A commonly taken approach is to consider nanomachines equipped with nanoscale molecular sensors that are capable of measuring received concentration [74, 75]. The undergoing biochemical processes for transmission and reception of molecular signals in the synthetic biological transceivers and their signal transduction pathways prove much more difficult to model and circumscribe [76, 77, 78, 79].

The goal of this work is to determine how the synthetic bacteria respond to external

variation in a molecular signal, e.g., in concentration of a certain type of molecule, by signal transduction and how this variation can be detected based on the bacteria response, e.g., green fluorescent protein (GFP) illumination. We, first, examine the raw bacteria response both theoretically and experimentally for the one-to-one input-output relation, the noise, and the timing of the bacterial signal transduction. We, second, investigate statistically the sampling of the bacteria response as the received signal and the detection of the molecular signals. We consider one molecular source releasing finite duration concentration signals with a specific type of molecule, i.e., pulse-amplitude modulation (PAM), and a single bacterial receiver. The information is modulated onto the amount of the specific molecule in the concentration, which the bacteria cannot synthesize.

The challenge on which we concentrate in this chapter is the effect of the signal transduction on the sampling of the continuous output signal in MC systems with bacterial receivers. Of particular interest is the issue of the effect of the noise and the timing on the detection of the PAM molecular signal. The issues of the signal transduction in cells have been broadly reviewed and can be found in many books [44, Chapter 2],[80, Chapter 24],[81, Chapter 5],[82, Chapter 2]. The biochemical modeling of the signal transduction has been often studied in the context of reaction-rate equations (RRE). Different cases have been considered, among them: the bacterial signal transduction is modeled using a set of RRE to predict the bacteria response in a microfluidic platform [73], or simplification of an RRE model of signal transduction is utilized under quasi-equilibrium condition to design biological circuits with both analog and digital signaling functionalities [43]. Close to our work, [71] investigates performance of pulse-based on-off keying (OOK) modulation, i.e., single bit transmission per pulse, for bacterial receivers, where the binary one is represented by the input signal, and the binary zero is represented by the removal of the input from the channel. Therefore, detection of the multi-level input signals by bacterial signal transduction has been an open problem to date and has not been addressed yet to the best of our knowledge.

In this chapter, we consider the issues of the one-to-one input-ouput relation, noise, and timing in the context of detection via sampling the bacterial signal transduction at the

receiver. The transient variations in the noise and timing issues are tightly linked with the sampling of the raw bacteria response. The random jitter in the beginning, peak, and the ending of the bacteria response entails that the sampling of the bacteria response at a fixed instant will be exposed to additional distortion apart from the noise. The noise and the timing together are responsible for the distortion observed on the bacteria response. The following questions are sought to be investigated throughout the course of this work.

- When is the input-output relation one-to-one?
- How does the noise in the bacteria response vary with the time?
- What are the randomness effects on the timing of the response beginning, the peak instant, and the response ending?
- How should the raw bacteria response be sampled to minimize noise and timing effects for the detection of the input molecular signal?

The question regarding the sampling of the bacteria response for the detection of the input signal is principally significant, since the noise and the timing issues of the biological receivers have not been studied empirically for M-ary PAM molecular signals based on the experimental data. Theoretical analysis of biological transceivers has been performed based on RRE models in [43], where the biological noise and the timing issues are neglected. The robust design of biochemical signaling pathways with kinetic parameter uncertainties and external disturbances is studied based on control theory in [83, 84, 85]. However, the inference of information from the biochemical signal transduction has been an open debate. The provided performance analysis of the on-off keying modulation for bacterial receivers in [71] is only valid for binary PAM with transmission of a fixed level for 1 and transmission of no signal for 0. The sampling of the received signal from raw bacteria response is a subject yet to be studied for M-ary detection in the course of this work.

5.2 Bacterial Signal Transduction

The bacteria can generate a controlled response to an external molecular stimuli by signal transduction. For example, the gene sequence of bacteria can be modified such that output

protein production can be controlled in response to an input molecular signal [44, Chapter 2]. Here, we provide an overview of the biochemical phenomena of the bacterial response to external stimuli and how it makes the detection of the input signal possible.

To guide the detection of molecular signals, the basics of the input-output relation, e.g., input controlled synthesis of GFP, by bacteria must be first understood. Therefore, the bacterial signal transduction is analytically investigated focusing on the gene expression. In the following subsections, first, the specific model of the bacteria signal transduction is overviewed, and then, the input-output relation of the bacteria response is discussed along with the error analysis.

5.2.1 Model

The gene expression is regulated, e.g., activated, by the control of inducer molecules, which are supposed to be externally provided. To analytically study the bacteria response, we focus on the protein production as the *output signal*. The output signal is analyzed with respect to the externally provided inducer molecules, which is the *input signal*. Specifically, simplification of the RREs for the gene expression under the quasi steady-state and equilibrium approximations is considered for modeling [82, Chapter 2],[44, Chapter 2]. The detailed explanation for the modeling of gene expression and the simplifications of the RREs can be found in [82, Chapter 2],[44, Chapter 2]. Accordingly, the output signal is related to the input signal via the RRE given by

$$\frac{\partial y(t)}{\partial t} = \frac{\beta x^n}{\theta^n + x^n} - \alpha y(t) \tag{193}$$

where y is the output signal, x is the input signal level, θ is the activation coefficient. For example, when the expression is significantly activated when $x > \theta$, n determines steepness of the bacteria signal transduction, β is the empirical rate parameter defining the maximum expression level when $x \gg \theta$, and α is the degradation rate of the output signal y. Although this model is a simplified version of the bacterial signal transduction, it captures the input-output behavior of the bacteria response based on the gene expression.

To solve (193) for the step response with the zero initial conditions, i.e., the input is changed from zero to its desired level, Laplace transform of y, i.e., $Y(s) = \mathcal{L}\{y(t)\}$, is used,

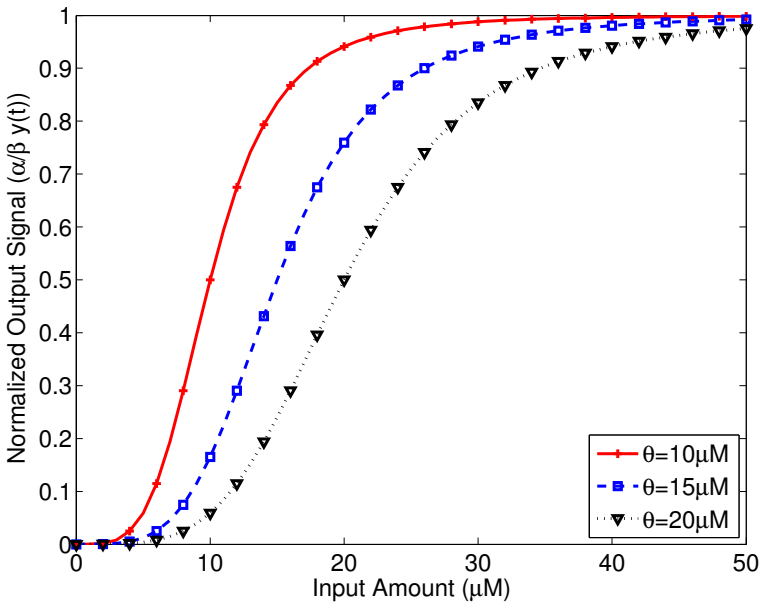

Figure 32: The input-output relation of the bacteria response based on (196). The activation coefficient θ is taken as 10, 15, and 20μM, $n = 4$, and the input amount varied from 0 to 50μM. The output signal is normalized by α/β.

and after partial fraction decomposition Y is found as

$$Y(s) = (\frac{\beta x^n}{\theta^n + x^n})\frac{1}{\alpha}(\frac{1}{s} - \frac{1}{s+\alpha}) \tag{194}$$

Finally, by taking the inverse Laplace transform of Y, i.e., $y(t) = \mathcal{L}^{-1}\{Y(s)\}$, y is found as

$$y(t) = \frac{\beta x^n}{\alpha(\theta^n + x^n)}(1 - e^{-\alpha t}) \tag{195}$$

5.2.2 Input-Output Relation and Error Analysis

To study the input-output relation, the normalized steady-state response of the bacteria is obtained using (195) as

$$\lim_{t\to\infty} \frac{\alpha}{\beta} y(t) = \frac{x^n}{\theta^n + x^n} \tag{196}$$

In Fig. 32, it is observed that the bacteria response is a one-to-one function of the input within an acceptable range. For example, when input is in the range from 15 to 25 μM for $\theta = 20\mu$M in Fig. 32, the output can even be approximated as a linear function of the input. As the input signal level kept increasing, the bacteria response is observed to be saturating

in Fig. 32. After saturation, the further increasing the input signal makes no difference on the output signal, i.e., input signal is indistinguishable based on the output signal. On the other hand, the output signal stays approximately zero for small input values, e.g., a few μM in Fig. 32. However, when the input signal range is kept both sufficiently large and below saturation level, a one-to-one input-output relation can be achieved.

We also analytically study the transient response of the bacteria to point out the impact of error in the maximum expression level β. To this end, the linear approximation of the $y(t)$ in (195) for $t = 0$ is used. First order Taylor series expansion of the exponential term, i.e., $e^{-\alpha t} \approx 1 - \alpha t$ for $\alpha t \approx 0$, gives

$$y(t) \approx \frac{x^n}{(\theta^n + x^n)} \beta t \tag{197}$$

where the term $x^n/(\theta^n + x^n)$ is constant with respect to time. We define $\hat{\beta} = \beta + \epsilon$ as the erroneous version of the maximum production level β, and ϵ incorporates the arbitrary error factor. Accordingly, the erroneous output $\hat{y}(t)$ can be rewritten by plugging $\hat{\beta}$ into (197) as

$$\begin{aligned} \hat{y}(t) =& \frac{x^n}{(\theta^n + x^n)} \beta t + \frac{x^n}{(\theta^n + x^n)} \epsilon t \\ =& y(t) + \frac{x^n}{(\theta^n + x^n)} \epsilon t \end{aligned} \tag{198}$$

The absolute error in the output, i.e., $|\hat{y}(t) - y(t)|$, is

$$|\hat{y}(t) - y(t)| = \frac{x^n}{(\theta^n + x^n)} \epsilon t \tag{199}$$

Note that the error term evolves with time. Accordingly, the error on the output is expected to increase during the ramp-up behavior of the bacteria response, i.e., the impact of erroneous protein production rate $\hat{\beta}$ on the output is more severe as time elapses. In the next section, we will investigate the bacteria signal transduction experimentally for PAM molecular signals.

5.3 Experimental Analysis of Bacteria Response

We perform tests with *Escherichia coli* (*E. coli*) bacteria strains on a microfluidic platform [71, 73]. The microfluidic platform provides control over the input molecular signal, i.e.,

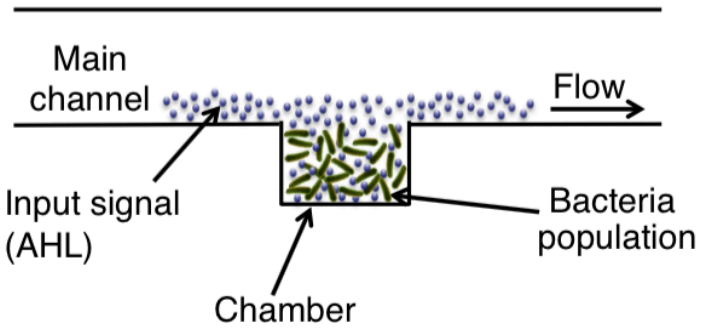

Figure 33: The chamber that is connected to the microfluidic channel and hosts the genetically-engineered bacteria.

the concentration pulse level and duration. Furthermore, the microfluidic platform hosts bacteria strains in chambers, where a microfluidic channel with flow carries the media composed of both the required nutrients and the input signal (Fig. 33).

The *E. coli* bacteria are genetically engineered to express genes from the autoinducer system of *Vibrio fischeri* (*V. fischeri*) bacteria and produce a variant of the green flouresence protein (GFP) under the presence of the autoinducer N-Acyl homoserine lactone (AHL) molecules. The produced GFP represents the bacteria response, i.e., output signal, and measured using the fluorescence microscopy. The autoinducer AHL molecules represent the input signal. Since the *E. coli* bacteria cannot encode the genes to produce AHL, the output signal can be utilized to detect the amplitude of the externally provided PAM molecular signal, i.e., the level of a finite duration AHL concentration pulse.

The specifics of the experimental system composed of the genetically engineered *E. coli* bacteria and the microfluidic platform were previously presented in [71, 73]. In the preceding discussions, we start with the study of the molecular signal propagation through the microfluidic channel. The negligible propagation delay, and invariance of the pulse amplitude and duration are pointed out for the multiple chambers hosting the bacteria. Then, the timing and the noise issues of the bacteria signal transduction are investigated based on measurements from the experimental platform. We provide a comprehensive look at the raw bacteria response for molecular signal detection and set the stage for statistical

Table 4: Concentration Pulse Prolongation through the Microfluidic Channel

	Distance	Delay	Prolongation Duration
Chamber 1	1.16 mm	0.0260 sec	0.0438 sec
Chamber 2	1.66 mm	0.0262 sec	0.0440 sec
Chamber 3	2.16 mm	0.0264 sec	0.0441 sec
Chamber 4	2.66 mm	0.0266 sec	0.0443 sec
Chamber 5	3.16 mm	0.0268 sec	0.0445 sec

comparison of the different strategies for sampling of the raw bacteria response.

5.3.1 Pulse Prolongation between Multiple Chambers

Having bacteria response from the different chambers attached to the same microfludic channel is useful to obtain multiple measurements and alleviate noise effects on the output signal for detection purposes. The microfluidic channel has a cross-section of 250μm x 10μm, and flow rate is 360μl/hr. The chambers are placed on the microfluidic channel with a constant separation distance, e.g., 0.5mm.

To obtain the prolongation of the concentration pulse until it reaches to the chamber k, we first calculate the molecular propagation delay ($\tau_{\text{delay}}^{(k)}$) until the chamber k as [1]

$$\tau_{\text{delay}}^{(k)} = \frac{l_1 + k \cdot l_{\text{sep}}}{u} \tag{200}$$

where l_1 is the distance of the closest chamber to the source, l_{sep} is the separation distance between chambers, and u is the area averaged flow velocity. The dispersion length ($l_{\text{disp}}^{(k)}$) until the chamber k is obtained using the diffusion equation as

$$l_{\text{disp}}^{(k)} = \sqrt{2D\tau_{\text{delay}}^{(k)}} \tag{201}$$

where D is the Taylor dispersion adjusted diffusion constant. Finally, the pulse prolongation duration τ_{prolong} is obtained as

$$\tau_{\text{prolong}}^{(k)} = \frac{l_{\text{disp}}^{(k)}}{u} \tag{202}$$

The molecular propagation delay and the pulse prolongation durations are tabulated in Table 4, which are in the range of a few 10ms. The calculated delay and prolongation

durations are much less compared to the required pulse duration to get a response from the bacteria, which is in the order of 10min [71, 73].

The separation distance between the source and the chambers is in the range of a few mm, and the considered pulse durations are in the range of a few 10min to get response from the bacteria in the experimental microfluidic platform. Accordingly, the input molecular signal can be taken invariant with respect to the propagation through the microfluidic channel. Therefore, the bacteria in different chambers are exposed to the same concentration pulse duration. Furthermore, the delay due to molecular propagation is also negligible since the bacteria response is in the hours scale [73, 43], which will be investigated in the following subsections.

5.3.2 Timing Analysis

The timing of the bacterial response behavior has importance to be able to efficiently sample and process the output signal for detection of the amplitude of the PAM molecular signal. The bacterial signal transduction involves ordered set of biochemical reactions. A set of biochemical reactions produces fluctuating number of intermediate molecules in short bursts at random time intervals, which need to reach an effective level to activate the next step in the signal transduction pathway. Therefore, there can be large differences in the time delay required for signal transduction, especially across the bacteria population [76]. Here, we investigate the timing specifically with respect to the response beginning, i.e., the instant that bacteria starts to produce the output signal, and the peak instant, i.e., the moment when the bacteria response reaches its peak, and the total response duration, i.e., the time elapses from the beginning of the bacteria response to the end.

The transient bacteria response behavior for PAM molecular signals of 15, 20, 22.5μM is shown in Fig. 34, which are averaged over 4, 7, and 5 experiments, respectively. The reason for the different number of measurements for the different concentration inputs is as follows. Once loaded, a few bacteria will settle in the trapping chambers. Not all chambers will have bacteria in them, which means the number of measurements can change from experiment to experiment. The molecular signals have a finite duration of 50min.

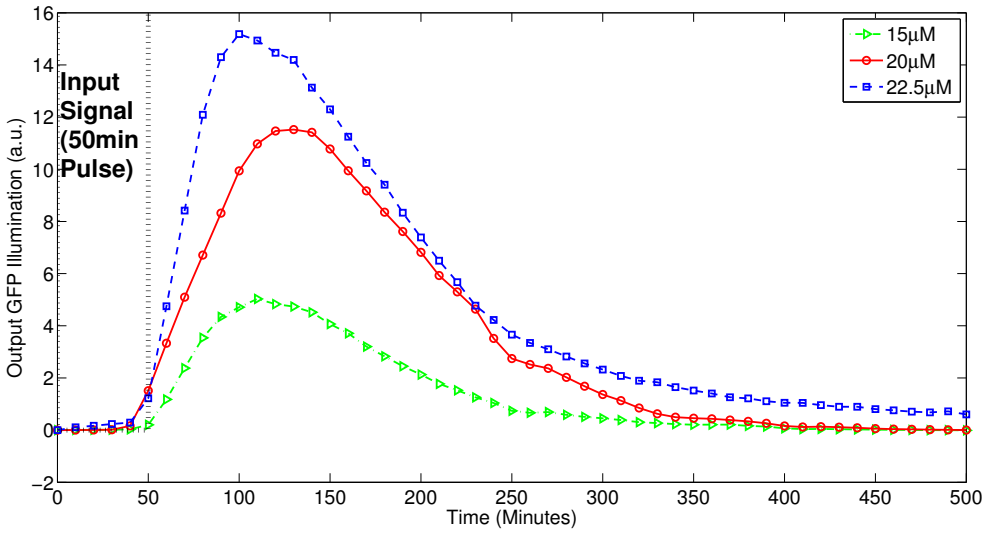

Figure 34: The transient response of the bacteria for different PAM molecular signal amplitudes.

The output signal is the relative fluorescence illumination. Fluorescent images were captured once every 10 min and post-processed using MATLAB. The intensity of the pixels within the bacteria chamber was averaged and the background fluorescence was subtracted, yielding the relative fluorescence (arbitrary units, or a.u.). Each run represents a single chamber that was imaged over time. Each data point for that run is calculated using the image processing mentioned above. The average for a concentration represents the averaging of all runs for that concentration. Therefore the standard deviations are the deviations between the individual chambers.

5.3.2.1 Bacteria Response Beginning

The difference of the response beginning and input molecular signal start ($t = 0$) times in Fig. 34 gives the bacteria response beginning delay. The response beginning delay is shown to be depending on the input molecular signal amplitude in Fig. 34. For 22.5μM and 20μM, the mean response beginning delay is shown to be converging and less than the one for 15μM. The input dependent beginning time of the bacteria response makes the sampling of the output signal at that particular instant challenging. Furthermore, since the

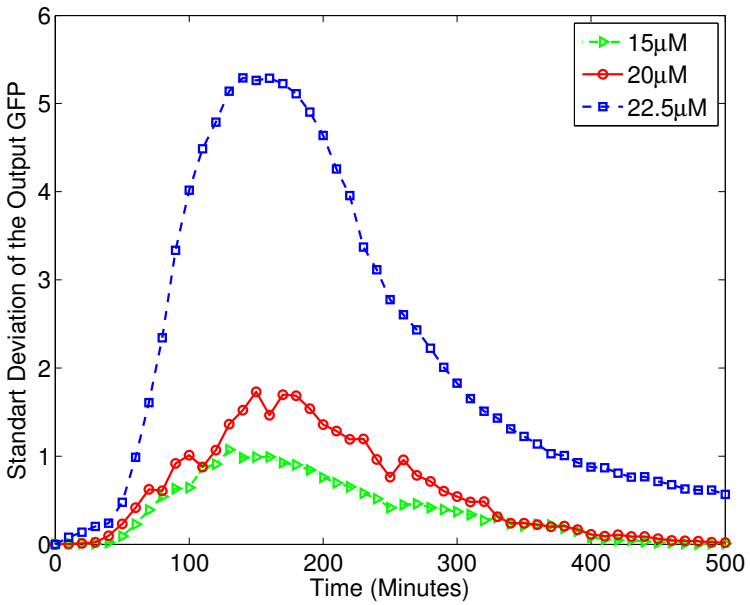

Figure 35: The standard deviation of the bacteria response with respect to time for different PAM molecular signal amplitudes.

response beginning delay is not always providing a one-to-one input-output relation as the input signal amplitude is further increased, it is not an efficient option for the detection of PAM molecular signals. For example, consider 2a.u. is selected as the reference to decide on the beginning of the bacteria response, the response reaches the output level of 2a.u. at the same instant for both input levels of 20μM to 22.5μM.

5.3.2.2 Peak Instant

The peak time of the bacteria response behavior is shown to be varying based on the amplitude of the input molecular signal in Fig. 34. Furthermore, the input dependance of the peak time is observed to be non-monotonic. Therefore, determination of a fixed time instant for sampling of the peak of the bacteria response is not trivial. For example, the peak instant for the input level 20μM is later than both 22.5μM and 15μM input levels. The experimental data in Fig. 34 suggest that the tight timing requirements on the sampling of the bacteria response is not favorable, since the bacteria response behavior is not synchronized to the input signal source.

5.3.2.3 Total Response Duration

Lastly, the total response duration, i.e., the time elapses form the beginning of the response to the ending, is observed in Fig. 34. The total response duration increases monotonically with input molecular signal amplitude. Furthermore, the total response duration is shown to be providing a one-to-one relation between the input and output in in Fig. 34. The use of the total response duration for sampling of the received signal and the detection of the input PAM molecular signal is further discussed in Section 5.4.

5.3.3 Transient Noise Analysis

In Fig. 34, the bacteria response behavior is identified to be composed of three regions, i.e., ramp-up region which takes place from beginning of the response to the peak, peak region where the response reaches its peak value, and the ramp-down region which takes place from the peak to the end of response. Here, the impact of noise on the bacteria response during ramp-up, peak, and ramp-down regions is studied. To this end, the standard deviation of the bacteria response behavior with respect to time for PAM molecular signals of 15, 20, and 22.5μM is shown in Fig. 35.

The higher standard deviation implies higher noise effect on the output signal. The standard deviation of the response is observed to be increasing as it reaches its peak in the ramp-up region. Then, the standard deviation of the response decays until the response ends. For different input levels, i.e., 15, 20, and 22.5μM, the same trend in the bacteria response behavior is observed in Fig. 35. Increasing noise from the response beginning to the peak in the ramp-up region conforms with the theoretical insights provided in Section 5.2.2. In (198), the absolute error in the output signal, i.e., $|\hat{y}(t) - y(t)|$, due to the error ϵ in the maximum protein production level β is identified to be increasing over time t. In the line with our theoretical investigations, it is shown experimentally that the increase in the output protein amount yields increased error contribution in the output, i.e., the error in the output signal is amplified as it reaches to the peak response value.

The study of the stochasticity in the gene expression has recently been a research field of interest [77, 86]. The impact of perturbation, i.e., stimulus, on the noise in the signal

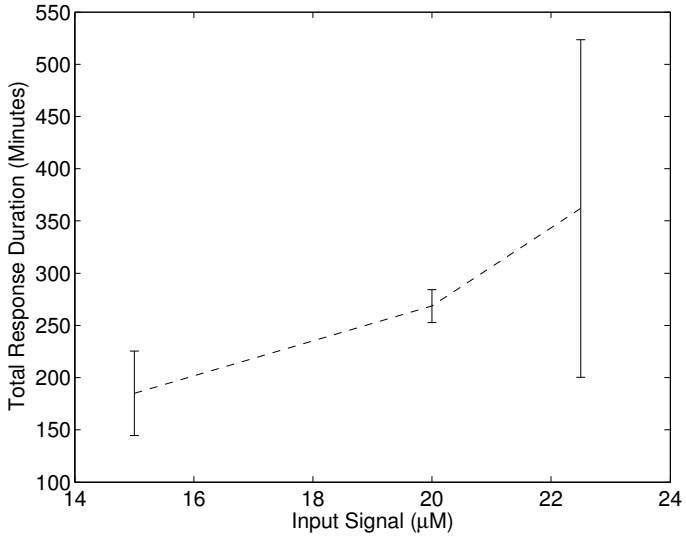

Figure 36: Input-output relation for the sampling of the received signal using total response duration.

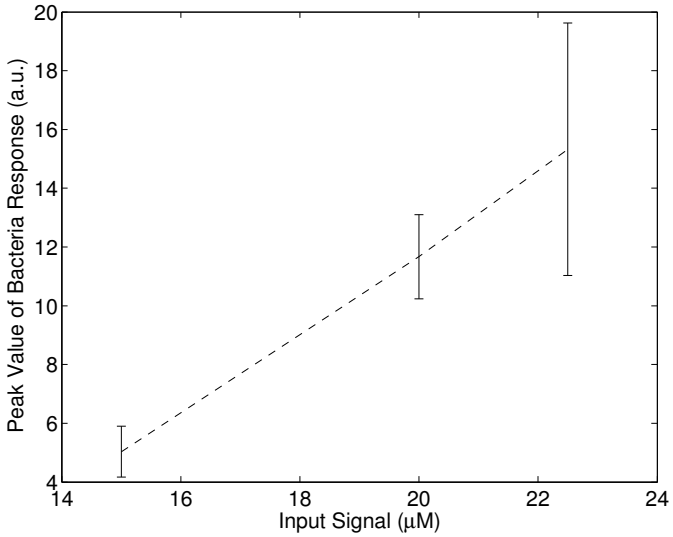

Figure 37: Input-output relation for the sampling of the received signal using the peak value.

transduction is investigated in [86], and directly proportional scaling of the noise variance with the protein abundance is reported, which are normalized with respect to the pre-stimulus values. Similarly, in Fig. 35, it is observed that the standard deviation of the bacteria response increases proportional to the magnitude of the response, i.e., standard

deviation increases as the input level is increased from 15μM to 22.5μM. Next, the different sampling strategies of the received signal are investigated to facilitate accurate and timely detection of the PAM molecular signals.

5.4 Sampling of the Received Signal based on the Bacterial Signal Transduction

So far, both analytical and experimental characterizations of the bacteria response are performed. However, the sampling of the received signal, i.e., mapping of the recorded raw bacteria response to the decision space, is missing such that the PAM input signal can be detected accurately. The input signal can be detected via applying thresholding on the received signal, i.e., comparing the received signal with the predefined thresholds for different input signal amplitudes. In this section, we extend our theoretical and experimental analyses in the former sections by proposing and comparing four different sampling strategies for the raw bacteria response, namely, the total response duration, the peak level of the response, the ramp-up slope, and the ramp-down slope.

5.4.1 Sampling Strategies for the Raw Bacteria Response

In the following, we study the sampling of the received signal ($r_k(t)$) from the raw bacteria response based on the total response duration ($r_{\text{total}}[k]$), the peak value ($r_{\text{peak}}[k]$), ramp-up slope ($r_{\text{up}}[k]$), and the ramp-down slope ($r_{\text{down}}[k]$). The sample sample index k indicates the kth transmission of the PAM molecular signal. It should be noted that while the received signal $r_k(t)$ from the bacteria response is a continuous function of t, the sampled responses $r_{\text{total}}[k]$, $r_{\text{peak}}[k]$, $r_{\text{up}}[k]$, $r_{\text{down}}[k]$ are discrete-time and a function with sample index k. The one-to-one input-output relation of the different sampling strategies is specifically investigated for the detection purposes.

To sample the raw bacteria response $r(t)$ for the total response duration $r_{\text{total}}[k]$, the duration between the instant when the response exceeds a predefined threshold η_{total} and

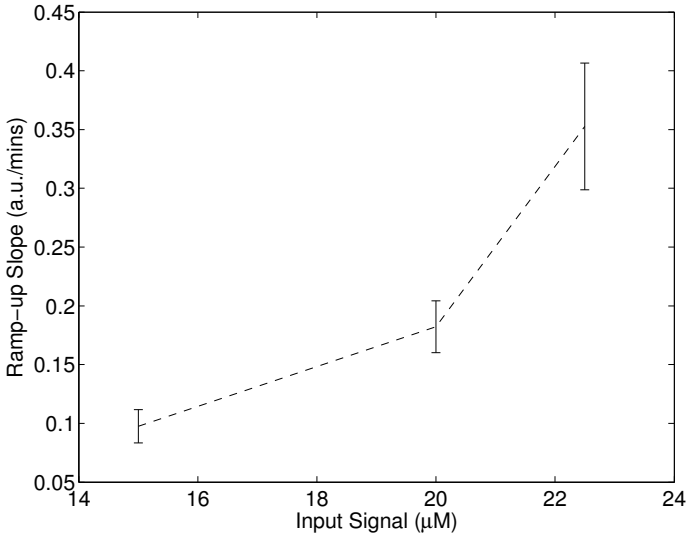

Figure 38: Input-output relation for the sampling of the received signal using the ramp-up slope.

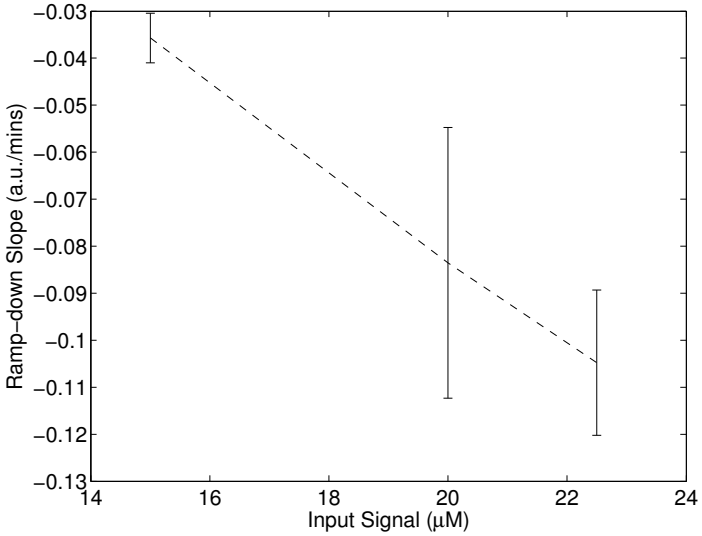

Figure 39: Input-output relation for the sampling of the received signal using ramp-down slope.

the instant the response goes below the threshold η_{total} is used, which is given by

$$\begin{aligned} r_{\text{total}}[k] = &\sup_t \operatorname*{argmin}_t |r_k(t) - \eta_{\text{total}}| \\ &- \inf_t \operatorname*{argmin}_t |r_k(t) - \eta_{\text{total}}| \end{aligned} \tag{203}$$

For evaluations, we set the threshold for output flouresence illumination to $\eta_{\text{total}} = 1$ a.u., i.e., the response beginning is taken as the instant when the measured bacteria response exceeds $\eta_{\text{total}} = 1$ a.u. and the response ending is taken as the instant when the measured bacteria response reduces below $\eta_{\text{total}} = 1$ a.u.. The peak value is taken as the maximum of the raw bacteria response as

$$r_{\text{peak}}[k] = \sup_t r_k(t) \tag{204}$$

Apart from the total response duration and the peak value, the slope of the ramp-up and the ramp-down behavior in the bacteria response can also be utilized to decide on the input signal level. Accordingly, ramp-up slope $r_{\text{up}}[k]$ can be calculated as

$$r_{\text{up}}[k] = \frac{r_k(t_2) - r_k(t_1)}{t_2 - t_1} \tag{205}$$

The ramp-up slope is calculated for the interval of $t_1 = 60$ and $t_2 = 70$ mins. The ramp-down slope is calculated as

$$r_{\text{down}}[k] = \frac{r_k(t_2) - r_k(t_1)}{t_2 - t_1} \tag{206}$$

where we use the interval of $t_1 = 160$ and $t_2 = 170$ mins for the evaluations.

The mean of the sampled received signal using total response duration, the peak value, the ramp-up slope, and the ramp-down slope are shown in Fig. 36, Fig. 37, Fig. 38, and Fig. 39, respectively, with respect to different input signal levels. It should be noted that the received signal is in different units for different sampling strategies, i.e., minutes for the total response duration, a.u. for the peak value, and a.u./mins for the slope of ramp-up and the ramp-down. It is observed that there is a one-to-one relation between the received signal and the input signal for all four sampling strategies of the received signal. Furthermore, the mean of the received signal monotonically increases as the input level increased for all four strategies of the received signal, which enables non-overlapping mapping of the received signal to the decision space. The input signal can be detected via comparison of the received signal with the predetermined thresholds based on the selected sampling strategy. However, each sampling strategy yields different statistical properties for the sampled received signal, i.e., mean and variance. Therefore, in the next subsection, we study the distinguishability of the sampled received signals to detect distinct input levels.

Table 5: p-values for the Sampling Strategies of the Received Signal

Sampling Scheme	**$15-20$ μM**	**$15-22.5$ μM**	**$20-22.5$ μM**
Total Response Duration	$2.11 \cdot 10^{-2}$	$6.91 \cdot 10^{-2}$	0.266
Peak Value	$5.68 \cdot 10^{-6}$	$4.9 \cdot 10^{-3}$	0.131
Ramp-up slope	$3.41 \cdot 10^{-5}$	$2.35 \cdot 10^{-4}$	$1.17 \cdot 10^{-3}$
Ramp-down slope	$4.1 \cdot 10^{-3}$	$2.11 \cdot 10^{-4}$	0.131

5.4.2 Statistical Distinguishability

Here, the detection performance of the four sampling strategies for the received signal are statistically compared. We utilize the t-test with unequal variances [87, Chapter 4], where obtained samples from the raw bacteria response are assumed to be normally distributed. The probability that the obtained two samples are belonging to the same input level, i.e., p-value, is specifically studied. The smaller the p-value, the more **unlikely** the compared samples are belonging to the same input signal level. In the following, the obtained p-values are examined for the decision between the different input level pairs.

The p-values are tabulated in Table 5. For decision between 15μM and 20μM, the lowest p-values are provided by peak value and the ramp-up slope, i.e., $5.68 \cdot 10^{-6}$ and $3.41 \cdot 10^{-5}$, respectively, where the later one is 6 times larger than the former. For the decision between 15μM and 22.5μM, the lowest p-value is provided by the ramp-up and the ramp-down slope, i.e., $2.35 \cdot 10^{-4}$ where the p-value by sampling the peak is about 20 times larger than them. For the decision between 20μM and 22.5μM, the lowest p-value, i.e., $1.17 \cdot 10^{-3}$, is provided by the ramp-up slope, where the other interpretations of the bacteria response have an approximately 100 times larger p-value. On the other hand, the total response duration provides the worst performance for detection purposes as a sampling strategy of the received signal based on the p-value results.

While the ramp-up slope and the peak value provides a close p-value for the decision between 15μM and 20μM, the p-value of the input pulse pairs is further amplified as the input levels are increased, i.e., the peak value has the third smallest p-value for the other input combinations. Meanwhile, the ramp-up slope performs either the lowest or the second

Table 6: Mean (μ) of the Sampled Bacteria Response

Sampling Scheme (unit)	**15μM**	**20μM**	**22.5μM**
Total Response Duration (mins)	185	268	362
Peak Value (a.u.)	5.03	11.66	15.32
Ramp-up Slope (a.u./mins)	0.097	0.18	0.35
Ramp-down Slope (a.u./mins)	-0.035	-0.083	-0.1

Table 7: Variance (σ^2) of the Sampled Bacteria Response

Sampling Scheme (unit^2)	**15μM**	**20μM**	**22.5μM**
Total Response Duration (mins^2)	1630	247	26100
Peak Value (a.u.^{2})	0.75	2.04	18.48
Ramp-up Slope (a.u.^{2}/mins^2)	0.00019	0.00048	0.0029
Ramp-down Slope (a.u.^{2}/mins^2)	0.000027	0.00082	0.00023

lowest p-value.

Based on the statistical analysis of the received signal interpretations in Table 5 and the experimental transient analysis of standard deviation in Fig. 35, as well as theoretical insights provided in (198), the ramp-up slope is selected to be further investigated for the sampling of the received signal among others in Section 5.5.

5.4.3 Probability of Error for Detection of Binary and 3-ary PAM

The probability of error for the PAM molecular signals is studied with respect to the four sampling schemes. Each different input pulse level $\mathcal{H}_i$ has a specified different mean sampled received signal level μ_i. We assume the sampled received signal for each different $\mathcal{H}_i$ is corrupted by Gaussian noise, i.e.,

$$p(r|\mathcal{H}_i) \sim \mathcal{N}(\mu_i, \sigma_i^2) \tag{207}$$

where index k is dropped from the sampled bacteria response r for the ease of notation, and σ_i^2 is the variance of the sampled response. The obtained μ_i and σ_i^2 values from experimental measurements are given in Table 6 and Table 7, respectively, for the four sampling schemes.

In the following, we, first, give the formulation of the probability of error for the detection of the binary and the 3-ary PAM molecular signals [88, Chapter 2]. Then, we investigate

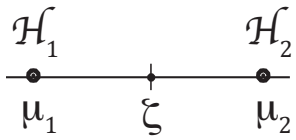

(a)

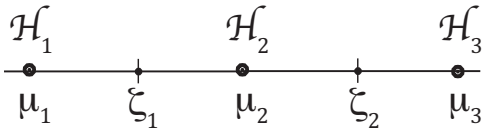

(b)

Figure 40: The signal points for binary and 3-ary PAM signals in (a) and (b), respectively.

the detection performance of the four sampling strategies based on the data obtained from experimental measurements for the bacterial signal transduction.

5.4.3.1 Binary Transmission

For the binary transmission case, only two different signal levels, i.e., $\mathcal{H}_1$ and $\mathcal{H}_2$, are considered to be transmitted. During the formulation, the corresponding signal level to $\mathcal{H}_1$ is taken to be lower than the one for $\mathcal{H}_2$. In the line with signal levels, the bacteria response corresponding to $\mathcal{H}_1$ is lower than $\mathcal{H}_2$, e.g., consider the bacteria response for 15μM and 20μM in Fig. 34. In Fig. 40(a), the signal points for the binary PAM signals is shown.

We should note again that r is a scalar value and corresponds to obtained received signal via sampling the bacteria response using one of the four sampling strategies. The probability distribution of the received signal for $\mathcal{H}_1$ is as

$$p(r|\mathcal{H}_1) = \frac{1}{\sqrt{2\pi\sigma_1^2}} e^{-\frac{(r-\mu_1)^2}{2\sigma_1^2}} \tag{208}$$

and for the transmission signal level corresponding to $\mathcal{H}_2$, the distribution of the received signal is given as

$$p(r|\mathcal{H}_2) = \frac{1}{\sqrt{2\pi\sigma_2^2}} e^{-\frac{(r-\mu_2)^2}{2\sigma_2^2}} \tag{209}$$

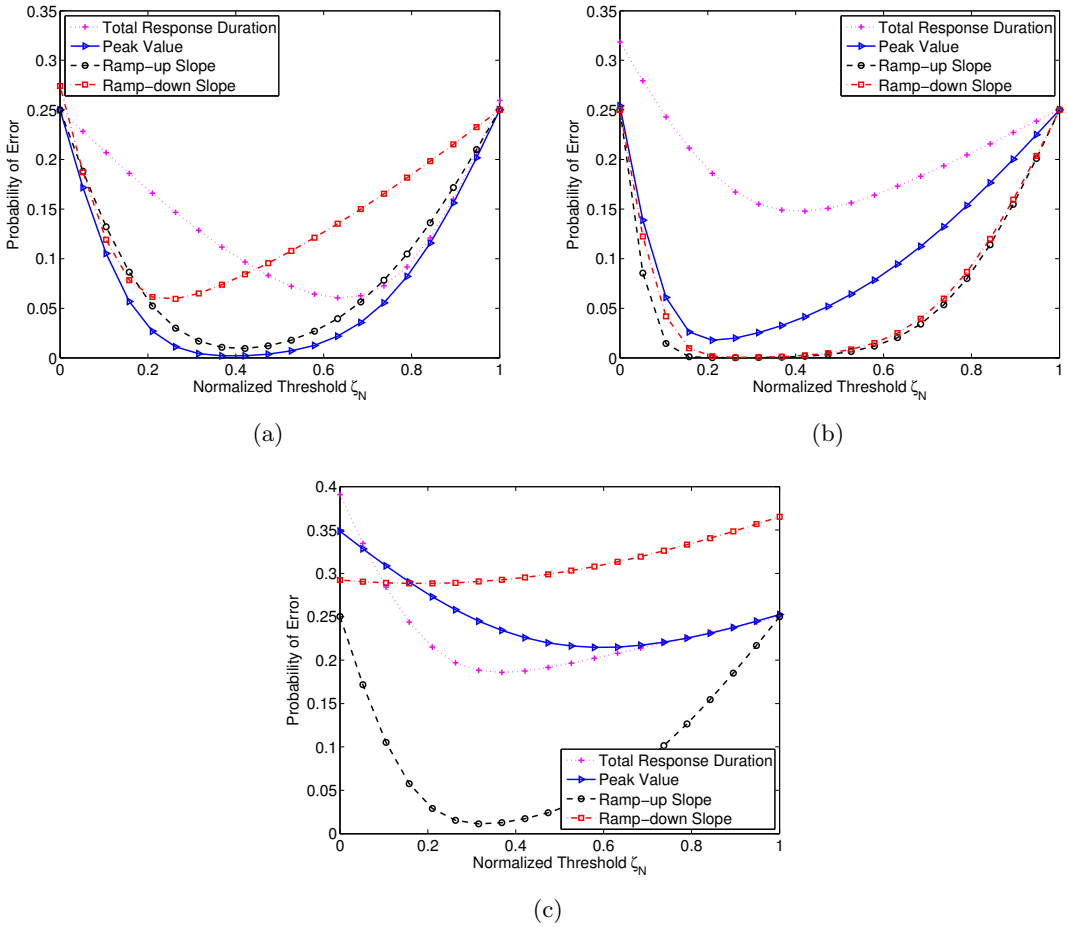

Figure 41: Comparison of the sampling schemes with respect to probability of error for binary PAM. Input pairs of $15-20\mu$M (a), $20-22.5\mu$M (b), and $20-22.5\mu$M (c) with 50 mins pulse width are considered. Threshold ζ is varied. To present results for different sampling schemes in the same plot, the threshold ζ is normalized using $\zeta_{\mathrm{N}} = (\zeta - \mu_1)/(\mu_2 - \mu_1)$.

The probability of error for $\mathcal{H}_1$, i.e., the received signal is greater than the detection threshold ζ, is given by

$$P(r > \zeta|\mathcal{H}_1) = \int_{\zeta}^{\infty} p(r|\mathcal{H}_1) \tag{210}$$

and similarly the probability of error for $\mathcal{H}_2$ is given by

$$P(r < \zeta|\mathcal{H}_2) = \int_{-\infty}^{\zeta} p(r|\mathcal{H}_2) \tag{211}$$

The transmission of both signal levels are taken to be equally likely, and hence, the probability of error for binary PAM is obtained using (210) and (211) by

$$P_b = P(r > \zeta|\mathcal{H}_1) + P(r < \zeta|\mathcal{H}_2) \tag{212}$$

5.4.3.2 3-ary Transmission

In 3-ary PAM, the transmission of 3 different pulse amplitudes, i.e., $\mathcal{H}_1$, $\mathcal{H}_2$, and $\mathcal{H}_3$, are considered. We assume corresponding bacteria responses to $\mathcal{H}_1$, $\mathcal{H}_2$, and $\mathcal{H}_3$ are sorted in the ascending order. In Fig. 40(b), signal points for the 3-ary PAM is shown. For the 3-ary transmission case, i.e., three transmission levels, the formulation of the $p(r|\mathcal{H}_1)$ and $p(r|\mathcal{H}_2)$ follows (208) and (209) in the binary case. For $\mathcal{H}_3$, $p(r|\mathcal{H}_3)$ is as

$$p(r|\mathcal{H}_3) = \frac{1}{\sqrt{2\pi\sigma_3^2}} e^{-\frac{(r-\mu_3)^2}{2\sigma_3^2}} \tag{213}$$

The probability of error for $\mathcal{H}_1$, i.e., $P(r > \zeta_1|\mathcal{H}_1)$ is

$$P(r > \zeta_1|\mathcal{H}_1) = \int_{\zeta_1}^{\infty} p(r|\mathcal{H}_1) \tag{214}$$

The probability of error for $\mathcal{H}_2$, i.e., $P(r < \zeta_1 \cup r > \zeta_2|\mathcal{H}_2)$ is given as

$$P(r < \zeta_1 \cup r > \zeta_2|\mathcal{H}_2) = \int_{-\infty}^{\zeta_1} p(r|\mathcal{H}_2) + \int_{\zeta_2}^{\infty} p(r|\mathcal{H}_2) \tag{215}$$

Lastly, the probability of error for $\mathcal{H}_3$, i.e., $P(r < \zeta_2|\mathcal{H}_3)$, is as

$$P(r < \zeta_2|\mathcal{H}_3) = \int_{-\infty}^{\zeta_2} p(r|\mathcal{H}_3) \tag{216}$$

With equal transmission probability for all three levels, probability of error for 3-ary PAM is obtained using (214), (215) and (216) as

$$\begin{aligned} P_b =& \frac{1}{3} P(r > \zeta_1|\mathcal{H}_1) + \frac{1}{3} P(r < \zeta_1 \cup r > \zeta_2|\mathcal{H}_2) \\ &+ \frac{1}{3} P(r < \zeta_2|\mathcal{H}_3) \end{aligned} \tag{217}$$

In the following, we present results on probability of error for both binary and 3-ary PAM cases.

5.4.3.3 Discussion

In Fig. 41, the probability of error is evaluated for the binary PAM. The threshold ζ to decide between different input levels $\mathcal{H}_1$ and $\mathcal{H}_2$ is varied between the corresponding specified mean sampled response levels μ_1 and μ_2. Since the threshold ζ has a different unit and scale for each sampling scheme, it is normalized to the interval $[0, 1]$.

Table 8: Minimum Probability of Error for Binary PAM

Sampling Scheme	**$15-20$ μM**	**$15-22.5$ μM**	**$20-22.5$ μM**
Total Response Duration	0.0605	0.1478	0.1859
Peak Value	0.002	0.0178	0.2147
Ramp-up Slope	0.0095	0.0001	0.0114
Ramp-down Slope	0.0595	0.0004	0.2885

For the input level pairs of $15-20\mu$M, $15-22.5\mu$M, and $20-22.5\mu$M, the sampling based on the peak value and the ramp-up slope is shown to be achieving lower error probability than the sampling based on the ramp-down slope and the total response duration in Fig. 41(a), Fig. 41(b), and Fig. 41(c), respectively. The minimum probability of error achieved by each sampling scheme for the binary PAM is given in Table 8. For the input level pair of $15-20\mu$M, sampling based on the peak value achieves the lowest probability of error, i.e., 0.002, whereas the probability of error for sampling based on ramp-up slope is 0.0095. For the input pairs of $15-22.5\mu$M and $20-22.5\mu$M, the minimum probability of error is achieved by sampling based on ramp-up slope, which outperforms peak value sampling by 100x and 10x in terms of probability of error, respectively. Additionally, the selection of proper threshold ζ is essential to minimize the probability of error as observed in Fig. 41.

For 3-ary PAM, all experimentally tested input levels, i.e., 15μM, 20μM, and 22.5μM are allowed to be transmitted. The results on error probability for the four sampling schemes are presented with respect to the normalized threshold ζ_1, which is to decide between $\mathcal{H}_1$ and $\mathcal{H}_2$, and normalized threshold ζ_2, which is to decide between $\mathcal{H}_2$ and $\mathcal{H}_3$, in Fig. 42(a), and Fig. 42(b), respectively. The sampling based on the ramp-up slope is shown to be achieving the lowest error probability compared to the other sampling schemes for the all evaluated choices for the detection thresholds ζ_1 and ζ_2 in Fig. 42(a) and Fig. 42 (b), respectively. The minimum probability of error achieved by each sampling scheme for the 3-ary PAM is given in Table 9. The sampling via ramp-up slope achieves more than 5x and 10x improvement in the probability of error over the sampling based on peak value for both studies with respect to the detection thresholds ζ_1 and ζ_2, respectively. The proper selection

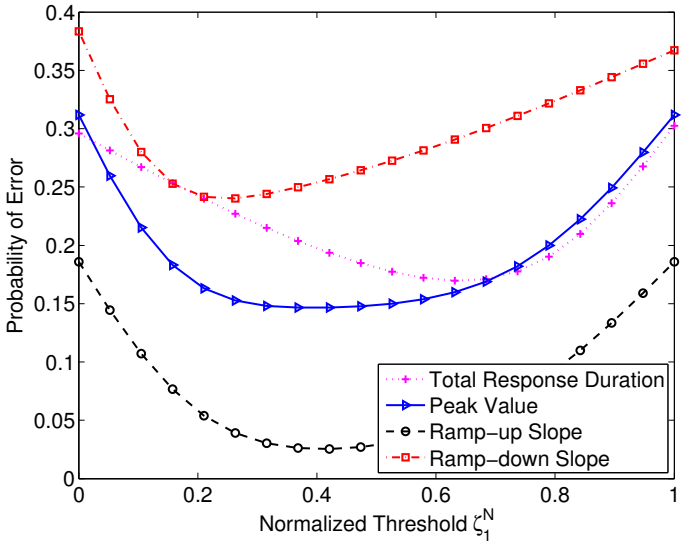

(a)

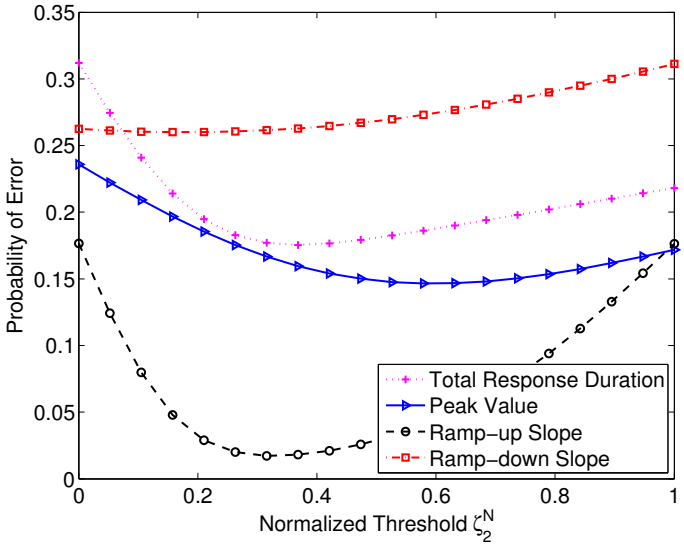

(b)

Figure 42: Comparison of the sampling schemes with respect to probability of error for 3-ary PAM with 50 mins pulse width. Thresholds ζ_1 and ζ_2 are varied. To present results for different sampling schemes in the same plot, the thresholds ζ_1 and ζ_2 are normalized using $\zeta_1^{\mathrm{N}} = (\zeta_1 - \mu_1)/(\mu_2 - \mu_1)$ and $\zeta_2^{\mathrm{N}} = (\zeta_2 - \mu_2)/(\mu_3 - \mu_2)$, respectively.

of the detection thresholds ζ_1 and ζ_2 is essential to optimize the detection performance.

5.4.4 Response Observation Duration

The required observation duration on the bacteria response is discussed in the descending order for the four sampling strategies of the received signal. To determine the total response

Table 9: Minimum Probability of Error for 3-ary PAM

Sampling Scheme	ζ_1 varied, $\zeta_2^{\mathrm{N}} = 0.5$	ζ_2 varied, $\zeta_1^{\mathrm{N}} = 0.5$
Total Response Duration	0.1696	0.1755
Peak Value	0.1466	0.1465
Ramp-up Slope	0.0254	0.0172
Ramp-down Slope	0.2403	0.26

duration, bacteria response needs to end, thus, it has the longest observation duration with respect to the other interpretations of the received signal. The ramp-down slope requires the bacteria response to be in the decay behavior, hence, it requires less observation duration than the total response. However, the required observation duration is still longer than the one for peak value. To sample the peak value, the bacteria response needs to reach its maximum value which happens before the decay behavior but later than the ramp-up behavior. The ramp-up slope provides the earliest opportunity for instantaneous detection purposes, since the bacteria response enters first to this behavior after it starts. The required observation durations for the different sampling strategies of the received signal are summarized as

$$\tau_{\mathrm{total-response}} > \tau_{\mathrm{ramp-down}} > \tau_{\mathrm{peak}} > \tau_{\mathrm{ramp-up}} \tag{218}$$

where $\tau_{\mathrm{total-response}}$, $\tau_{\mathrm{ramp-down}}$, τ_{peak}, and $\tau_{\mathrm{ramp-up}}$ represent the required observation duration for the received signal sampling based on the total response duration, the ramp-down slope, the peak value, and the ramp-up slope, respectively. Next, we further investigate the detection of molecular signals using the ramp-up slope.

5.5 Detection of Molecular Signals via Ramp-up Slope of the Bacterial Signal Transduction

During the course of this work, we have found the following answers to the questions listed in the introduction section through both analytical and experimental investigation:

- The input-output relation of the signal transduction is one-to-one for sufficiently small input ranges. (Section 5.2.2).

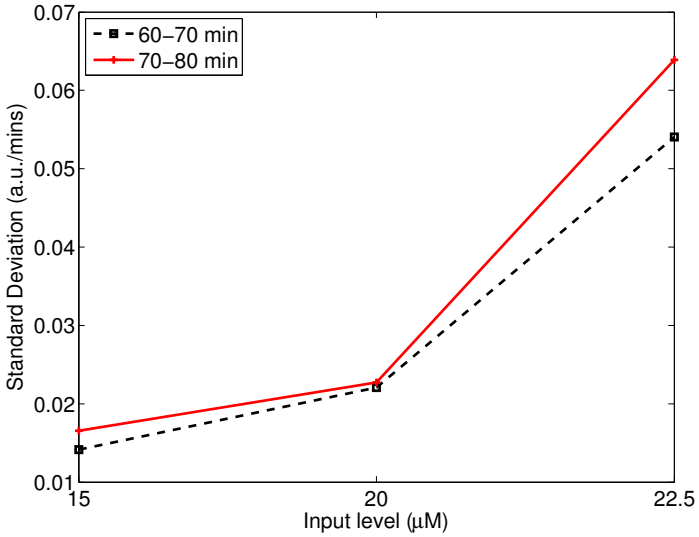

Figure 43: Standard deviation of ramp-up slope with respect to input level for different time interval selections.

- The noise in the bacteria response scales directly proportional to the time elapses until the response reaches peak. Then, the noise reduces as the bacteria response decays (Section 5.2.2 and Section 5.3.3).

- The time delay for the response beginning, the peak instant, and the response ending are shown to be randomly varying (Section 5.3.2).

- The sampling based on the ramp-up slope is shown to be favorable according to the comparisons based on the p-values and the probability of error for the detection of binary and 3-ary PAM molecular signals (Section 5.4.2 and Section 5.4.3).

Motivated by the results of comparisons based on p-test and probability of error, we further study the detection of molecular signals by sampling the raw bacteria response via the ramp-up slope.

5.5.1 Decision

We consider the use of t-test for the decision on whether a specific input level $\mathcal{H}_i$ is transmitted. μ_i corresponds to the mean of the sampled received signal for each input pulse level

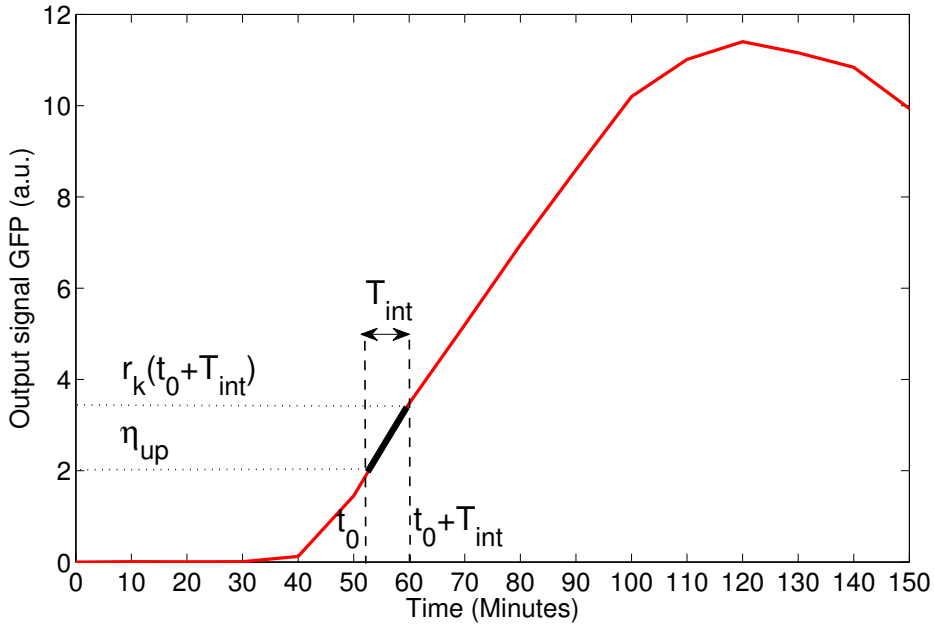

Figure 44: The sampling of the raw bacteria response for the ramp-up slope $r_{\text{up}}[k]$ (the raw bacteria response curve is taken from an individual experiment for 20μM input).

$\mathcal{H}_i$. Considering multiple repeated experiments, the t-statistic ξ is given by

$$\xi_i = \frac{\overline{r}_{\text{up}} - \mu_i}{s/\sqrt{K}} \tag{219}$$

where K is the number of samples, $\overline{x}$ is the sample mean given by

$$\overline{r}_{\text{up}} = \frac{1}{K}\sum_{k=1}^{K} r_{\text{up}}[k] \tag{220}$$

and s is the sample standard deviation given by

$$s = \sqrt{\frac{1}{K}\sum_{k=1}^{K}(r_{\text{up}}[k] - \mu_i)^2} \tag{221}$$

The signal level $\mathcal{H}_i$ corresponding to the μ_i providing the minimum t-statistic ξ_i is decided as the input molecular signal.

5.5.2 Time Interval Selection for Ramp-up Slope

The selection of time interval in bacteria response for the calculation of the mean ramp-up slope is of critical importance. In Fig. 34, it is observed that the instants when bacteria

1: **if** $r_k(t) == \eta_{\text{up}}$ **then**
2: $t_0 =$ current time
3: **while** $t \leq t + T_{\text{int}}$ **do**
4: **if** $t = T_{\text{int}}$ **then**
5: $r_{\text{up}}[k] = \frac{r_k(t_0+T_{\text{int}})-\eta_{\text{up}}}{T_{\text{int}}}$
6: **end if**
7: **end while**
8: **end if**

Figure 45: Non-coherent calculation of the ramp-up slope $r_{\text{up}}[k]$.

response enters and leaves ramp-up region vary based on input level. Furthermore, based on the results presented in Fig. 35, standard deviation of the bacteria response increases with the evolving time during the ramp-up behavior. Moreover, in Section 5.2.2, it is shown analytically that the error is amplified with the evolving time during the ramp-up behavior. This suggests the earlier calculation of the ramp-up slope μ_i during the ramp-up behavior.

For different intervals, the standard deviation of the ramp-up slope is studied in Fig. 43. T_{int} is taken as 10 min, and the ramp-up slope is calculated for 60-70 min, and 70-80 min. It is shown that the standard deviation of the ramp-up slope is less for earlier intervals of bacteria response, e.g., $60-70$min interval has a lower standard deviation compared to the $70-80$min interval.

5.5.3 Non-coherent Sampling for the Ramp-up Slope

While earliest calculation of the ramp-up slope provides better prediction of the input level, the randomness in entering the ramp-up behavior yield strict timing requirements for detection impractical. Therefore, a non-coherent scheme for detection of molecular signals via bacteria response is needed to mitigate delay uncertainty and eliminate timing requirements at the receiver. To remove timing requirement for sampling, a differential detection scheme can be utilized, which is illustrated in Fig. 44. A sufficiently large threshold level η_{up}, for which all different input levels i enter to the ramp-up region, can be determined, and the instant t_0 bacteria response reaches $r_{\text{up}}(t_0) = \eta_{\text{up}}$ level can be recorded. After waiting for the interval duration T_{int}, another sample can be taken from the response $r_k(t_0 + T_{\text{int}})$. Accordingly, the ramp-up slope can be calculated, and t-test can be applied to detect the transmitted signal level. The proposed algorithm is summarized in Fig. 45.

5.5.4 A Linear Noisy Model of Bacterial Receiver

A linear channel model can be solved directly, and the methodologies developed to assess performance of linear communication systems can also be applicable for MC with bacterial receivers, e.g., detection and estimation theory and information theory for linear channels [88, 68]. Here, a linear noisy model of bacterial receiver is proposed which aims to capture the noise in the ramp-up slope and in the timing of the bacterial signal transduction.

For finite duration pulse-amplitude modulated concentration signals, $r_{\text{up}}[k]$ is unique for different transmitted signal levels. Both experimental and theoretical evidences are provided in this section for the one-to-one input-output relation of bacterial signal transduction.

Based on the ramp-up slope calculation algorithm given in (45), the bacteria response in the ramp-up region can be expressed as

$$r_{\text{up}}[k] = \frac{r_k(t_0 + T_{\text{int}}) - \eta_{\text{up}}}{T_{\text{int}}} \tag{222}$$

To incorporate the randomness effects into the bacteria response, the noise terms w_{up} and w_{int} are added to model. The linear noisy model of $r_k(t_0 + T_{\text{int}})$ is obtained as

$$r_k(t_0 + T_{\text{int}}) = [r_{\text{up}}[k] + w_{\text{up}}][T_{\text{int}} + w_{\text{int}}] + \eta_{\text{up}} \tag{223}$$

where w_{up} is the noise in the ramp-up slope $r_{\text{up}}[k]$ and w_{int} is the noise in the timing of the bacterial signal transduction.

5.6 Highlights

In this work, detection of discrete messages with a bacteria-based molecular receiver is investigated for molecular communication over microfluidic channels. Discrete messages are represented by the amplitude of the transmitted finite-duration concentration pulses. Engineered bacteria transduce the concentration pulse to green fluorescent protein, which can be observed using fluorescence microscopy. Detection of the transmitted message is performed based on the fluorescence microscopy of the bacteria response.

There were several challenges on which we specifically focused during the course of this work. To detect the transmitted message, given fixed pulse duration, a unique response

level (one-to-one input-output relation) is required. Imperfections (noise effects) which are present in the bacteria response level as well as timing issues (randomly varying response beginning, peak instant, and response ending) make it difficult to distinguish which message was transmitted. The presence of noise effects have a detrimental effect on the detection performance and should be minimized. Furthermore, bacteria response can take several hours to complete. In some applications of synthetic biology, the timely communication of the transmitted message can be of great importance, such as in the case of real-time monitoring of chemical changes. Therefore, instead of waiting for the bacteria response to finish, it can be critical to decide on the transmitted signal as early as possible or within a delay constraint.

The goal of the molecular receiver (see Fig. 2) is to determine from a noise perturbed signal which of the finite set of discrete messages had been sent by the transmitter. To enable detection of the transmitted discrete messages, efficient sampling of bacteria response is studied addressing 1) the one-to-one input-output relation requirement, 2) noise on the sampled response, and 3) required response observation duration for detection.

Four different sampling schemes are defined: 1) total response duration, 2) peak value, 3) ramp-up slope, 4) ramp-down slope. The one-to-one relation between the transmitted discrete messages (pulse amplitudes) and the bacteria response are shown for all sampling schemes. The efficiency of each sampling scheme is assessed with respect to the impact of noise on the detection performance and the required bacteria response observation duration. Sampling of the ramp-up slope is shown to be less vulnerable to noise and providing the most accurate detection performance among others. Sampling of ramp-up slope also requires the minimum bacteria response observation duration.

The results of this study motivate the use of ramp-up slope of the bacteria response as an efficient sampling scheme for the detection of the transmitted discrete messages. To facilitate the detection while bacteria response is being observed, an algorithm is also devised for the calculation of the ramp-up slope.

CHAPTER VI

CONCLUSION

In this thesis, communication channel models are developed and performance analyses are performed for microfluidic molecular communication systems, as well as bacteria-based molecular receivers. The following four areas have been investigated under this research and each of them is described in the following subsections:

1. System-Theoretic Microfluidic Channel Modeling and FIR Filter Design
2. End-to-End Propagation Noise and Memory Analysis for Microfluidic Channels
3. Interference Modeling and Capacity Analysis for Microfluidic Multiple Access Channel
4. Detection of PAM Molecular Signals with Bacterial Receivers on a Microfluidic Channel

6.1 Research Contributions

6.1.1 System-Theoretic Microfluidic Channel Modeling and FIR Filter Design

In this research direction, system-theoretic analysis and least-squares design of microfluidic channels are performed for Flow-induced Molecular Communications (FMC). The objective of this work is the development of end-to-end concentration propagation model based on microfluidic channel configurations, i.e., building blocks of FMC. To the best of our knowledge, this is the first study of concentration propagation in FMC. Furthermore, using the developed system-theoretic end-to-end model for building blocks of FMC, the Finite Impulse Response (FIR) filters are devised. Specifically, the least-squares method is used to map channel parameters to the desired FIR filter frequency response. A parallel connection of microfluidic channels scheme is proposed similar to tapped delay lines. The transfer functions of straight and turning channels are investigated for various length and turning angles, and example design of microfluidic channels are presented for band-pass and band-stop filtering of concentration signal.

6.1.2 End-to-End Propagation Noise and Memory Analysis for Microfluidic Channels

In this work, the propagation noise and memory analyses are performed for Flow-induced Molecular Communications (FMC). The objective of this work is the investigation of end-to-end propagation noise based on the chamber and microfluidic channel parameters. To the best of our knowledge, this is the first study of propagation noise in FMC. Motivated by the flat spectral density of the noise, an Additive White Gaussian Noise (AWGN) model is proposed for FMC. Furthermore, we model the molecular memory due to the inter-diffusion of transmitted concentration signals and show the effect of the memory on the propagation noise. We also investigate the signal propagation at the chambers, and the noise spectrum for various chambers, the microfluidic channel, and the transmission parameters.

The derived mathematical framework provides a complete analysis of the propagation characteristics for the combination of different mass transport phenomenons, i.e., diffusion in the chambers and convection in the microfluidic channels. Using developed building blocks for molecular noise, spectral density of the end-to-end propagation noise for any MC architecture can be analyzed. Accordingly, suitable noise model for the transmission frequency range of interest can be developed.

The memory effect is investigated from both impact of different molecular transport phenomenons and impact on molecular noise perspectives. Necessary conditions for memoryless MC are defined for both diffusion-based and convection-based molecular transport. Developed memory analysis for proposed microfluidic MC architecture can be applied to any combination of the molecular transport mechanisms as well.

Therefore, our analysis is universal, and independent of the microfluidic MC architecture. The developed linear end-to-end channel model sets the stage for capacity analysis, and design of complex modulation, coding, and receiver schemes for MC over microfluidic channels. On the other hand, to model generation of molecular signal and distortion effects on it, analysis and design biological transceivers are imperative as well.

6.1.3 Interference Modeling and Capacity Analysis for Microfluidic Multiple Access Channel

In this work, the interference modeling and capacity analysis for the microfluidic MC channel are presented. The impact of interferer signal on the MC capacity is studied for single and multiple interferer cases. The MC capacity is shown to be severely limited under interference, which requires development of practical interference-aware communication schemes considering the capabilities of the biological molecular transmitters and receivers. Furthermore, three different microfluidic interference channel configurations are introduced based on the flow velocity and the receiver placement on the microfluidic channel, namely, the microfluidic both-sided interference configuration, the microfluidic one-sided interference configuration, and the microfluidic interference-free configuration.

MC over microfluidic channels can enable in parallel sensing and processing of chemicals by molecular transmitters, and these transmitters can engage in multi-stage chemical reactions with the receivers via sending their message molecules over a common microfluidic channel. For large-scale integration of chemical analysis systems on a microfluidic chip, the provided information-theoretic analysis and the capacity expressions for the MIC can be utilized to analyze the throughput of the chip, which can lead to improvement in efficiency and optimization of the design. The modeling of the molecular transmitter and receivers is still an open research problem which can help to design a complete microfluidic MC system. To distinguish the designated signal from interference, the development of modulation and detection schemes based on constraints of biological transmitters and receivers, respectively, is essential.

6.1.4 Detection of PAM Molecular Signals with Bacterial Receivers on a Microfluidic Channel

We have investigated the utilization of the bacterial signal transduction for the detection of pulse-amplitude modulated (PAM) molecular signals. The one-to-one input-output relation, the noise, and the timing issues on the bacteria response are examined based on both the measurements from the experiments and the analytical evaluations of a biochemical model of bacteria signal transduction. To sample the raw bacteria response, four different strategies,

i.e., the total response duration, the peak value, the ramp-up slope, and the ramp-down slope, are statistically compared. Based on the statistical comparisons, the sampling of the bacteria response via the ramp-up slope is selected for further investigation. The time-interval selection and non-coherent sampling for ramp-up slope calculation from the raw bacteria response are studied to address noise and timing issues, respectively. The provided analyses and results in this work provide a basis for efficient detection of the PAM molecular signals in molecular communication and sensing applications.

6.2 Future Research Directions

6.2.1 Modeling and Prediction for Intra/Inter Cellular Signaling

Noise in the biological pathways is due to the intracellular, intercellular, and extracellular stochastic biochemical elements, each having a different importance for the metabolism, gene regulation, and signal transduction of the cell. Synthetic biological systems similarly perform tasks by a population of cells to utilize intercellular communication for synchronization. Therefore, the prediction of the output signal given the input signal and the detection of the input signal from the output signal require a comprehensive modeling of intra/inter cellular signaling mechanisms.

By expanding the work presented in this thesis on engineered bacteria, the impact of noise from different sources at different time-scales including biofilm formation, mutation, and cell cycle on the processing of biochemical signals within biological circuits need to be investigated. Additionally, the interdependence of the diseases and the noise in the biological pathways should be investigated. The models to accurately predict the response or detect the excitation level of the engineered and natural intra/inter cellular signaling mechanisms are needed.

6.2.2 Computation with Interconnection of Biological Circuits

The synthetic biological systems can operate both as analog and digital devices. For example, biological circuits can perform as a switch as well as an amplifier based on their design. In the nature, input signals are usually in the analog form, and analog design can eliminate analog-to-digital/digital-to-analog conversion requirements for the circuit design and

can provide faster operation. However, digital processing is robust to noise at the expense of processing delay and complex circuit design due to the conversion between analog and digital signals. On the other hand, the required precision level depends on the time-scale and the nature of the computational process. The design trade-offs between the analog and digital computation within biological circuits for the precision, the delay, and the complexity of the process need to be investigated. Utilizing the developed methodologies for molecular communication over microfluidic channels and engineered bacteria, the theoretical limits for the intra/inter process communication need to be investigated addressing the unique communication challenges and requirements for the interconnection of biological circuits on a chip. Additionally, modulation, detection, medium access control, and addressing schemes should be developed for distributed molecular computation with networks of distinct populations of cells on a chip.

6.2.3 Continuous Monitoring of Intra-Body Biochemical Signals

To monitor the diseases and the disorders in the body, the concentration changes of biological markers can be sensed at different scales and converted to electronic signals by the bioelectronic interfaces implanted under the tissue. Furthermore, these interfaces can communicate with programmable cells to restore health and fight diseases. By merging my research on biological circuits and modeling of the intra/inter cellular signaling, the interfacing of the biological pathways with the cyber-human systems to dynamically track cellular physiology and function, and intervene to tune metabolism, gene regulation, and signal transduction is required. Furthermore, the interpretation of accumulated big data from continuously monitored people requires a new perspective for biomedical signal processing. For example, the daily fluctuations of hormone levels can be monitored for hundreds of thousands of individuals to determine a baseline for the extraction of the abnormalities and patterns. The methods are required to efficiently correlate the data and understand the changing intra-body biochemical signals at different time-scales in response to stress, medication, and infection.

REFERENCES

[1] A. O. Bicen, and I. F. Akyildiz, "System-theoretic Analysis and Least-squares Design of Microfluidic Channels for Flow-induced Molecular Communication," *IEEE Transactions on Signal Processing,* vol. 61, no. 20, pp. 5000-5013, October 2013.

[2] A. O. Bicen, and I. F. Akyildiz, "End-to-end Propagation Noise and Memory Analysis for Molecular Communication over Microfluidic Channels," *IEEE Transactions on Communications,* vol. 62, no. 7, pp. 2432-2443, July 2014.

[3] A. O. Bicen, and I. F. Akyildiz, "Interference Modeling and Capacity Analysis for Microfluidic Molecular Communication Channels," *IEEE Transactions on Nanotechnology,* vol. 14, no. 3, pp. 570-579, May 2015.

[4] A. O. Bicen, C. M. Austin, I. F. Akyildiz, and C. R. Forest, "Efficient Sampling of Bacterial Signal Transduction for Detection of Pulse-Amplitude Modulated Molecular Signals," *IEEE Transactions on Biomedical Circuits and Systems,* vol. 9, no. 4, pp. 505-517, August 2015.

[5] I. F. Akyildiz, J. M. Jornet, and M. Pierobon, "Nanonetworks: A New Frontier in Communications," *Communications of the ACM*, vol. 54, no. 11, pp. 84-89, Nov. 2011.

[6] I. F. Akyildiz, F. Brunetti, and C. Blazquez, "Nanonetworks: A New Communication Paradigm," *Computer Networks Journal (Elsevier)*, vol. 52, no. 12, pp. 2260-2279, Aug. 2008.

[7] M. Pierobon, and I. F. Akyildiz, "End-to-end Physical Model of Molecular Communications," *IEEE JSAC*, vol. 28, no. 4, pp 602-611, May 2010.

[8] J. Atencia, and D. J. Beebe, "Controlled microfluidic interfaces" *Nature*, vol. 437, no. 7059, pp. 648-655, Sept. 2005.

[9] I. F. Akyildiz, F. Fekri, R. Sivakumar, C. R. Forest, and B. K. Hammer, "MONACO: Fundamentals of Molecular Nano-communication Networks," *IEEE Wireless Commun.,* vol. 19, no. 5, pp. 12-18, Oct. 2012.

[10] M. Pierobon, and I. F. Akyildiz, "Diffusion-based noise analysis for molecular communication in nanonetworks," *IEEE Transactions on Signal Processing,* vol. 59, no. 6, pp. 2532-2547, June 2011.

[11] M. Pierobon, and I. F. Akyildiz, "Noise analysis in ligand-binding reception for molecular communication in nanonetworks," *IEEE Transactions on Signal Processing,* vol. 59, no. 9, pp. 4168-4182, Sept. 2011.

[12] M. Pierobon, and I. F. Akyildiz, "Capacity of a Diffusion-based Molecular Communication System with Channel Memory and Molecular Noise," *IEEE Transactions on Information Theory,* vol. 59, no. 2, pp. 942-954, Feb. 2013.

[13] T. Nakano, and J.-Q. Liu, "Design and Analysis of Molecular Relay Channels: An Information Theoretic Approach," *IEEE Transactions on Nanobiosience,* vol. 9, no. 3, pp. 213-221, September 2010.

[14] E. De Leo, L. Galluccio, A. Lombardo, and G. Morabito, "Networked Labs-on-a-Chip (NLoC): Introducing Networking Technologies in Microfluidic Systems," *Nano Communication Networks (Elsevier),* vol. 3, no. 4, pp. 217-228, Dec. 2012.

[15] H. Bruus, Theoretical Microfluidics, Oxford University Press, 2008.

[16] B. Kirby, Micro- and Nanoscale Fluid Mechanics: Transport in Microfluidic Devices, Cambridge University Press, New York, 2010.

[17] J. M. Koo, and C. Kleinstreuer, "Liquid Flow in Microchannels: Experimental Observations and Computational Analyses of Microfluidics Effects," *J. Micromech. Microeng.,* vol. 13, no. 5, pp. 568-579, May 2003.

[18] D. Di Carlo, "Inertial Microfluidics," *Lab Chip,* vol. 9, no. 21, pp. 3038-3046, Nov. 2009.

[19] D. Huh, J. H. Bahng, Y. B. Ling, H. H. Wei, O. D. Kripfgans, J. B. Fowlkes, J. B. Grotberg, and S. Takayama, "Gravity-driven Microfluidic Particle Sorting Device with Hydrodynamic Separation Amplification," *Anal. Chem.,* vol. 79, no. 4, pp. 1369-1376, Feb. 2007.

[20] D. Di Carlo, D. Irimia, R. G. Tompkins, and M. Toner, "Continuous Inertial Focusing, Ordering, and Separation of Particles in Microchannels," *Proc. Natl. Acad. Sci. U.S.A.,* vol. 104, no. 48, pp. 18892-18897, Nov. 2007.

[21] M. J. Fuerstman, P. Deschatelets, R. Kane, A. Schwartz, P. J. A. Kenis, J. M. Deutch, and G. M. Whitesides, "Solving Mazes using microfluidic networks," *Langmuir,* vol. 19, no. 11, pp. 4714-4722, Apr. 2003.

[22] S. Gendels, and A. Jakovics, "Numerical Modeling of Hydraulic Resistance in Pipes of Various Shapes," *Latvian Journal of Physics and Technical Sciences,* vol. 41, no.4, pp. 13-27, 2004.

[23] A. Brask, G. Goranovic, and H. Bruus, "Theoretical Analysis of the Low-voltage Cascade Electro-osmotic Pump," *Sensors and Actuators B: Chemical,* vol. 92, no. 1-2, pp. 127-132, July 2003.

[24] D. Dutta, A. Ramachandran, and D. T. Leighton Jr, "Effect of Channel Geometry on Solute Dispersion in Pressure-driven Microfluidic Systems," *Microfluid Nanofluid,* vol. 2, no. 2, pp. 275-290, July 2006.

[25] H. A. Stone, A. D. Stroock, and A. Ajdari, "Engineering Flows in Small Devices: Microfluidics Toward a Lab-on-a-Chip," *Annual Review of Fluid Mechanics,* vol. 36, pp. 381-411, Jan. 2004.

[26] J. I. Molho, A. E. Herr, B. P. Mosier, J. G. Santiago, and T. W. Kenny, "Optimization of Turn Geometries for Microchip Electrophoresis" *Analytical Chemistry,* vol. 73, no. 6, pp. 1350-1360, Mar. 2001.

[27] T. Danino, O. Mondragon-Palomino, L. Tsimring, and J. Hasty, "A Synchronized Quorum of Genetic Clocks," *Nature,* vol. 463, no. 7279, pp. 326-330, Jan. 2010.

[28] T. M. Squires, and S. R. Quake, "Microfluidics: Fluid Physics at the Nanoliter Scale," *Rev. Mod. Phys.,* vol. 77, no. 3, pp. 977–1026, Oct. 2005.

[29] K. W. Oh, K. Lee, B. Ahn, and E. P. Furlani, "Design of Pressure-driven Microfluidic Networks using Electric Circuit Analogy," *Lab Chip,* vol. 12, no. 3, pp 515–545, 2012.

[30] Y. Zhou, Y. Wang, T. Mukherjee, and Q. Lin "Generation of Complex Concentration Profiles by Partial Diffusive Mixing in Multi-stream Laminar Flow," *Lab Chip,* vol. 9, no. 10, pp. 1439–1448, 2009.

[31] S. K. Griffiths, and R. H. Nilson, "Design and Analysis of Folded Channels for Chip-Based Separations" *Anal. Chem.* vol. 74, no. 13, pp. 2960–2967, July 2002.

[32] S. K. Griffiths, and R. H. Nilson, "Low-Dispersion Turns and Junctions for Microchannel Systems" *Anal. Chem.* vol. 73, no. 2, pp. 272–278, January 2001.

[33] Y. Wang, T. Mukherjee, and Q. Lin, "Systematic Modeling of Microfluidic Concentration Gradient Generators" *Journal of Micromechanics and Microengineering* vol. 8, no. 5, pp. 2128–2137, September 2006.

[34] A. S. Bedekar, Y. Wang, S. Krishnamoorthy, S. S. Siddhaye, and S. Sundaram, "System-Level Simulation of Flow-Induced Dispersion in Lab-on-a-Chip Systems," *IEEE Transactions on Computer-aided Design of Integrated Circuits and Systems,* vol. 25, no. 2, pp. 294–304, Feb. 2006.

[35] S. Kim, H. J. Kimzb, and N. L. Jeon "Biological applications of microfluidic gradient devices," *Integrative Biology,* vol. 2, no. 11-12, pp. 584–60, 2010.

[36] Y. Xie, Y. Wang, L. Chen, and C. H. Mastrangelo, "Fourier Microfluidics," *Lab Chip,* vol. 8, no. 5, pp. 779–785, 2008.

[37] B. Atakan, and O. B. Akan, "On Channel Capacity and Error Compensation in Molecular Communication," *Trans. Comput. Syst. Biol. X,* pp. 59-80, 2008.

[38] D. J. Spencer, S. K. Hampton, P. Park, J. P. Zurkus, and P. J. Thomas, "The Diffusion-limited Biochemical Signal-relay Channel," in *Proc. Adv. Neural Inf. Process. Syst.,* vol. 16, 2004.

[39] M. J. Moore, T. Suda, and K. Oiwa, "Molecular Communication: Modeling Noise Effects on Information rate," *IEEE Trans. Nanobiosci.,* vol. 8, no. 2, pp. 169–180, Jun. 2009.

[40] D. Mark, S. Haeberle, G. Roth, F. von Stetten, and R. Zengerle, "Microfluidic Lab-on-a-Chip Platforms: Requirements, Characteristics and Applications," *Chem. Soc. Rev.,* vol. 39, pp. 1153-1182, 2010.

[41] B. Atakan, and O. B. Akan, "Deterministic capacity of information flow in molecular nanonetworks," *Nano Communication Networks,* vol. 1, no. 1, pp. 31–42, March 2010.

[42] C. E. Shannon, *A mathematical theory of communication.* Urbana, USA: Univ. Illinois Press, 1949.

[43] B. D. Unluturk, A. O. Bicen, and I . F. Akyildiz, "Genetically Engineered Bacteria-based BioTransceivers for Molecular Communication," *IEEE Transactions on Communications,* vol. 63, no. 4, pp. 1271-1281, April 2015.

[44] U. Alon, *An introduction to systems biology: design principles of biological circuits,* CRC press, 2006.

[45] B. Novak, and J. J. Tyson, "Design Principles of Biochemical Oscillators" *Nat. Rev. Mol. Cell Biol.,* vol. 9, no. 12, pp. 981–991, December 2008.

[46] J. Hasty, D. McMillen, and J. J. Collins, "Engineered gene circuits," *Nature,* vol. 420, no. 14, pp. 224–230, 2002.

[47] W. Bialek, and S. Setayeshgar, "Physical Limits to Biochemical Signaling," vol. 102, no. 29, pp. 10040-10045, July 2005.

[48] S. S. Andrews, and A. P. Arkin, "Simulating Cell Biology," *Current Biology,* vol. 16, no. 14, pp. R523-R527, 2006.

[49] O. Suvak, and A. Demir, "Phase Computations and Phase Models for Discrete Molecular Oscillators," *EURASIP Journal on Bioinformatics and Systems Biology,* 2012.

[50] D. T. Gillespie, "Stochastic Simulation of Chemical Kinetics," *Annu. Rev. Phys. Chem.,* vol. 58, pp. 35-55, 2007.

[51] D. Dutta, and D. T. Leighton, "Dispersion Reduction in Pressure-Driven Flow Through Microetched Channels," *Anal. Chem.,* vol. 73, no. 3, pp. 504-513, Feb. 2001.

[52] G. M. Whitesides, "The origins and the future of microfluidics" *Nature*, vol. 442, no. 7101, pp. 368–373, July 2006.

[53] T. Vilkner, D. Janasek, and A. Manz, "Micro Total Analysis Systems. Latest Advancements and Trends," *Analytical Chemistry,* vol. 78, no. 12, pp. 3887-3907, June 15, 2006.

[54] D. Janasek, J. Franzke, and A. Manz, "Scaling and the Design of Miniaturized Chemical-Analysis Systems," *Nature,* no. 442, pp. 374–380, 27 July 2006.

[55] T. Thorsen, S. J. Maerkl, and S. R. Quake, "Microfluidic Large-Scale Integration," *Science,* vol. 298, no. 5593, pp. 580-584, 18 October 2002.

[56] J. Melin, and S. R. Quake, "Microfluidic Large-Scale Integration: The Evolution of Design Rules for Biological Automation," *Annual Review of Biophysics and Biomolecular Structure,* vol. 36, pp. 213-231, June 2007.

[57] P. J. Lee, P. J. Hung, V. M. Rao, L. P. Lee "Nanoliter Scale Microbioreactor Array for Quantitative Cell Biology," *Biotechnology and Bioengineering,* vol. 94, No. 1, May 5, 2006.

[58] B. M. Willardson, J. F. Wilkins, T. A. Rand, J. M. Schupp, K. K. Hill, P. K. and P. J. Jackson, "Development and Testing of a Bacterial Biosensor for Toluene-Based Environmental Contaminants," *Appl. Environ. Microbiol.,* vol. 64, no. 3, pp. 1006-1012, March 1998.

[59] S. Leth, S. Maltoni, R. Simkus, B. Mattiasson, P. Corbisier, I. Klimant, O. S. Wolfbeis, and E. Csoregi, "Engineered Bacteria Based Biosensors for Monitoring Bioavailable Heavy Metals," *Electroanalysis,* vol. 14, no. 1, pp. 35-42, January 2002.

[60] T. Elad, J. H. Lee, M. B. Gu, and S. Belkin "Microbial Cell Arrays," *Adv Biochem Engin/Biotechnol,* vol. 117, pp. 85–108, 2010.

[61] S. Daunert, G. Barrett, J. S. Feliciano, R. S. Shetty, S. Shrestha, and W. Smith-Spencer, "Genetically Engineered Whole-Cell Sensing Systems: Coupling Biological Recognition with Reporter Genes," *Chem. Rev.* vol. 100, no. 7, pp. 2705–2738, July 2000.

[62] S. Belkin, "Microbial whole-cell sensing systems of environmental pollutants," *Current Opinion in Microbiology,* vol. 6, no. 3, pp. 206-212, June 2003.

[63] S. Magrisso, Y. Erel, and S. Belkin, "Microbial reporters of metal bioavailability," *Microbial Biotechnology,* vol. 1, no. 4, pp. 320-330, 2008.

[64] S. J. Sorensen, M. Burmolle, and L. H. Hansen, "Making bio-sense of toxicity: new developments in whole-cell biosensors" *Current Opinion in Biotechnology,* vol. 17, vol. 1, pp. 11-16, February 2006.

[65] M.T. Barros, S. Balasubramaniam, B. Jennings, Y. Koucheryavy, "Transmission Protocols for Calcium-Signaling-Based Molecular Communications in Deformable Cellular Tissue," *IEEE Transactions on Nanotechnology,* vol.13, no.4, pp. 779–788, July 2014.

[66] D. Kilinc and O. B. Akan, "An information Theoretical Analysis of Nanoscale Molecular Gap Junction Communication Channel between Cardiomyocytes," *IEEE Transactions on Nanotechnology,* vol. 12, no. 2, pp. 129–136, Mar. 2013.

[67] M. Pierobon, and I. F. Akyildiz, "A Statistical-Physical Model of Interference in Diffusion-Based Molecular Nanonetworks," *IEEE Transactions on Communications,* vol. 62, no. 6, pp. 2085-2095, June 2014.

[68] T. M. Cover, and J. A. Thomas, *Elements of Information Theory.* New York, NY, USA: Wiley-Interscience, 2006.

[69] S. Park, X. Hong, W. S. Choi, and T. Kim, "Microfabricated ratchet structure integrated concentrator arrays for synthetic bacterial cell-to-cell communication assays," *Lab Chip,* vol. 12, no. 20, pp. 3914-3922, September 2012.

[70] A. Prindle, J. Selimkhanov, H. Li, I. Razinkov, L. S. Tsimring, and J. Hasty, "Rapid and tunable post-translational coupling of genetic circuits," *Nature,* vol. 508, no. 7496, pp. 387–391, April 2014.

[71] B. Krishnaswamy, C. M. Austin, J.P. Bardill, D. Russakow, G. L. Holst, B. K. Hammer, C. R. Forest, and R. Sivakumar, "Time-elapse communication: bacterial communication on a microfluidic chip," *IEEE Transactions on Communications,* vol. 61, no. 12, pp. 5139-5151, December 2013.

[72] J. R. van der Meer, and S. Belkin, "Where microbiology meets microengineering: design and applications of reporter bacteria," *Nature Reviews Microbiology,* vol. 8, no. 7, pp. 511-522, 2010.

[73] C. M. Austin, W. Stoy, P. Su, M. C. Harber, J. P. Bardill, B. K. Hammer, C. R. Forest, "Modeling and validation of autoinducer-mediated bacterial gene expression in microfluidic environments," *Biomicrofluidics,* 2014.

[74] D. Kilinc, O. B. Akan, "Receiver Design for Molecular Communication," *IEEE Journal on Selected Areas in Communications,* vol.31, no.12, pp.705-714, December 2013.

[75] L.-S. Meng, P.-C. Yeh, K.-C. Chen, I. F., Akyildiz, "On Receiver Design for Diffusion-Based Molecular Communication," *IEEE Transactions on Signal Processing,* vol. 62., no. 22, pp. 6032-6044, Nov. 15 2014.

[76] H. H. McAdams, and A. Arkin, "Stochastic Mechanisms in Gene Expression," *Proc. National Academy of Sciences,* vol. 94, pp. 814-819, February 1997.

[77] M. Kaern, T. C. Elston, W. J. Blake, and J. J. Collins, "Stochasticity in Gene Expression: From Theories to Phenotypes," *Nature Reviews,* vol. 6, pp. 451-464, June 2005.

[78] J. M. Raser, and E. K. O'Shea "Noise in Gene Expression: Origins, Consequences, and Control," *Science Mag,* 2005.

[79] M. B. Elowitz, A. J. Levine, E. D. Siggia, and P. S. Swain, "Stochastic Gene Expression in a Single Cell," *Science Mag,* 2002.

[80] R. Sharpeskhar, Ultralow Power Bioelectronics: *Fundamentals, Biomedical Applications and Bio-Inspired Systems.* Cambridge, U.K.: Cambridge Univ. Press, 2010.

[81] C. J. Myers, *Engineering Genetic Circuits,* CHAPMAN & HALL/CRC press, 2010.

[82] G. Bernot, J.-P. Comet, A. Richard, M. Chaves, J.-L. Gouze, and F. Dayan, "Modeling and Analysis of Gene Regulatory Networks," in *Modeling in Computational Biology and Biomedicine,* Edited by F. Cazals, and P. Kornprobst, Springer, pp. 47-80, 2013.

[83] B.-S. Chen, W.-S. Wu, Y.-C. Wang, and W.-H. Li, "On the Robust Circuit Design Schemes of Biochemical Networks: Steady-State Approach," *IEEE Transactions on Biomedical Circuits and Systems,* vol. 1, no. 2, pp. 114-132, June 2007.

[84] B.-S. Chen, and P.-W. Chen, "Robust Engineered Circuit Design Principles for Stochastic Biochemical Networks With Parameter Uncertainties and Disturbances," *IEEE Transactions on Biomedical Circuits and Systems,* vol. 2, no. 2, pp. 114-132, June 2008.

[85] F.-X. Wu, "Global and Robust Stability Analysis of Genetic Regulatory Networks With Time-Varying Delays and Parameter Uncertainties," *IEEE Transactions on Biomedical Circuits and Systems,* vol. 5, no. 4, pp. 391-398, August 2011.

[86] A. Bar-Even, J. Paulsson, N. Maheshri, M. Carmi, E. O'Shea, Y. Pilpel, and N. Barkai, "Noise in protein expression scales with natural protein abundance," *Nature Genetics,* vol. 38, no. 6, pp. 636-643, June 2006.

[87] J. H. McDonald, *Handbook of Biological Statistics,* 3rd ed. Baltimore, Maryland: Sparky House Publishing, 2014.

[88] H. L. Van Trees, *Detection, Estimation, and Modulation Theory, Part I.* New York: John Wiley & Sons, 1968.

VITA

Ahmet Ozan Biçen was born on December 16, 1987, in Istanbul, Turkey. He received the B.Sc. and M.Sc. degrees in Electrical and Electronics Engineering from Middle East Technical University, Ankara, Turkey, in 2010 and from Koc University, Istanbul, Turkey in 2012, respectively. He attended the doctoral program at the School of Electrical and Computer Engineering of Georgia Institute of Technology, Atlanta, GA, from August 2012 to May 2016, where he was a research assistant in the Broadband and Wireless Networking Laboratory (BWN-LAB). He is also the recipient of the Researcher of Year 2014 Award of BWN-LAB. In May 2016, he received his Ph.D. in Electrical and Computer Engineering from Georgia Institute of Technology.